eXPRESS Polymer Letters Vol.8, No.5 (2014) 300
Available online at www.expresspolymlett.com
DOI: 10.3144/expresspolymlett.2014.33

Editorial corner – a personal view
Electric conductance of carbon/epoxy laminated composites

*A. Todoroki**

Tokyo Institute of Technology, 2-12-1, Ookayama, Meguro, Tokyo, Japan

For continuous carbon fiber composites, the electric conductance in the fiber direction can be easily calculated using the rule of mixture. The measured result is not so different from the calculated one and the scatter of the measured results is small.

The electric conductance in the transverse direction and that in the thickness direction, however, are not easily obtained by calculations. The values of electric conductance of these directions depend on the contacts between the carbon fibers, for example, when the bundle is twisted, there may be higher electrical conductance in the transverse direction and lower conductance in the thickness direction compared with that of the transverse direction. The reason is that the twisting of the fiber boundle makes a lot of chance of the adjacent fiber contact and the twisting makes small movement of fibers in the thickness direction when the composite structure is cured. This small movement of the fibers causes less fiber contacts between plies.

Unfortunately, the electrical properties are not usually qualified as a specification even for the commercially available composites. This may cause large scatter of the measured results of conductance usually observed in the transverse and in the thickness direction.

Recently several new composites introduce polymer rich layer or dots between the plies to increase delamination strength. This may cause significant decrease of electric conductance in the thickness direction. This may cause another problem. For example, electrical ground is usually taken to the body in automobiles, but when there is significant decrease of electric conductance in the thickness direction, the electric potential difference may exist between the plies in components. This could cause the induced electric current when the large electric current flows near the automobile surface. Even when the airplane has lightning strike protection system such as copper mesh or copper foil strips, the extremely steep and large electric current of the lightning may cause large electric current in the protection system and the induced electric current flows in the composites.

Unfortunately, there is no qualification specification of the electric conductance in the composites. It is unknown how large is the scatter of the electric conductance in the thickness direction of the components made of carbon fibers. The values depend on fabrication process. Factors affecting the electric conductance in the thickness direction are also unclear.

I believe we should be careful with respect to the electrical conductance of carbon composites. That is not a constant material property especially in the thickness direction. Of course, as discussed in the first part, the conductance in the fiber direction is well controlled. The electric conductance of the laminated composites is completely different from that of metallic materials, and I hope we should do more research of composites on the electric conductance.

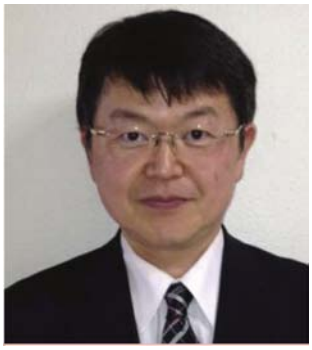

Prof. Dr. Akira Todoroki
Member of International Advisory Board

*Corresponding author, e-mail: atodorok@ginza.mes.titech.ac.jp

eXPRESS Polymer Letters Vol.8, No.5 (2014) 301–311
Available online at www.expresspolymlett.com
DOI: 10.3144/expresspolymlett.2014.34

Plastic flow and failure in single point incremental forming of PVC sheets

S. Alkas Yonan[1], *M. B. Silva*[2], *P. A. F. Martins*[2*], *A. E. Tekkaya*[1]

[1]Institute of Forming Technology and Lightweight Construction, Technical University of Dortmund, Baroper Str. 301, D-44227 Dortmund, Germany
[2]Instituto Superior Técnico, Universidade de Lisboa, Av. Rovisco Pais, 1049-001 Lisboa, Portugal

Received 20 October 2013; accepted in revised form 16 December 2013

Abstract. This paper presents an innovative and effective methodology to characterize plastic flow and failure in single point incremental forming (SPIF) of polymers that allows determining the stresses and the accumulated values of ductile damage directly from the experimental values of strain at various positions over the deformed polymer sheets. The approach traces the deformation path of material elements in conical and pyramidal SPIF parts, undergoing linear strain loading paths from beginning until failure, and is built upon the generalization of the analytical framework conditions assumed by Glover *et al*. [1] to the pressure-sensitive yield surfaces of polymers under incompressible, non-associated, plastic flow. Experimentation in conventional and multi-stage SPIF of Polyvinylchloride (PVC) sheets confirms the effectiveness of the proposed methodology and demonstrates that standard non-coupled damage models currently utilized in sheet metal forming are inapplicable to describe failure in polymers. Instead fracture forming limit lines (FFL's) should be employed.

Keywords: *processing technologies, incremental sheet forming, polyvinylchloride (PVC), damage, fracture*

1. Introduction

Current manufacturing technologies for producing polymer parts are based on heating-shaping-cooling process routes and are closely linked to mass production. The first attempt to develop a flexible, cost-efficient technology to allow small batch production of polymer parts was performed by Franzen *et al*. [2], who evaluated the performance of single point incremental forming (SPIF) to shape commercial Polyvinylchloride (PVC) sheets at room temperature (Figure 1a). Table 1 presents a comparative summary of the main technical and economic aspects of different polymer processing technologies.

Franzen *et al*. [2] identified the main operating parameters of the process and systematized three different modes of failure, giving special emphasis to the development of cracks in conditions that are different from those commonly found in the SPIF of metals.

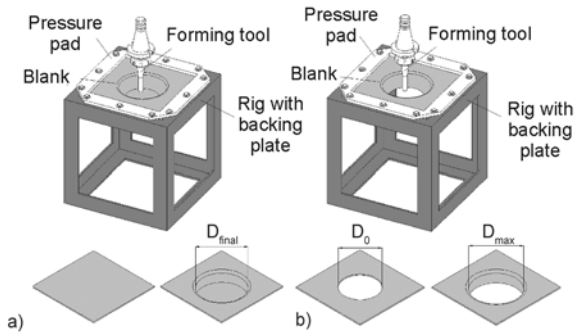

Figure 1. Schematic representation of the experimental apparatus utilized in single point incremental forming (SPIF) for producing (a) a conical part and (b) a hole-flanged cylindrical part in a blank with a pre-cut hole

*Corresponding author, e-mail: pmartins@ist.utl.pt

Table 1. Technic and economic aspects of polymer processing

	Equipment cost	Tooling cost	Production rate	Batch size (number of parts)	Applications
Blow moulding	Medium	Medium	Medium	$>10^3$	Hollow thin-walled parts such as bottles, containers and fuel tanks
Compression moulding	High	Medium	Medium	$>10^3$	Parts similar to closed-die forgings primarily made from highly filled polymers with a high viscosity
Injection moulding	High	High	High	$>10^4$	Complex shapes of various sizes with fine details such as gears, fasteners, housings, switches and knobs
Transfer moulding	High	High	Medium	$>10^3$	More complex parts than those produced by compression moulding
Thermoforming	Low	Low	Low	$>10^2$	Parts with shallow or deep cavities made from polymer sheets such as packaging cases
SPIF	(*)	Very Low	Low	>1	Rapid prototypes and low batch production of simple polymer sheet parts similar to those fabricated by thermoforming

(*) Does not require a specific piece of equipment because CNC machining centers are commonly available at industrial companies.

In a subsequent publication, Le *et al*. [3] presented a set of experimental results in SPIF of Polypropylene (PP) sheets and utilized statistical analysis based on design of experiments to study the influence of the step size, tool size, feed rate and spindle speed on the overall formability of the process. Two modes of failure similar to those that had been previously observed by Franzen *et al*. [2] were reported. In a second paper, Martins *et al*. [4] extended the scope of their investigation to include four additional polymers (polyoxymethylene (POM), polyethylene (PE), polyamide (PA) and polycarbonate (PC)). The previously identified failure modes were revisited in the light of new experimental data and a criterion for the selection of polymers for SPIF applications was proposed.

Taken together at the end of 2009, the results of the abovementioned preliminary studies allowed anticipating that research in the SPIF of polymers would continue to be carried out in two different approaches. Firstly, to evaluate the performance and potential applications of different polymers under new and increasingly sophisticated sets of operating parameters. Secondly, to develop a new fundamental level of understanding about the SPIF of polymers by means of analytical or numerical models that could be able to predict plastic flow and failure across the useful range of operating conditions.

The work of Silva *et al*. [5] in hole-flanging of polyethylene terephthalate (PET) and (PC) sheets by means of multistage SPIF is a good example of the first line approach and contributed to enlarging the scope of applications of the SPIF of polymers to the production of hole-flanged parts with vertical walls (Figure 1b). The discussion on the relative performance of the SPIF of polymers against that of metals performed by Silva *et al*. [6] may also be included in the first line approach (Table 2).

The works of Silva *et al*. [7] and Alkas Yonan and coworkers [8, 9] were built upon the second line approach. Silva *et al*. [7] developed a theoretical framework based on membrane analysis and pressure-sensitive yield surfaces to characterize plastic flow and failure in polymer sheets. Alkas Yonan and coworkers [8, 9] developed a non-linear viscoplastic material model for thermoplastics and its finite strain extension to the finite element simulation of PVC parts produced by SPIF.

However, both developments exhibited difficulties in modelling the SPIF of polymers. For example, the theoretical framework proposed by Silva *et al*. [7] could only be qualitatively assessed against experimental data and observations. On the other hand,

Table 2. Experimental maximum drawing angles ψ_{max} that metal and polymer sheet blanks can undertake when producing a truncated conical shape by SPIF

Material		ψ_{max} [°]
Aluminium	AA1050-O	80º
	AA1050-H111	76º
	AA5052	74º
Steel	DC01	76º
	DC04	74º
	AISI 304L	74º
Titanium	Grade 2	65º
Polymer	PET	~90º
	PVC	66º

the evaluation of the non-linear viscoplastic material model proposed by Alkas Yonan and coworkers [8, 9] was limited by small deformations, which prevented analysing plastic flow and the corresponding stress field for high values of strain.

As a result of the abovementioned limitations, the aims and scope of this paper is to present an alternative and effective methodology to characterize plastic flow and failure in the SPIF of polymers. The proposed methodology traces the deformation path of material elements in conical and pyramidal benchmark parts produced by SPIF and is built upon the generalization of the analytical framework proposed by Glover *et al*. [1], in their investigation on failure maps in sheet metal forming, to pressure-sensitive yield surfaces under non-associated plastic flow.

In general, the proposed methodology to be presented in this paper will provide quantitative answers to important key questions related to the SPIF of polymers that were never solved or properly addressed before; what is the stress distribution and how can these values be determined from the experimental values of strain at various positions over the polymer SPIF parts? How can the critical values of ductile damage based on standard non-coupled models be experimentally determined without having the need to apply inverse calibration procedures? Is there a correlation between the aforementioned values of ductile damage at the onset of necking and the fracture forming line (FFL)? Can the FFL be successfully utilized for assessing the formability limits of multi-stage SPIF of polymer sheets?

The organization of the paper is the following. Section 2. summarises the experimental procedures utilized in the mechanical and formability characterization of the material, presents the fundamentals of the new proposed methodology to determine the distributions of stress and ductile damage at the onset of cracking, and describes the work plan utilized in the experiments that give support to the paper. Section 3. presents and discusses the results obtained in SPIF of cones and pyramids, analysing the strain loading paths in the principal strain space in the light of non-coupled ductile damage criteria and the FFL. The effectiveness of the FFL is subsequently evaluated by means of experiments in hole-flanging produced by multi-stage SPIF. Section 4. presents the conclusions.

2. Experimental

2.1. Determination of the stress-strain curve

The research work was performed on sheets of polyvinylchloride (PVC) with 3 mm thickness (commercial designation Koemadur WA 155, supplier Koemmerling, Germany). The choice of PVC results from its high strength, good dimensional stability and more environmental friendly features than alternative polymers due to its lower dependency on petroleum (only 40% of the composition of PVC is petroleum-derived).

The stress-strain curves of PVC were obtained by means of tensile and stack compression tests. The specimens utilized in the tensile tests were machined from the supplied sheets in accordance to the ISO 527 standard. The testing speed was equal to 0.2 mm/min. The multi-layer cylinder specimens utilized in the stack compression tests were assembled by piling up 3 circular discs with 12 mm diameter and 3 mm thickness cut from the aforementioned PVC sheets by water jet. The testing speed was equal to 0.02 mm/min.

Figure 2 shows the tensile and compressive stress-strain curves of PVC. It is worth noting that the engineering stress-strain curves resulting from the tensile and stack compression tests were converted into true stress-strain curves in order to be employed in the analytical methodology to characterize plastic flow and failure that will be described in section 2.2. The relationship between true stress and true strains for both tensile and stack compression tests were approximated by a Ludwik-Hollomon's model $\sigma = K\varepsilon^n$ (Figure 2) assuming PVC as incom-

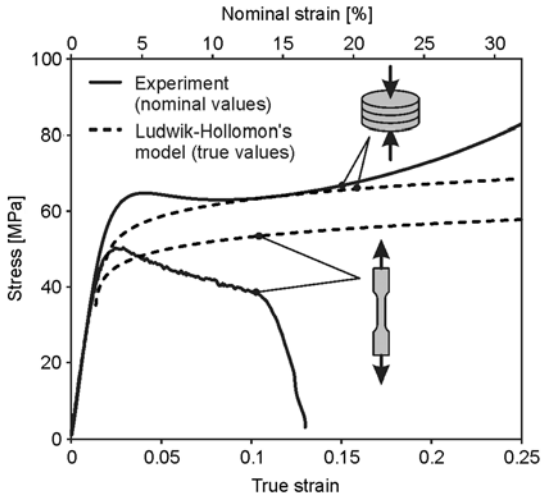

Figure 2. Stress-strain curves of PVC obtained from tensile and stack compression tests

Table 3. Representative summary of the mechanical properties of the PVC sheets that were utilized in the investigation

	Elasticity modulus (tension), E [MPa]	Elasticity modulus (compression), E [MPa]	Yield stress (tension), σ_{YT} [MPa]	Yield stress (compression), σ_{YC} [MPa]
Average value	2760.0	2712.27	38.63	46.67
Standard deviation	58.3	10.90	1.05	3.06

pressible (see Equation (1)). This was necessary in order to facilitate mathematical treatment by means of the proposed methodology to be described in section 2.2.:

Tensile test: $\sigma = 65\varepsilon^{0.082}$ [MPa]
Stack compression test: $\sigma = 77\varepsilon^{0.08}$ [MPa] (1)

The difference between the tensile and compressive stress-strain curves is attributed to the strength differential effect that is caused by the pressure-sensitive characteristics of the yield surface. Table 3 presents a summary of the mechanical properties of PVC.

2.2. Determination of strains, stresses and ductile damage

The experimental technique utilized for determining the in-plane strains on the surface of the specimens produced by SPIF made use of imprinted grids of dots with 2 mm initial spacing between dot centres (Figure 3). During SPIF, the grid deforms with the material, and the corresponding major and minor surface strains were automatically measured from the deformed pattern by employing a digital image correlation technique based on a commercial Argus system of GOM mbH that compares the actual grid with the original (undeformed) grid.

In general, sheet metal forming is characterized by complex strain paths that prevent the distribution of stresses and the critical values of damage at the onset of necking to be directly determined from the experimental values of strain. However, in case of conical and pyramidal SPIF parts made from PVC, previous work in the field combined with results obtained in the present investigation showed that strain paths are linear and do not experience abrupt changes in direction at the forming limit curve (FLC) [7].

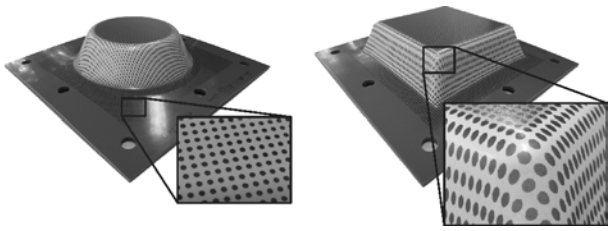

Figure 3. Conical and pyramidal parts produced by SPIF with a constant drawing angle $\psi = 60°$ showing details of the undeformed and deformed grid of dots that were imprinted on the surface of the blanks before testing

The aforementioned observation opens the possibility of utilizing SPIF tests based on conical and pyramidal geometries to set up a new methodology for determining the stress distribution and the critical values of damage from the experimental strains at the onset of cracking. In specific terms the proposed approach makes use of the pressure modified version of the von Mises yield criterion (see Equation (2)) that explicitly accounts for the stress differential effect of polymers [10]:

$$F(\sigma_{ij}) = \bar{\sigma}^2 - \sigma_C \cdot \sigma_T + (\sigma_C - \sigma_T)\sigma_{kk} = 0 \quad (2)$$

where $F(\sigma_{ij})$ is the yield function, $\bar{\sigma} = \sqrt{\frac{1}{2}\sigma'_{ij}\sigma'_{ij}}$ is the effective stress, σ'_{ij} is the deviatoric stress and $\sigma_{kk} = \delta_{ij}\sigma_{ij}$. The tensile σ_T and compressive σ_C flow stresses are obtained from tension and compression tests (Section 2.1.) and in case $\sigma_{T=}\sigma_C$, the traditional von Mises criterion (currently utilized in metals) results.

Because PVC is nearly incompressible [11], the normality rule typical of associated plasticity does not hold in case of pressure dependent yield surfaces (Equation (2)) since it leads to volume variations that are at least one order of magnitude larger than observed experimental values [12]. Instead, a non-associated flow rule where the plastic potential is taken as J_2 of the von-Mises plasticity should be employed [11, 13].

Under these circumstances, and assuming isotropic plastic deformation under plane stress conditions $\sigma_3 = 0$, the constitutive equations relating the in-plane strain increments with the applied stresses are given by Equation (3):

$$d\varepsilon_1 = \frac{d\bar{\varepsilon}}{\bar{\sigma}}\left(\sigma_1 - \frac{1}{2}\sigma_2\right), \; d\varepsilon_2 = \frac{d\bar{\varepsilon}}{\bar{\sigma}}\left(\sigma_2 - \frac{1}{2}\sigma_1\right) \quad (3)$$

where the effective stress $\bar{\sigma}$ and the effective strain increment $d\bar{\varepsilon}$ are obtained from Equation (4):

$$\bar{\sigma} = \sqrt{\sigma_1^2 + \sigma_2^2 - \sigma_1\sigma_2},$$
$$d\bar{\varepsilon} = \frac{2}{\sqrt{3}}\sqrt{d\varepsilon_1^2 + d\varepsilon_2^2 + d\varepsilon_1 d\varepsilon_2} \quad (4)$$

Now, taking into consideration that plastic deformation of PVC sheets in conical and pyramidal SPIF parts is carried out under linear strain-paths with a slope $\beta = d\varepsilon_2/d\varepsilon_1 = \varepsilon_2/\varepsilon_1$, the following relationship can be derived as shown by Equation (5):

$$\alpha = \frac{\sigma_2}{\sigma_1} = \frac{2\beta + 1}{2 + \beta} \quad (5)$$

and the simplified expressions of the principal in-plane stresses (σ_1, σ_2) can be obtained by replacing Equation (5) into Equation (4):

$$\sigma_1 = \frac{\bar{\sigma}}{\sqrt{(1 - \alpha + \alpha^2)}}, \sigma_2 = \frac{\alpha\bar{\sigma}}{\sqrt{(1 - \alpha + \alpha^2)}} \quad (6)$$

The effective stress $\bar{\sigma}$ in Equation (6) is calculated by combining the tensile and compressive flow stresses from Equation (1) into Equation (2) with the integration of the increment of effective strain $\bar{\varepsilon} = \int d\bar{\varepsilon}$ up to the actual plastic deformation.

Once the distribution of stress is determined from the experimental measurements of the major in-plane strains, the critical values of damage D^{crit} at the onset of failure are easily obtained by integrating the damage function D from beginning until failure (that is, until the amount of deformation that corresponds to the instant of time where cracking occurs).

The present work makes use of the normalized Cockcroft-Latham [14] ductile fracture criterion and of two other ductile fracture criteria that are based on the triaxiality ratio $\sigma_m/\bar{\sigma}$ that was originally proposed by McClintock [15] and is known to play an important role in the overall formability. The damage functions D_{CL}, D_{RT} and D_A of the ductile fracture models proposed by Cockcroft and Latham [14], Rice and Tracey [16] and Ayada *et al*. [17], take the form given by Equation (7):

$$D_{CL} = \int_0^{\bar{\varepsilon}_f} \frac{\sigma_1}{\bar{\sigma}} d\bar{\varepsilon}, \; D_{RT} = \int_0^{\bar{\varepsilon}_f} \exp\left(\frac{3}{2}\frac{\sigma_m}{\bar{\sigma}}\right) d\bar{\varepsilon}$$
$$D_A = \int_0^{\bar{\varepsilon}_f} \frac{\sigma_m}{\bar{\sigma}} d\bar{\varepsilon} \quad (7)$$

where $\sigma_m = \sigma_{kk}/3$ is the average stress and $\bar{\varepsilon}_f$ is the effective strain at fracture.

The overall methodology could have been extended to other ductile fracture criteria available in the literature but its application would basically remain identical.

2.3. Determination of the fracture forming limit line

The formability limits at fracture (fracture forming limit line, FFL) were determined by combining the results obtained from independent tensile and hydraulic bulge tests with the experimental measurements performed on conical and pyramidal SPIF parts at the onset of cracking.

The tensile tests were performed in an Instron 4507 testing machine and the hydraulic bulge tests were performed in a universal sheet testing machine (Erichsen 145/60) using a bi-axial circular (100 mm) tooling set. The conical and pyramidal SPIF parts were produced with a forming tool with a hemispherical tip of 10 mm diameter. The tests were performed with helical tool paths characterized by a step size per revolution equal to 0.5 mm (downward feed) and a feed rate equal to 1000 mm/min. The rotation of the forming tool was free and the lubricant was deep-drawing oil.

The experimental strains at the onset of fracture resulting from the above mentioned procedure were fitted by a straight line (the fracture forming limit line, FFL) falling from left to right and bounded by grey areas corresponding to an interval of approximately 10% (above and below the FFL) due to the experimental uncertainty in its determination (see Figure 4 and Equation (8)):

$$\varepsilon_1 = -0.19\varepsilon_2 + 0.87 \quad (8)$$

The aforementioned uncertainty stems from the utilization of different tests to the determination of the FFL and from difficulties in measuring the strain gauge strains at the onset of fracture in case of tensile and hydraulic bulge tests.

As shown in Figure 4, the FFL of PVC presents a slope considerably different from that commonly observed in metals, which meet the dual condition of constant thickness strain and constant triaxiality ratio $\sigma_m/\bar{\sigma}$ at fracture (corresponding to a slope equal to '–1', [18]). In fact, the experimental slope equal to '–0.19' corresponds to a diminishing rate

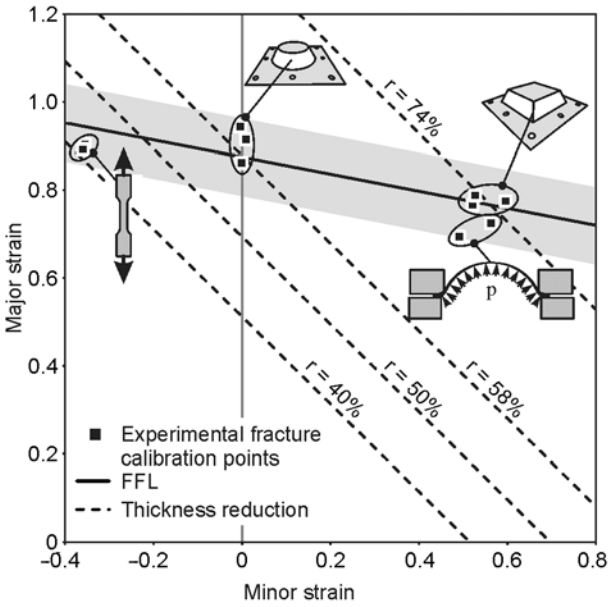

Figure 4. Fracture forming limit line (FFL) and iso-thickness reduction lines of the PVC sheets (in %)

of the accumulated damage when the strain loading paths evolve from the tension-compression (second quadrant) to the tension-tension (first quadrant) regions of the principal strain space.

The dashed grey lines in Figure 4 correspond to the iso-thickness reduction lines and are calculated from the incompressibility condition of the PVC sheets shown in Equation (9):

$$\varepsilon_1 + \varepsilon_2 = -\ln\left(1 - \frac{r}{100}\right) \tag{9}$$

where $r = (t_0 - t)/t_0$ is the reduction in sheet thickness (in %).

As seen in Figure 4, the reduction in sheet thickness at the onset of failure by fracture changes from 58% to 74% when the strain loading paths change from plane strain to biaxial stretching. This result is different from what is commonly observed in metals and, as shown in Section 3., will have a major influence on the correlation between the FFL and the standard non-coupled ductile damage criteria due to Cockcroft and Latham [14], Rice and Tracey [16] and Ayada *et al*. [17].

2.4. Fabrication of hole-flanged parts by multi-stage SPIF

The experiments in hole-flanging produced by multi-stage SPIF made use of rectangular PVC blanks with 220 mm side length and 3 mm thickness. All the blanks were cut from the supplied sheets and subsequently drilled to provide holes at the centre with diameters of 80 and 90 mm. Drilling was performed with a hole cutter and the resulting edges were carefully grinded with medium and fine grit sand paper to remove any sharp edges or burrs. The single point forming tool and the basic operating conditions utilized in the experiments were similar to those previously utilized for fabricating the conical and pyramidal SPIF parts (Section 2.3.).

The experimental work plan was designed with a twofold objective. Firstly, to investigate the feasibility of using multi-stage SPIF to produce hole-flanges in PVC blanks with pre-cut holes. Secondly, to analyse the feasibility of using the FFL to assess the formability of PVC under complex strain paths

Table 4. Experimental work plan for producing hole-flanged PVC parts by multi-stage SPIF

(Pre-cut) Hole diameter, D_0 [mm]	Tool diameter [mm]	Drawing angle of the intermediate stages, ψ_i [°]					
		1st	2nd	3rd	4th	5th	6th
80	10	65	70	75	80	85	90
90							

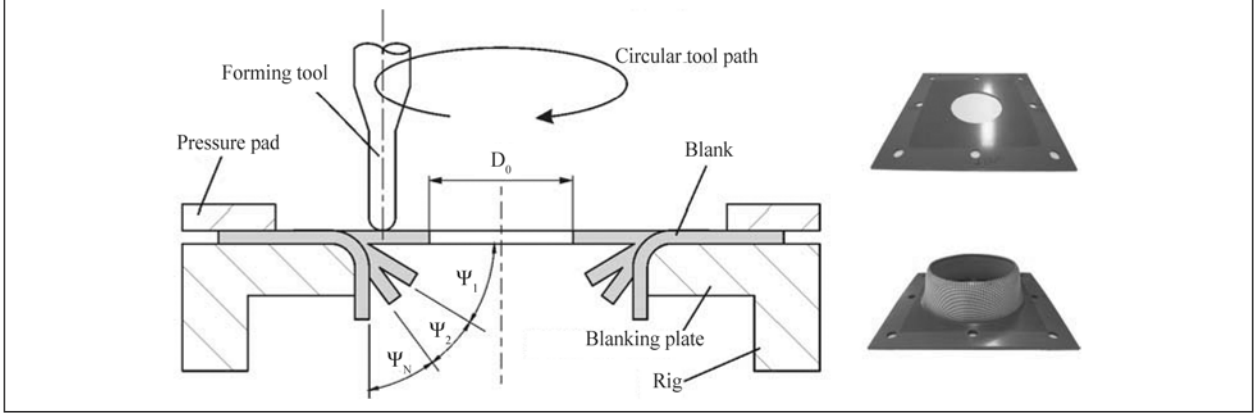

resulting from multi-stage SPIF. Each individual forming stage was produced with a constant drawing angle that was increased by $\Delta\psi = 5°$, between stages, from an initial value $\psi_1 = 65°$ until a limiting value $\psi_n = 90°$, corresponding to a hole-flange with vertical walls. Table 4 presents a summary of the experimental work plan.

3. Results and discussion

3.1. Plastic flow and failure

The experimental values of the major and minor in-plane true strains of selected conical and pyramidal parts produced by SPIF were measured along the meridional cross section in accordance to the method and procedure described in Section 2.2. after the parts reach failure or, in case of no-failure, at the end of the process. The results are plotted in the principal strain space (Figure 5).

As seen in Figure 5a the average values of the experimental in-plane true strains of the conical parts are aligned along the vertical axis corresponding to $\varepsilon_2 = 0$ and confirm that plastic flow takes place under plane strain proportional (or linear, $\beta = d\varepsilon_2/d\varepsilon_1 = 0$) loading conditions.

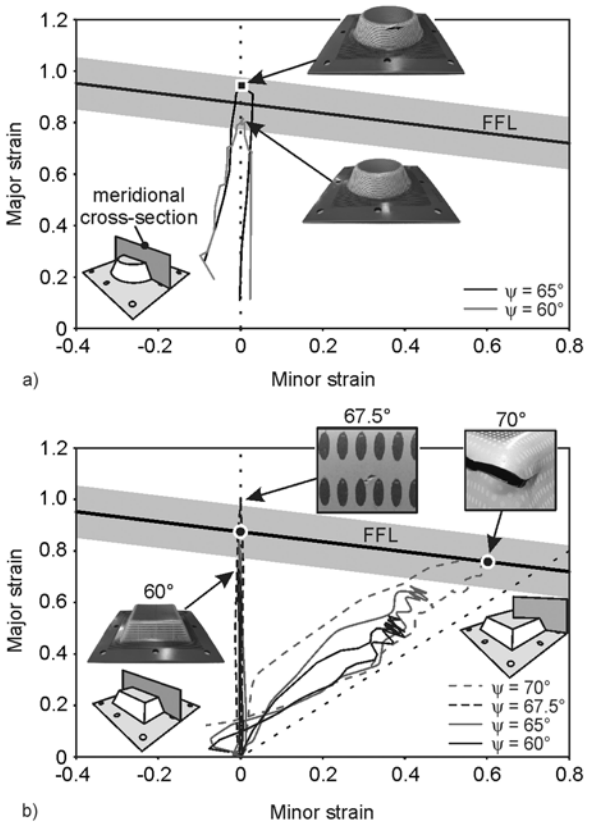

Figure 5. Experimental in-plane true strains in (a) conical and (b) pyramidal PVC parts produced by SPIF with different drawing angles. The photographs show a successful pyramidal part and details of the cracks that were found in two different regions

The agreement between the maximum values of strain at the onset of cracking and the FFL that was previously determined in Section 2.3. is very good. In fact, the maximum in-plane true strains of the conical part produced by SPIF with a drawing angle $\psi = 65°$, which failed by cracking along the circumferential direction (refer to the photograph in Figure 5a), are located above the FFL but inside the grey scattered area of 10% resulting from the aforementioned uncertainty in the determination of the FFL. In contrast, the maximum in-plane true strains of the other conical part produced by SPIF with a drawing angle $\psi = 60°$ are located below the FFL, as expected from a PVC part that was successfully fabricated by SPIF.

The results obtained for the pyramidal parts produced by SPIF further confirm the good agreement between the experimental values of the in-plane true strains at the onset of failure and the FFL. For example, the strain values of the pyramidal part produced by SPIF with a drawing angle $\psi = 67{,}5°$, which failed by cracking at the mid-side (undergoing plane strain loading conditions), are located above the FFL and those of the pyramidal part produced by SPIF with a drawing angle $\psi = 70°$, which failed by cracking at the corner (undergoing biaxial strain loading conditions), are very close to the FFL. The photographs included in Figure 5b show the details of cracks that were observed in both cases.

It is worth noting that all the other pyramidal parts produced by SPIF with smaller drawing angles than those mentioned above present maximum in-plane true strain values below the FFL. These results are in close agreement with the absence of cracks. See, for example, the pyramidal part that was successfully produced by SPIF with a drawing angle $\psi = 60°$ in Figure 5b.

The stress field corresponding to the aforementioned experimental values of strain at different locations over the conical and pyramidal PVC parts can be determined by means of the previously described methodology (Section 2.3.). Taken the conical part produced by SPIF with a drawing angle $\psi = 65°$ for example, the major and minor in-plane stresses are directly calculated from Equation (6) using an iterative analytical procedure based on the experimental values of the in-plane strains (refer to

the black square mark in Figure 5a) and the tensile and compressive stress-strain curves of Equation (1).

The iterative procedure is as follows. Firstly, it is necessary to obtain a rough approximation σ_1^0, σ_2^0, $\sigma_m^0 = \sigma_{kk}^0/3$ of the major, minor and average stresses by applying Equation (6) in conjunction with the tensile stress-strain curve of Equation (1), which is then utilized to obtain a new set of values for σ_1^1, σ_2^1, $\sigma_m^1 = \sigma_{kk}^1/3$ that already take into consideration the strength differential effect of the PVC yield surface. The overall procedure is applied until convergence, as it is shown in Figure 6.

As seen in Figure 6, the relative error arising from the utilization of the first approximation of the in-plane stresses, which were solely based on the tensile stress-strain curve of PVC, is rather small (below 10%). This means that the strength differential effect of PVC may be neglected from calculation of plastic flow and failure, as it was previously done by Alkas Yonan and coworkers [8, 9], who only considered the tensile stress-strain curve during the development of their non-linear viscoplastic material model for thermoplastics.

Hence, by taking the abovementioned simplification into account, the critical values D^{crit} of the non-coupled ductile damage models proposed by Cockcroft and Latham [14], Rice and Tracey [16] and Ayada *et al*. [17] can be easy and straightforwardly determined by means of Equations (7), without the need to apply inverse, cumbersome, calibration procedures based on numerical simulations. The experimental in-plane true strains utilized in these calculations were taken from the intersection of the FFL and the vertical axis ($\varepsilon_2 = 0$), and from the intersection of the FFL and the inclined strain-loading path corresponding to the corners of the pyramids ($\varepsilon_1 \cong 1.3\varepsilon_2$) (refer to the black circular marks in Figures 5b). The results are shown in Figure 7.

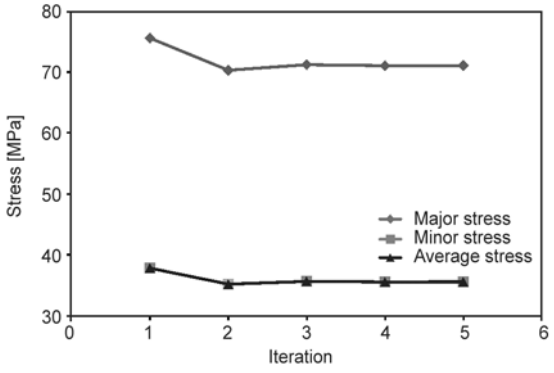

Figure 6. Iterative procedure for determining the major, minor and average stress values at the onset of cracking for a conical part produced by SPIF with a drawing angle $\psi = 65°$

As seen in Figure 7, and contrary to what has been recently observed in metals [19], the critical values of damage D^{crit} are significantly influenced by the strain loading conditions (from 21% in case of the damage models proposed by Cockcroft and Latham to 55 and 53% in case of the other damage models proposed by Rice and Tracey and Ayada *et al*., respectively). The fact that the slope of the FFL in Equa-

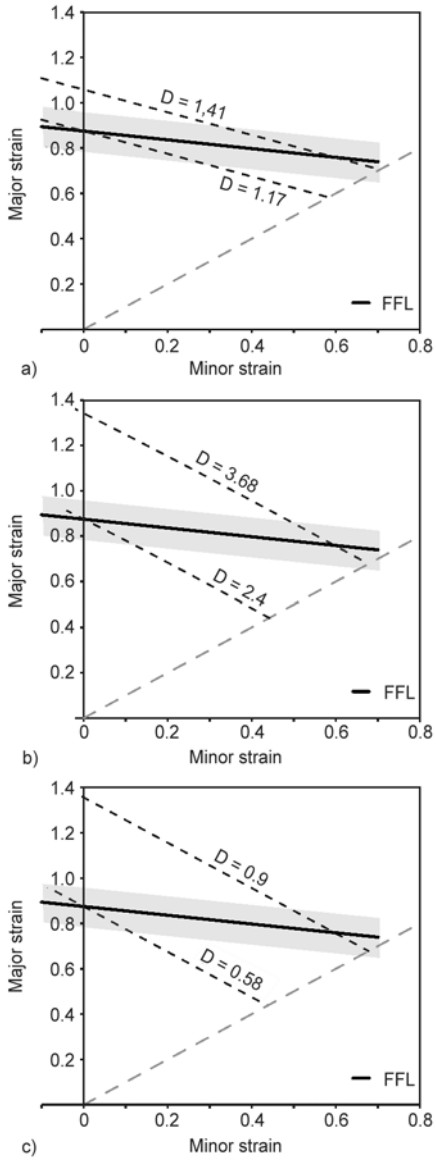

Figure 7. Principal strain space showing the FFL and two different black dashed lines corresponding to the iso-contours of the critical values of damage D^{crit} according to (a) Cockcroft and Latham [14] (b) Rice and Tracey [16] and (c) Ayada *et al.* [17] criteria

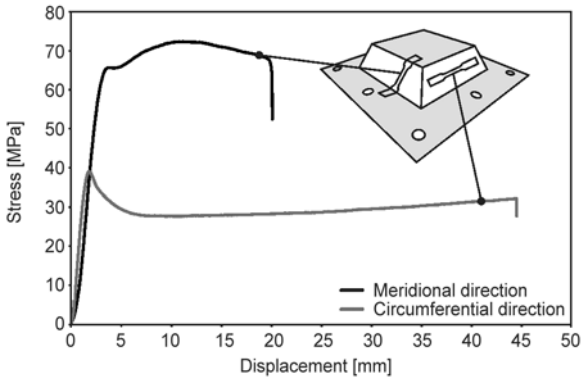

Figure 8. Stress-displacement curves obtained from tensile tests performed on specimens taken from the longitudinal and meridional directions along the mid-side of a pyramidal part produced by SPIF with a drawing angle $\psi = 60°$

tion (8) is significantly different from '–1' provides a justification for the above mentioned conclusion because PVC does not follow the conditions of failure by cracking under constant thinning and constant triaxiality ratio $\sigma_m/\bar{\sigma}$ that are typical of metals. The cause, however, is probably related to stable neck propagation during SPIF, a phenomenon that does not occur in metals.

Stable neck propagation along the meridional direction of PVC parts produced by SPIF is also responsible for inducing anisotropy that will result in different stress responses along the meridional and circumferential directions. This phenomenon is shown in Figure 8 and will have a major influence in multi-stage SPIF, as will be explained in the following section of the paper.

3.2. Hole-flanging of PVC sheets produced by multi-stage SPIF

The experiments in hole-flanging of PVC sheets produced by multi-stage SPIF were performed in accordance to the work plan and operating conditions that were previously described in Section 2.4. The black curves in Figures 9a and 9b are the envelopes of the greatest achievable experimental strains at selected forming stages in hole-flanging produced by SPIF. Each line corresponds to an intermediate drawing angle ψ_i listed in Table 2 and will be hereafter referred to as 'the strain envelope'. In case of the strain envelope corresponding to the last forming stage ($\psi_1 = 90°$) of Figure 9a, point '*A*' corresponds to near plane strain conditions at the middle of the wall flange, point '*B*' to biaxial strain conditions close to its edge and point '*C*' to tensile

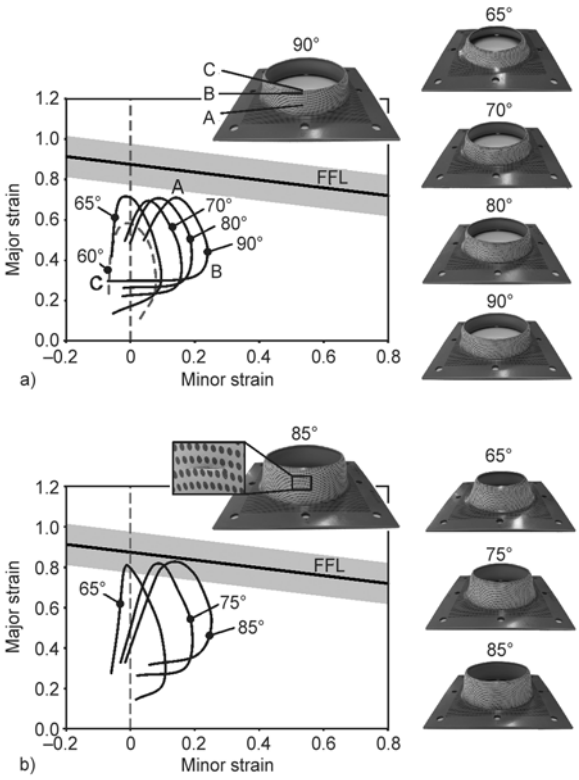

Figure 9. Experimental strain envelopes in the principal strain space for different intermediate configurations of hole-flanging produced by multi-stage SPIF. (a) Successful production using a PVC blank with an initial hole diameter of 90 mm. (b) Failure by cracking at $\psi_5 = 85°$ (refer to the detail) in case of a PVC blank with an initial hole diameter of 80 mm.

strain conditions along a very narrow region located at the edge of the hole. This result is similar to what has recently been observed in the hole-flanging of metals [19].

A detailed analysis of the evolution of the strain envelopes from the initial drawing angle $\psi_1 = 65°$ up to the last drawing angles included in Figures 9a and 9b, allows us to conclude that strain envelopes corresponding to intermediate forming stages with increasing values of ψ_i unveil significant differences between PVC and metals. In case of PVC, the second and following stages are characterized by expansion and translation of the strain envelopes towards higher values of the minor in-plane true strain ε_2. During expansion and translation the major in-plane true strain ε_1 remains approximately constant and equal to the values that had been reached during the first forming stage. This behaviour is different from that observed in metals, which experience expansion of the strain envelopes (from

the origin) under proportional loading conditions β = Const. [19].

As a result of this, the final height of the PVC wall flanges is practically identical to that reached at the end of the first forming stage. The subsequent forming stages mainly account for the increase in the diameter of the hole as a result of the decrease in sheet thickness ($\varepsilon_2 = -\varepsilon_3$), as the wall flange progressively rotates towards the vertical direction.

The cause of this behaviour is attributed to stable neck propagation during the first forming stage, which induces strong anisotropy and encourages plastic flow during the subsequent forming stages to be preferentially carried out in the circumferential direction instead of the meridional direction. The phenomenon was quantified in Figure 8 for a pyramidal part produced by SPIF with a drawing angle $\psi = 60°$.

Another conclusion arising from this investigation is that although non-coupled ductile damage models currently utilized in metals cannot apply to the analysis of failure in the hole-flanging produced by PVC because of the reasons that were explained in Section 3.1., the alternative analysis exclusively based on the FFL is reliable and accurate. In fact, the PVC blanks with pre-cut holes of 90 mm that were able to successfully withstand all the six intermediate forming steps of multistage SPIF, have the strain envelope corresponding to the last forming stage placed below the FFL (Figure 9a). On the contrary, the PVC blanks with pre-cut holes of 80 mm that failed by fracture during the fifth forming stage (corresponding to $\psi_5 = 85°$) exhibit a strain envelop inside the grey band area (i.e. inside the uncertainty interval of the FFL) and very close to the FFL (Figure 9b). In connection to this, it is worth noting that the influence of the uncertainty interval of the FFL on the overall performance of the process can be avoided if the sheet polymer parts are designed in order to have strain envelops below the lower bound of the grey band area.

4. Conclusions

The proposed methodology to determine the in-plane stresses and the accumulated damage at various positions over the surface of conical and pyramidal PVC parts directly from the experimental strain measurements avoids the need to utilize cumbersome inverse procedures based on numerical simulations.

The in-plane stresses are dependent on the strength differential effect of PVC but its influence was found to be rather limited (below 10%). This result opens the possibility of performing the calculations exclusively based on the tensile stress-strain curve and, thereby, avoids the need to perform stack compression tests.

The critical values of damage associated to standard non-coupled models due to Rice and Tracey and Ayada *et al*. experience 55 and 53% variation when the loading conditions change from plane-strain to biaxial stretching. This result prevents their utilization for assessing the formability limits of the SPIF of PVC sheets.

The critical value of damage associated to the non-coupled model due to Cockcroft and Latham experiences a smaller but still important variation (21%) with the change in loading conditions. This result derives from the fact that iso-damage lines have a slope equal to '–1/2' (instead of '–1') and, therefore, are closer to the slope '–0.19' of the fracture forming limit line (FFL) of PVC.

However, the overall results indicate that non-coupled damage models currently utilized in sheet metal forming applications should not be applied to characterize formability in the SPIF of PVC. The utilization of the FFL not only proved successful to describe formability in single-stage SPIF but also in multi-stage SPIF with complex strain paths.

Acknowledgements

Paulo Martins would like to acknowledge the financial support provided by the German Research Foundation (DFG) under research project SFB/TR 73 during his sabbatical license at the Institute of Forming Technology and Lightweight Construction of the Technical University of Dortmund.

Sammer Alkas Yonan would like to acknowledge the financial support provided by the German Research Foundation (DFG) under research project TE508/20-1.

References

[1] Glover G., Duncan J. L., Embury J. D.: Failure maps for sheet metal. Metals Technology, **4**, 153–159 (1977). DOI: 10.1179/030716977803292006

[2] Franzen V., Kwiatkowski L., Martins P. A. F., Tekkaya A. E.: Single point incremental forming of PVC. Journal of Materials Processing Technology, **209**, 462–469 (2008). DOI: 10.1016/j.jmatprotec.2008.02.013

[3] Le V. S., Ghiotti A., Lucchetta G: Preliminary studies on single point incremental forming for thermoplastic materials. International Journal of Material Forming, **1**, 1179–1182 (2008).
DOI: 10.1007/s12289-008-0191-0

[4] Martins P. A. F., Kwiatkowski L., Franzen V., Tekkaya A. E., Kleiner M.: Single point incremental forming of polymers. CIRP Annals – Manufacturing Technology, **58**, 229–232 (2009).
DOI: 10.1016/j.cirp.2009.03.095

[5] Silva M. B., Martinho T. M., Martins P. A. F.: Incremental forming of hole-flanges in polymer sheets. Materials and Manufacturing Processes, **28**, 330–335 (2013).
DOI: 10.1080/10426914.2012.682488

[6] Marques T., Silva M. B., Martins P. A. F.: Single point incremental forming of polymers. in 'Mechatronics and manufacturing engineering – Research and development' (Ed.: Davim J. P.) Woodhead Publishing, Oxford, 293–331 (2012).

[7] Silva M. B., Alves L. M., Martins P. A. F.: Single point incremental forming of PVC: Experimental findings and theoretical interpretation. European Journal of Mechanics – A/Solids, **29**, 557–566 (2010).
DOI: 10.1016/j.euromechsol.2010.03.008

[8] Alkas Yonan S., Haupt P., Kwiatkowski L., Franzen V., Brosius A., Tekkaya A. E.: A viscoplastic material model based on overstress for the simulation of incremental sheet forming of thermoplastics. AIP Conference Proceedings, **1353**, 803–808 (2011).
DOI: 10.1063/1.3589614

[9] Alkas Yonan S., Soyarslan C., Haupt P., Kwiatkowski L., Tekkaya A. E.: A simple finite strain non-linear visco-plastic model for thermoplastics and its application to the simulation of incremental cold forming of polyvinylchloride (PVC). International Journal of Mechanical Sciences, **66**, 192–201 (2013).
DOI: 10.1016/j.ijmecsci.2012.11.007

[10] Caddell R. M., Raghava R. S., Atkins A. G.: Pressure dependent yield criteria for polymers. Materials Science and Engineering, **13**, 113–120 (1974).
DOI: 10.1016/0025-5416(74)90179-7

[11] Alves L. M., Martins P. A. F.: Cold expansion and reduction of thin-walled PVC tubes using a die. Journal of Materials Processing Technology, **209**, 4229–4236 (2009).
DOI: 10.1016/j.jmatprotec.2008.11.015

[12] Spitzig W. A., Richmond O.: Effect of hydrostatic pressure on the deformation behavior of polyethylene and polycarbonate in tension and in compression. Polymer Engineering and Science, **19**, 1129–1139 (1979).
DOI: 10.1002/pen.760191602

[13] Lee J. H., Oung J.: Yield functions and flow rules for porous pressure-dependent strain-hardening polymeric materials. Journal Applied Mechanics, **67**, 288–297 (2000).
DOI: 10.1115/1.1305278

[14] Cockcroft M. G., Latham D. J.: Ductility and the workability of metals. Journal of the Institute of Metals, **96**, 33–39 (1968).

[15] McClintock F. A.: A criterion for ductile fracture by the growth of holes. Journal of Applied Mechanics, **35**, 363–371 (1968).
DOI: 10.1115/1.3601204

[16] Rice J. R., Tracey D. M.: On the ductile enlargement of voids in triaxial stress fields. Journal of the Mechanics and Physics of Solids, **17**, 201–217 (1969).
DOI: 10.1016/0022-5096(69)90033-7

[17] Ayada M., Higashino T., Mori K.: Central bursting in extrusion of inhomogeneous materials. Advanced Technology of Plasticity. Proceedings of the 2nd International Conference on Technology of Plasticity, Stuttgart, Germany, **1**, 553–558 (1987).

[18] Atkins A. G.: Fracture in forming. Journal of Materials Processing Technology, **56**, 609–618 (1996).
DOI: 10.1016/0924-0136(95)01875-1

[19] Cristino V. A., Montanari L., Silva M. B., Atkins A. G., Martins P. A. F.: Fracture in single point incremental forming predicted by ductile fracture mechanics. International Journal of Mechanical Sciences, in press (2013).

eXPRESS Polymer Letters Vol.8, No.5 (2014) 312–321
Available online at www.expresspolymlett.com
DOI: 10.3144/expresspolymlett.2014.35

A micro-Raman study of Cu-particulate-filled epoxy matrix composites

S. Tognana[1*], *W. Salgueiro*[1], *M. B. Valcarce*[2]

[1]IFIMAT, Fac. de Cs. Exactas, CIFICEN CONICET- Universidad Nacional del Centro de la Provincia de Buenos Aires, Pinto 399, (B7000GHG) Tandil, Argentina and Comisión de Investigaciones Científicas de la Provincia de Buenos Aires, calle 526 entre 10 y 11 (1900) La Plata, Argentina.
[2]División Electroquímica y Corrosión, INTEMA, CONICET, Universidad Nacional de Mar del Plata, Avenida Juan B. Justo 4302, (7608 FDQ) Mar del Plata, Argentina

Received 4 October 2013; accepted in revised form 23 December 2013

Abstract. A micro-Raman study is carried out to investigate the influence of the filler on the curing process of bisphenol A diglycidyl ether (DGEBA)-based epoxy matrix composites. The composites are cured (14 h at 393 K) with an anhydride (methyl tetrahydro phthalic anhydride, MTHPA, 100:90 pbw), catalyzed with a tertiary amine (0.7 pbw) and filled with a 30% volume of Cu particles of approximately 75 μm in diameter. The experimental results are compared with those obtained for the same epoxy resin unfilled and for the same composite with Cu filler but not catalyzed. The micro-Raman experimental technique is used to search for information on the curing process in different regions of the matrix, near to and far from the copper filler, taking into account the results of differential-scanning-calorimetry measurements performed on the same composites. The results provide information on the influence of the copper filler on the curing process of the epoxy matrix. Differences were observed in the peaks associated with the epoxy ring and the ester group as a function of the distance to the nearest copper particle, but no differences were observed between the different composites.

Keywords: *polymer composites, epoxy, micro-Raman spectroscopy*

1. Introduction

Epoxy resins are used in structural applications ranging from high-performance composites for aerospace applications to encapsulants for the microelectronics industry because of their high thermal resistance, high tensile strength and modulus, and good chemical resistance. It is well known that the most important factors that influence their performance are the molecular architecture, the ratio between the epoxide and the hardener, and the cure conditions, frequently at a high temperature, which determine the final properties of the material. The influence of the filler particles on the curing is still a subject of study and clearly depends on the nature of the particles [1–5]. Epoxy matrix composites find new applications every day in several areas of engineering and technology. For example, copper-filled composites have a high possibility of being used in microelectronics because the high thermal conductivity of copper allows the composite to be a good heat dissipator, which serves as protection to electronic devices [6, 7].

The matrix-particle interphases also play an important role. The physical properties of the polymeric composites can be significantly influenced by their thermal history; in fact, internal stresses are developed during the fabrication process and further thermal treatments. Microtechniques such as microcalorimetry [8], micro-Raman spectroscopy [9], and atomic-force microscopy have been used to study

*Corresponding author, e-mail: stognana@exa.unicen.edu.ar

composites, and these techniques allow for deep analyses of the physics at work in the interphase and the matrix of such composites, opening a wide range of possibilities. The advantages of microtechniques are exploited in the present study.

Regarding the DGEBA-anhydride system catalyzed by a tertiary amine, this material has been studied by various authors, and the kinetic model that governs the curing reactions has been extensively discussed [10, 11]. The curing has also been studied in a non-catalyzed system, in which it has been proposed that the reaction is initiated by impurities in a commercial tetrafunctional epoxy monomer [10]. We have recently observed that a non-catalyzed matrix filled with copper particles cures at a higher temperature than the related catalyzed system, and the results with differential scanning calorimetry is in preparation to be submitted. The present work is a continuation of a more general framework of study of epoxy-based composites containing different kinds of particles, in which some of the authors are involved. The main goals pursued are to investigate the effect produced by the inclusion of different kinds of particles, with a typical size of 100 μm, in an epoxy matrix and their influence on the thermal residual stresses [12–15]. The present work focuses on both types of composites (catalyzed and non-catalyzed) using micro-Raman spectroscopy. The aim of the work was to analyze the capability of this technique to garner information on the presence of inhomogeneities produced by the influence of filler (here, copper particles) on the curing of epoxy matrix composites. Information about the interphase between the copper and matrix in epoxy composites is sought in the framework of previous work of some of the authors, who study interphase phenomena in epoxy aluminum filled composites with different experimental techniques [13, 14, 16].

2. Experimental

The samples studied were prepared using as matrix diglycidyl ether of bisphenol A (DGEBA) epoxy resin, cured with an anhydride (methyl tetrahydro phthalic anhydride MTHPA) (100:90 pbw), filled with Cu powder with a particle diameter of ≈75 μm and with a filler volume fraction $\varphi = 30\%$. A catalyst (tertiary amine) was added (0.7 pbw) for the catalyzed sample. The catalyst was not used in the non-catalyzed sample. During the preparation of both samples, the mixture was stirred under vacuum until a good dispersion of the particles in the resin was attained. The compound was poured into a tubular Pyrex mold and placed in a horizontal position in a tubular oven. During the curing process, the mixture was heated to 393 K and maintained at a constant temperature for 14 h. Following the same procedure, a sample of DGEBA-MTHPA-catalyser without copper particles (blank epoxy, cured at 393 K) was prepared.

The Raman measurements were carried out using an Invia Reflex confocal Raman microprobe with an Ar^+ laser ($\lambda = 514$ nm) and with a diode laser ($\lambda = 786$ nm) in backscattering mode. An exposure time of 10 s and one accumulation were used with a 50× objective. The power of the laser was reduced using neutral density filters such that it did not exceed 1.05 mW.

3. Results and discussion

3.1. Raman spectroscopy, preliminary

The blank epoxy was studied with a wavelength excitation source of 786 nm; the results obtained (spectrum) are presented in Figure 1. It is important to emphasize that when studying the samples using a 514 nm excitation source, Raman results could not be obtained because only a saturation signal was observed.

A micro-Raman measurement was also performed in epoxy matrix composite filled with Cu particles (30% in volume), corresponding to the catalyzed system, using a 514 nm excitation source. A characteristic spectrum is also shown in Figure 1 for the purpose of comparing the results with those obtained when studying the blank epoxy. A third measurement with a 786 nm excitation source was carried out, but as can be seen in Figure 1, no Raman results were obtained. It is worth mentioning that a measurement of the non-catalyzed composite, using the 786 nm excitation source, yielded an analogous result to that of the catalyzed composite. We note that the measurements on the composites were performed in a region distant from the Cu particles to ensure that the result was obtained with the laser incident on the epoxy matrix.

From the analysis of both spectra shown in Figure 1, is possible to conclude that approximately the same peaks are present in the Raman spectra, although some differences are apparent for shift lower than 600 cm^{-1}, where the peaks associated with the composite are smaller than the peaks associated with the

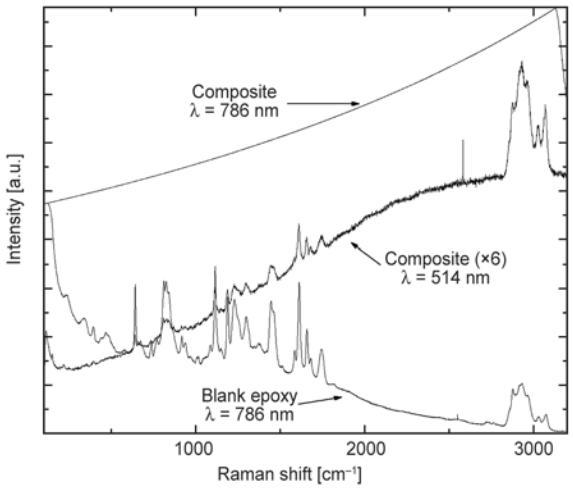

Figure 1. Raman spectra obtained from a blank epoxy sample and from a composite (30% Cu). The laser wavelengths used for excitation are indicated for each spectrum. The laser power remained unchanged for the same wavelength.

epoxy. Furthermore, it is important to note that a direct comparison cannot be performed because different excitation wavelengths were used.

We remark that the difficulties in selecting the excitation wavelength for these materials arise because both matrix and filler can be detected at the same time. The differences observed in the Raman spectra using sources with different excitation wavelengths can be attributed to different effects. The saturation in the epoxy sample caused by the 514 nm excitation could be associated with the strong fluorescence observed when short wavelengths (visible range) are used [17].

The opposite situation is observed for the copper-filled composites; in this case, the 514 nm excitation source allows a good spectrum to be obtained, while no results are gained from the spectrum obtained with the 786 nm wavelength. An explanation for the latter effect could be provided by the surface-enhanced Raman scattering (SERS) on Cu, by which a significant increase in the scattering intensity is produced. The SERS effect in Cu is expected for wavelengths longer than 580 nm [18], and therefore, at the 514 nm wavelength, this effect is absent. On the other hand Resonant Raman scattering can occurs when the energy of the exciting light lies in the absorption band of the sample. The UV-visible reflectance spectra of the oxides grown on Cu show that the absorbance peaks at 237, 314 and 380 nm together with the shoulders at 462 and 550 nm are characteristics of Cu_2O [19]. The 514 nm excitation source is nearer to some of the peaks mentioned and then the Resonant Raman scattering is present in Cu_2O. The intensity of the SERS effect is usually many times greater than the Resonant Raman [18]. This effect could be related to the good signal of epoxy obtained in the composites. This phenomenon must certainly be relevant when the Raman test is performed on or in the neighborhood of the Cu particles, but when the Raman measurement is performed on the epoxy matrix, the saturation is also observed, indicating that the incident radiation passes through of the matrix and ultimately reaches the copper surfaces.

The strong fluorescence and the difficulty that this fluorescence involves in the epoxies are well-known [20]; for example, using a laser source with same wavelength of our work, cycloaliphatic epoxy could not be studied; however, the hybrid systems of epoxy-methacrylate were free from fluorescence [21]. Then, the response of the epoxy systems to different wavelength excitation measurements is complex. Although there are signals of fluorescence in the composites that were studied using the 514 nm excitation source, the peaks can be easily analyzed. It is not clear yet if the fluorescence is lower in the composites and what the reason for this difference might be.

3.2. Composite DGEBA + HY 918 + 30% Cu, non-catalyzed

Micro-Raman spectroscopy was used to study composites filled with 30% Cu particles (by volume) in the non-catalyzed epoxy matrix using an excitation wavelength of 514 nm. The spectra were recorded at different positions along a straight line connecting two selected particles with a step size between measurements of ≈2 μm. In this mode the spatial resolution is ≈0.5 μm. A high confocality was used, allowing a best resolution at the expense of lower signal intensity. Depth resolution depends strongly on experimental setup being used besides of the optical properties of the sample. In this work, it was estimated that the scattered radiation originates from a volume with dimension of the order of 10 μm in depth.

The recorded spectra are labeled (E_i, i = 1, 2, …) according to the positions at which they were taken. In Figure 2, a micrograph is shown that indicates the line along which each spectrum was collected. The spectra obtained are presented in the same figure.

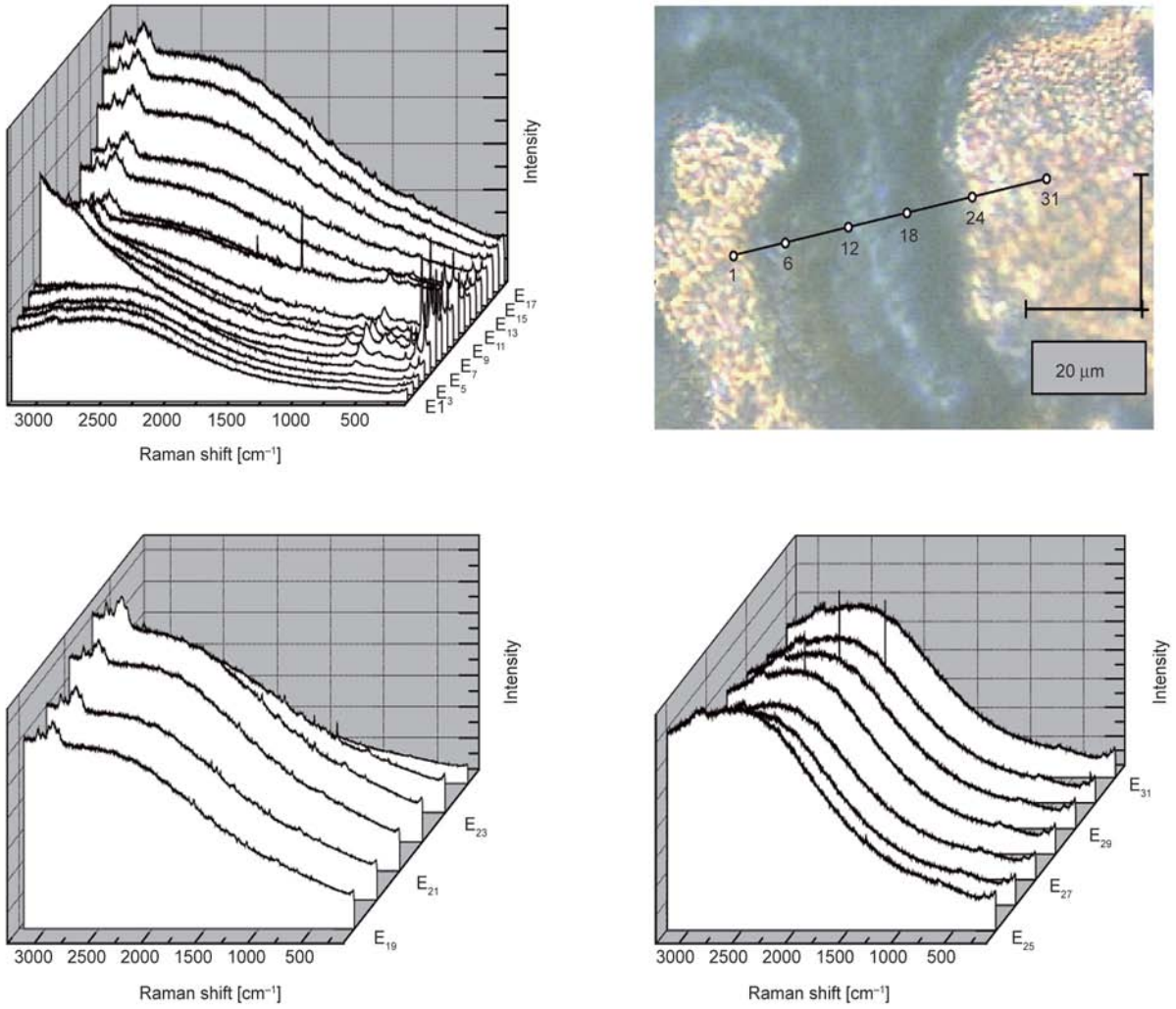

Figure 2. Micrograph and Raman spectra taken at different positions along a straight line connecting two selected copper particles in a DGEBA + HY 918 + 30% Cu composite. The recorded spectra are labeled (E_i, i = 1, 2, …) according to the positions shown on the micrograph.

In the spectra taken at positions N°1 to N°5, different peaks can be observed in the region at low Raman shifts (<1000 cm^{-1}), which belong to the Cu oxides. The Raman technique is sensitive to the presence of Cu oxides, and, in particular, it has been reported in the literature that Cu_2O exhibits peaks at 145, 220, 297, 411, 492, 633, and 786 cm^{-1} [18, 22]. In this work and, in particular, in the spectrum taken at position N°6, peaks at 149, 217, 300, 416, 505 cm^{-1} with a shoulder at 530, 650 and 802 cm^{-1} can be observed. These peaks could be attributed to Cu_2O, although a peak of the matrix would be superposed on the peak at 650 cm^{-1}. In addition, the identification of CuO with this technique is difficult to perform because the Raman scattering from CuO is much weaker than that from Cu_2O, and the main peak in the CuO spectrum lies too close to one of the most intense Cu_2O peaks.

A fact that deserves attention is that the peaks at 300 and 802 cm^{-1} are not observed in the spectrum taken at position Nº4; furthermore, there is a peak at 530 cm^{-1} that, in the spectrum taken at position Nº5, becomes a peak at 505 cm^{-1} with a shoulder. An expanded detail view of the spectra is shown in Figure 3. The observed changes can be explained by taking into account that in the first spectrum, the Raman measurement is taken on the polished surface of the particle, but the spectrum taken at position Nº5 corresponds to a measurement taken with the laser incident on an unpolished surface covered with epoxy matrix.

The Cu-oxide peaks are visible until the spectrum that was taken at position Nº18; therefore, the Cu oxide can be observed through the surface of the epoxy matrix. Between the spectra taken at positions Nº19 and Nº24, only the peaks corresponding

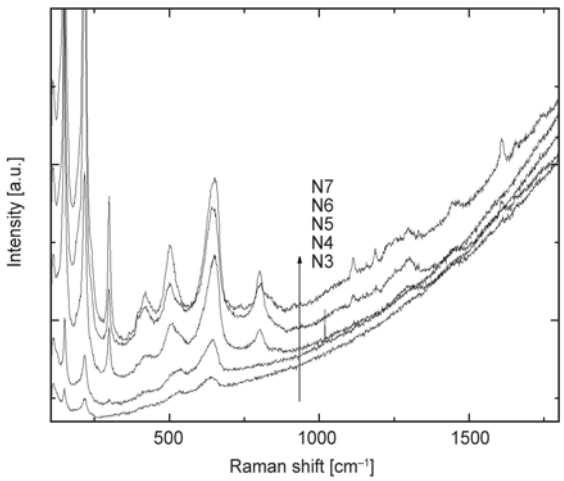

Figure 3. Raman spectra in the 100–1800 cm^{-1} Raman-shift region taken at positions near a copper particle

to the matrix are observed, but beginning with position Nº25, the measurements were once again taken with the laser incident on the surface of a copper particle, so the Cu_2O peaks are observed again.

Therefore, we can conclude that in some cases, the Raman measurements allow the simultaneous observation of results that can be attributed to the matrix and to the particle surface, indicating that the scattered radiation is collected from a volume between the sample surface and the copper particle. This is also supported by the fact that the peaks corresponding to the epoxy increase in intensity when the distance to the nearest particle increases. It is worth mentioning that the radiation can not pass through the copper surface, then the volume of collection of radiation can be limited for this surface.

A schematic picture based on the above explanation is presented in the diagram of panel a in Figure 4. In Figure 4b, the intensities of the peak that is characteristic of the epoxy at 1609 cm^{-1} (see below) for measurements taken at the different locations are also shown. As can be seen, the intensity increases when the distance to the nearest particle increases; this fact can be interpreted as a consequence of the greater epoxy volume where the scattering is produced.

The peaks corresponding to the epoxy matrix can be observed starting with the spectrum taken at position N°6. The most important peaks were observed at 1113, 1186, 1230, 1253, 1300, 1332, 1457, 1609, 1655, 1742 cm^{-1}, a shoulder at 2875, 2932, 2967, 3027 and 3070 cm^{-1}. The peaks located at Raman shifts higher than 2800 cm^{-1} could be associated with C–H vibrations [10] or CH_2 vibrations.

The peak at 1609 cm^{-1} is attributed to the aromatic ring (quadrant stretching) present in the epoxy monomer. In the literature, this peak has been reported at 1614 cm^{-1} [10, 23–25]. It is worth mentioning that there is a small shift of this peak compared with the results obtained from pure epoxy (see Figure 1), in which the peak is located at 1612 cm^{-1}. This difference is also present in the Raman spectrum of the catalyzed composite (Figure 1), and it could be attributed to residual stress remaining from the curing process [17, 26]. The peak at 1609 cm^{-1} can be clearly observed starting with the spectrum taken at position N°6; therefore, from this position on, the epoxy monomer can be observed.

The peak at 1457 cm^{-1} can be attributed to the matrix, and to be specific, it can be interpreted as two superposed peaks located at 1445 and 1460 cm^{-1}. Rocks *et al*. [10] attributed these peaks to the vibra-

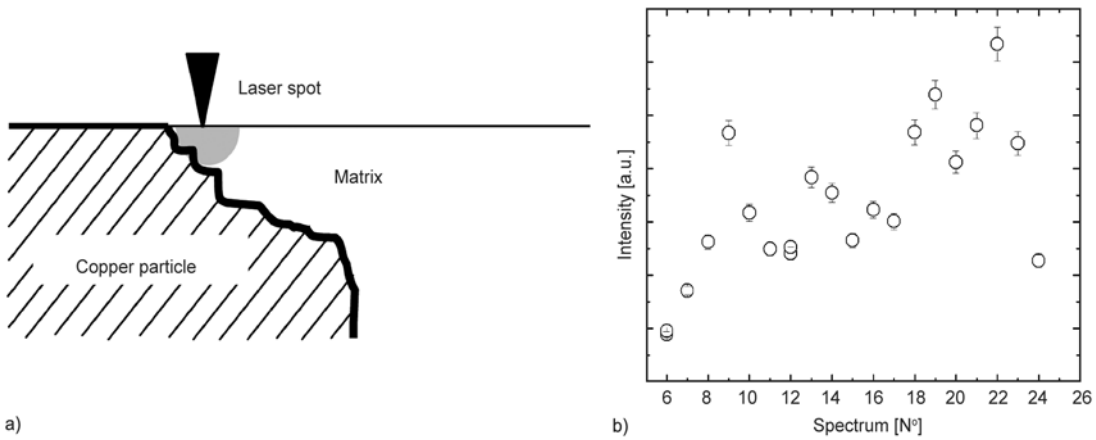

Figure 4. Schematic diagram of the incidence of the laser on the sample (a), the intensity of the peak at 1609 cm^{-1} is shown for the different positions (b)

tion δ CH_2 in the anhydride (1449 cm^{-1}) and the vibration δ CH_2 + δ_{as} CH_3 in the epoxy monomer (1470 cm^{-1}). On the other hand, Kister *et al*. [27] identified a vibration δ_{as} CH_3 at 1452 cm^{-1}, and Musto *et al*. [23] reported a peak at 1447 cm^{-1} belonging to the anhydride that is invariant during the curing.

The peak at 1300 cm^{-1} could be, according to Kister *et al*. [27], the superposition of three peaks located at 1313, 1302 and 1293 cm^{-1} and associated with the vibration δ_2 CH. These last two peaks, 1300 and 1457 cm^{-1}, are observed in the spectra obtained at positions N°5 and N°6, even though the peak at 1609 cm^{-1}, which is characteristic of the aromatic ring of the epoxy matrix, is observed weakly or not at all. This could be evidence of the formation of some organic complex at the matrix-particle interface.

On the other hand, the peak at 1113 cm^{-1} is clearly evident in the spectrum taken at position N°6 and could be attributed to the vibration of ether groups, C–O–C [9, 28], while the peak at 1186 cm^{-1} can be associated to the in-plane deformation of the aromatic ring [23].

The peaks at 1230 and 1253 cm^{-1} diminish in intensity in a complex way as the curing progresses, and in particular, the peak at 1253 cm^{-1} can be attributed to the epoxy ring [23]. Following similar methods to those reported in the literature to study the curing process [10, 23], the ratio of intensity of the peak at 1253 cm^{-1} (I_{1253}) with respect to the peak at 1609 cm^{-1} (I_{1609}) was calculated for the different spectra, and the values obtained are shown in Figure 5. To estimate the intensity of each peak, the experimental data were fitted using Lorentzian functions, and the values of the area under the curve were used. The values obtained vary for the different positions, with higher values in the region near the particle, *i.e.*, there are more epoxy rings or a worse-quality cure in this region. The variation in the values is primarily produced prior to the spectrum taken at position N°16, after which the values obtained exhibit a higher dispersion. The results can be interpreted by considering that the variation is produced in the zone in which the Cu-oxide peaks can also be observed in the Raman spectra. This gradual change could be explained by considering the Raman scattering as an average of the scattering at different depths, *i.e.*, as the contribution of the scattering at the interface plus the scattering in the bulk. Therefore, a gradual variation can be expected as a result of the higher scattering in the bulk matrix. In particular, from the behavior of the intensity of the peak at 1253 cm^{-1}, it could be concluded that a different number of open epoxy rings are present at the surface of the particle.

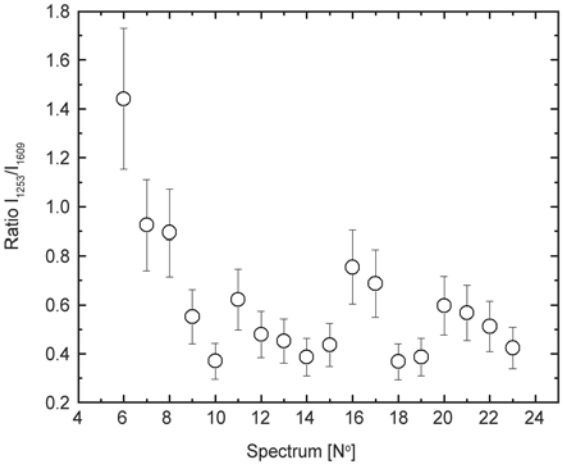

Figure 5. Ratio of the intensities of the peak at 1253 cm^{-1} with respect to the peak at 1609 cm^{-1} in the non-catalyzed composite. The spectra are labeled according to the positions at which they were recorded (see micrograph in Figure 2).

According to the literature [10, 23], the anhydride produces peaks at 1784 and 1854 cm^{-1} that can be assigned to C=O groups; as the curing progresses, these peaks decrease in intensity. In this case, these peaks were not observed, so it can be concluded that the anhydride conversion is approximately complete.

The peak at 1742 cm^{-1} is a broad peak and could be associated with the peak reported at 1734 cm^{-1}, which is characteristic of esterification involving the epoxy and anhydride groups (C=O aliphatic ester), and an increase of this intensity has been observed during curing [23].

3.3. Composite DGEBA + HY 918 + catalyst + 30% Cu

The DGEBA-anhydride system cured in the presence of a catalyst and containing a 30% volume fraction of Cu particles was studied using a 514 nm wavelength excitation source in a micro-Raman measurement along a straight line connecting two copper particles. Similar to the presentation of the results in the previous subsection, the spectra are labeled according to the locations at which they were collected in the composite. In Figure 6, the Raman spectra are shown, and the region between

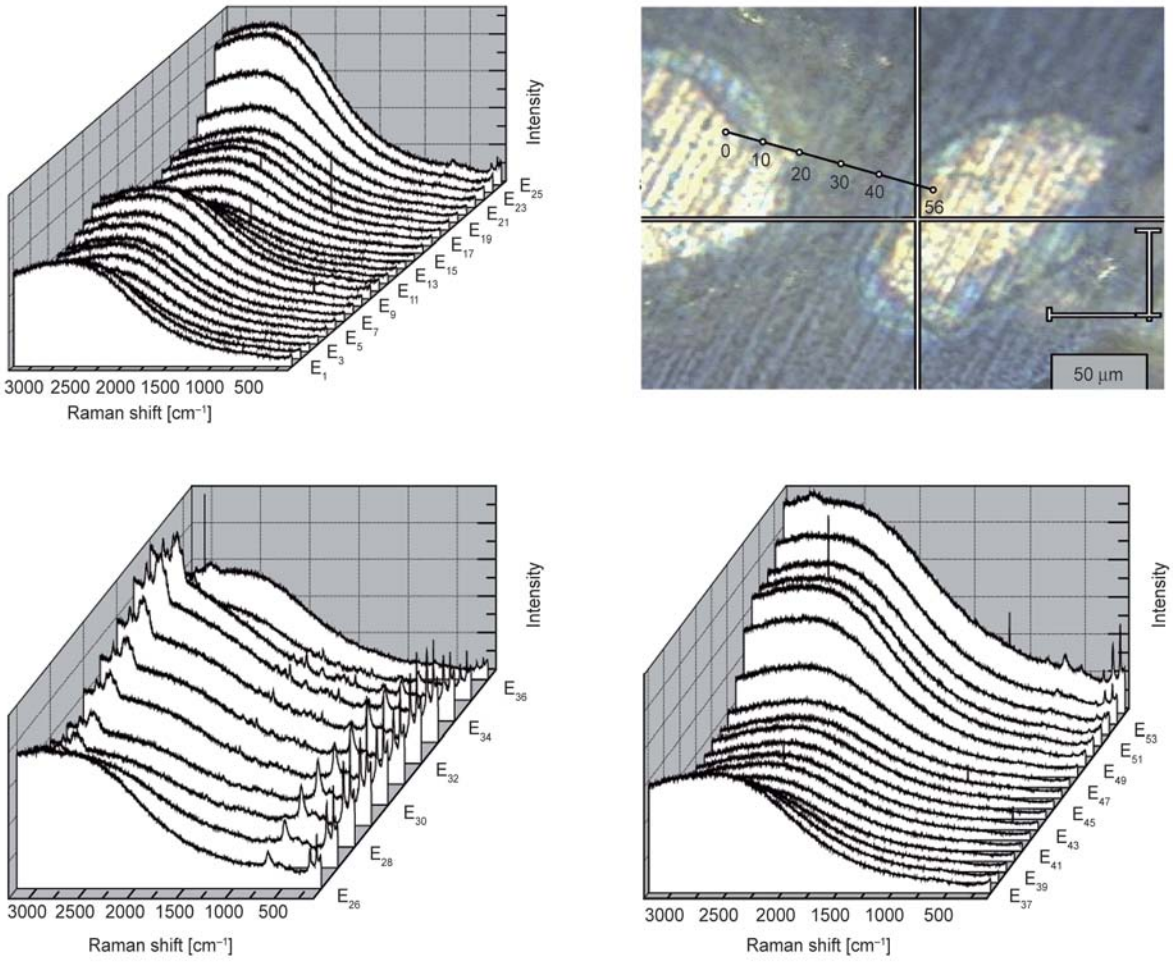

Figure 6. Micrograph and Raman spectra taken at different positions between two copper particles in the DGEBA + HY918 + catalyst + 30% Cu composite

the copper particles wherein they were collected is indicated in the micrograph.

As can be seen in Figure 6, various characteristic regions can be identified: First, from the spectrum taken at position Nº1 to the spectrum taken at position Nº25, only a small trace of the peaks corresponding to the Cu oxide can be observed, primarily in the spectra that were taken far from the particles. In the spectra taken from position Nº26 to position Nº36, the peaks associated with the Cu oxide are clearly visible, and the peaks corresponding to the epoxy matrix increase in intensity, indicating that both materials, the Cu oxide and the matrix, are clearly present in the Raman scattering. Therefore, the epoxy and the interface between the particle and the matrix contribute to the Raman scattering.

From the spectrum taken at position Nº37 onward, it is clear that the Cu-oxide peaks are barely observed, and it is clear that the epoxy peaks are absent, although in the spectrum taken at position Nº48 and subsequent spectra, the Cu-oxide peaks increase in intensity.

The peaks observed in the Raman spectra are the same that are observed in the non-catalyzed composites, so a further explanation of them will not be given. However, certain peaks will be analyzed. In the intermediate region of the Raman measurement line (in the spectra taken from position Nº28 to position Nº36), where the major changes in the peaks corresponding to the matrix are observed, the ratio of the intensity of the peak positioned at 1253 cm^{-1} (epoxy ring) with respect to the intensity of the peak at 1609 cm^{-1} was calculated. In addition, the broad peak at 1740 cm^{-1} was fitted using two Lorentzian functions, one centered at 1735 cm^{-1} and the other centered at 1747 cm^{-1}. The curve at 1735 cm^{-1} can be associated to ester formation involving the epoxy and anhydride groups, and the ratio of the intensity of this peak with respect to the intensity of the peak at 1609 cm^{-1} was calculated. The values of both intensity ratios, corresponding to the peak at

1253 cm^{-1} and the peak at 173 cm^{-1}, are shown in Figure 7. In the inset of the same figure, the fit to the experimental data using two Lorentzian functions is shown. The results obtained for the two investigated peaks demonstrate opposite tendencies and indicate that there are variations in the curing quality of the sample as a function of the measurement location with respect to the nearest copper particle. This fact was interpreted as arising from a higher number of epoxy rings near to the copper particle, meaning a lower esterification.

In both cases, the results indicate that there is a variation in the number of open epoxy rings depending on the distance to the particle, although a definitive conclusion regarding the general behavior could not be obtained from the data. However, a change in the cure kinetics due to the presence of copper is not discarded, and more information is necessary. In this study, the kinetics has not been considered because the aim is focused on finding differences between different regions of the composites. The use of micro-Raman spectroscopy to study the kinetics in the different regions of the composites increases the experimental complexity.

No significant variations are observed in the Raman spectra when a comparison is made between the spectra obtained from the catalyzed and non-catalyzed samples; therefore, it is possible to assume a similar chemical structure of the molecular chains in both samples. On this topic, Rocks *et al*. [10] proposed models for the possible types of curing reactions depending on whether there is a catalyst present. When there is a catalyst present, the catalyst reacts with the epoxy monomer, forming a zwitterion that contains an ammonium cation and a carboxylate anion. This carboxylate may be considered as an active center for alternating chainwise copolymerization. In the case of the non-catalyzed reaction, hydroxyl groups, which are present in the epoxy monomer, attack the anhydride, forming a monoester with a free carboxyl group. The free carboxyl group then reacts with an epoxy ring to yield a diester and a new hydroxyl group, allowing the curing process to continue. For more details about the chemistry that is involved, see for example the equations that are presented in the studies [10, 23]. Therefore, although the curing reaction is different for the two samples, the Raman results do not permit the identification of unambiguous differences between them [10]. Preliminary results, which were obtained using DSC in epoxy-copper composites with and without a catalyst, have shown changes in the curing exothermic peaks; thus, a change in the curing kinetics can be expected. This finding may also provide evidence that the copper is interacting chemically with the epoxy during the curing and that this interaction is not limited to be only a 'physical' interaction due to the high thermal conductivity of the copper. It is worthwhile mentioning that the time for curing is 14 hours, which is sufficient to reach thermal equilibrium. Studies that use other types of filler are also underway; for example, the use of quartz [15] or aluminum [13, 14, 16] particles has shown to not have an influence on the curing as important as the copper particles, although these materials have a thermal conductivity lower than that of copper. A study that uses particles with a thermal conductivity similar to that of copper could address the problem of discerning the difference between the physical and chemical interaction of copper with the epoxy.

On the other hand, secondary reactions during the curing process of epoxy forming ether groups can be produced [10, 23]. In this work, although some peaks that can be attributed to ether groups can be observed, evidence of a high degree of etherification with respect to esterification was not observed in the composites that were studied.

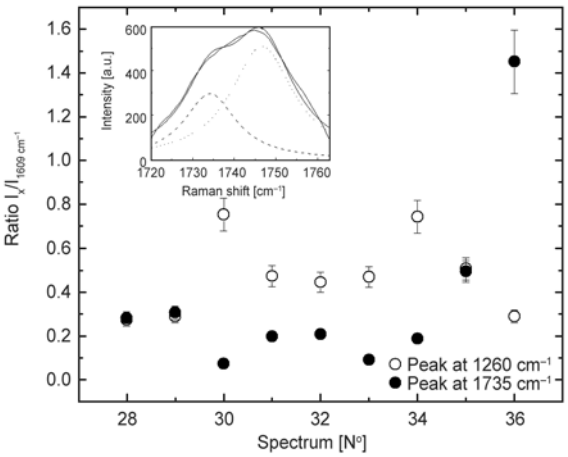

Figure 7. Ratios of the intensities of the peak at 1253 cm^{-1} and the peak at 1735 cm^{-1} with respect to the peak at 1609 cm^{-1} in the catalyzed composite. The spectra are labeled according to the positions at which they were recorded. In the inset, the fit of the peak at approximately 1740 cm^{-1} with two Lorentzian functions is shown.

4. Conclusions

In this work, epoxy-based particulate composites, both catalyzed with a tertiary amine and non-catalyzed, were studied using micro-Raman spectroscopy. The spectra were recorded in different regions of the sample: the Cu particles and the epoxy matrix.

Because of the characteristics of the samples, two different excitation sources were used, and it was found that it is possible to study the copper-filled composites using an excitation with a wavelength of 514 nm, while when an excitation with wavelength of 786 nm is used, saturation is observed. These results are interpreted as an effect of the Cu particles.

The peaks observed in the spectra were characterized according to their sources. The peaks corresponding to the Cu oxide are observed even when the measurements are performed on the matrix; this indicates that the particle surface can be seen below the matrix, due to the penetration of the laser radiation into the matrix.

The peak associated with the epoxy ring was analyzed by evaluating the ratio of its intensity with respect to the intensity of the peak at 1609 cm^{-1} that is associated with the aromatic ring. These ratios were analyzed in both the catalyzed and non-catalyzed composites, and their behavior, as a function of the distance to the nearest copper particle, is interpreted as a variation of the epoxy-ring signal when the distance to the nearest particle increases. The results are attributed to a smaller number of open epoxy rings near the particles. A similar evaluation for the peak associated with the ester-group formation was also performed in the non-catalyzed sample, and the opposite behavior with respect to that corresponding to the epoxy ring was observed.

No differences were observed between the different curing reactions in the presence or absence of the catalyst.

Acnowledgements

The authors acknowledge to Comisión de Investigaciones Científicas de la Provincia de Buenos Aires, SECAT- Universidad Nacional del Centro de la Provincia de Buenos Aires (Argentina), Universidad Nacional de Mar del Plata and the National Research Council (CONICET).

References

[1] Omrani A., Simon L. C., Rostami A. A.: The effects of alumina nanoparticle on the properties of an epoxy resin system. Materials Chemistry and Physics, **114**, 145–150 (2009).
DOI: 10.1016/j.matchemphys.2008.08.090

[2] Hong S. G., Wang T. C.: The effect of copper oxides on the curing of brominated epoxy resins. Thermochimica Acta, **237**, 305–316 (1994).
DOI: 10.1016/0040-6031(94)80188-6

[3] Fu Y., Zhong W-H.: Cure kinetics behavior of a functionalized graphitic nanofiber modified epoxy resin. Thermochimica Acta, **516**, 58–63 (2011).
DOI: 10.1016/j.tca.2011.01.016

[4] Tarrío-Saavedra J., López-Beceiro J., Naya S., Gracia C., Artiaga R.: Controversial effects of fumed silica on the curing and thermomechanical properties of epoxy composites. Express Polymer Letters, **4**, 382–395 (2010).
DOI: 10.3144/expresspolymlett.2010.48

[5] Harsch M., Karger-Kocsis J., Holst M.: Influence of fillers and additives on the cure kinetics of an epoxy/anhydride resin. European Polymer Journal, **43**, 1168–1178 (2007).
DOI: 10.1016/j.eurpolymj.2007.01.025

[6] Mamunya Y. P., Davydenko V. V., Pissis P., Lebedev E. V.: Electrical and thermal conductivity of polymers filled with metal powders. European Polymer Journal, **38**, 1887–1897 (2002).
DOI: 10.1016/S0014-3057(02)00064-2

[7] Boudenne A., Ibos L., Fois M., Majesté J. C., Géhin E.: Electrical and thermal behavior of polypropylene filled with copper particles. Composites Part A: Applied Science and Manufacturing, **36**, 1545–1554 (2005).
DOI: 10.1016/j.compositesa.2005.02.005

[8] Van Assche G., Van Mele B.: Interphase formation in model composites studied by micro-thermal analysis. Polymer, **43**, 4605–4610 (2002).
DOI: 10.1016/S0032-3861(02)00298-7

[9] Spencer P., Wang Y., Walker M. P., Wieliczka D. M., Swafford J. R.: Interfacial chemistry of the dentin/adhesive bond. Journal of Dental Research, **79**, 1458–1463 (2000).
DOI: 10.1177/00220345000790070501

[10] Rocks J., Rintoul L., Vohwinkel F., George G.: The kinetics and mechanism of cure of an amino-glycidyl epoxy resin by a *co*-anhydride as studied by FT-Raman spectroscopy. Polymer, **45**, 6799–6811 (2004).
DOI: 10.1016/J.POLYMER.2004.07.066

[11] Mauri A. N., Riccardi C. C.: The effect of epoxy excess on the kinetics of an epoxy–anhydride system. Journal of Applied Polymer Science, **85**, 2342–2349 (2002).
DOI: 10.1002/app.10867

[12] Tognana S., Salgueiro W., Somoza A., Pomarico J. A., Ranea Sandoval H. F.: Influence of the filler content on the thermal expansion behavior of an epoxy matrix particulate composite. Materials Science and Engineering: B, **157**, 26–31 (2009).
DOI: 10.1016/j.mseb.2008.12.003

[13] Goyanes S., Rubiolo G., Salgueiro W., Somoza A.: On the free volume evolution in a deformed epoxy composite. A positron annihilation study. Polymer, **46**, 9081–9087 (2005).
DOI: 10.1016/j.polymer.2005.07.020

[14] Goyanes S., Rubiolo G., Marzocca A., Salgueiro W., Somoza A., Consolati G., Mondragon I.: Yield and internal stresses in aluminum filled epoxy resin. A compression test and positron annihilation analysis. Polymer, **44**, 3193–3199 (2003).
DOI: 10.1016/S0032-3861(03)00229-5

[15] Marzocca A. J., Somoza A., Goyanes S. N., Salgueiro W., König P.: Characterization of free volume in particulate-filled epoxy resin by means of dynamic mechanical analysis and positron annihilation lifetime spectroscopy. Polymer International, **51**, 1277–1284 (2002).
DOI: 10.1002/pi.1017

[16] Tognana S., Salgueiro W., Somoza A.: On the matrix-particle interphase in epoxy-based composites. Journal of Alloys and Compounds, **495**, 588–591 (2010).
DOI: 10.1016/j.jallcom.2009.10.058

[17] Colomban Ph., Gouadec G., Mathez J., Tschiember J., Pérès P.: Raman stress measurement in opaque industrial C_f/epoxy composites submitted to tensile strain. Composites Part A: Applied Science and Manufacturing, **37**, 646–651 (2006).
DOI: 10.1016/j.compositesa.2005.05.004

[18] Hamilton J. C., Farmer J. C., Anderson R. J.: *In situ* raman spectroscopy of anodic films formed on copper and silver in sodium hydroxide solution. Journal of the Electrochemical Society, **133**, 739–745 (1986).
DOI: 10.1149/1.2108666

[19] Valcarce M. B., Vázquez M.: Phosphate ions used as green inhibitor against copper corrosion in tap water. Corrosion Science, **52**, 1413–1420 (2010).
DOI: 10.1016/j.corsci.2009.12.015

[20] Xue G.: Fourier transform raman spectroscopy and its application for the analysis of polymeric materials. Progress in Polymer Science, **22**, 313–406 (1997).
DOI: 10.1016/S0079-6700(96)00006-8

[21] Asmussen S., Schroeder W., dell'Erba I., Vallo C.: Monitoring of visible light photopolymerization of an epoxy/dimethacrylate hybrid system by Raman and near-infrared spectroscopies. Polymer Testing, **32**, 1283–1289 (2013).
DOI: 10.1016/j.polymertesting.2013.08.005

[22] Niaura G.: Surface-enhanced Raman spectroscopic observation of two kinds of adsorbed OH^- ions at copper electrode. Electrochimica Acta, **45**, 3507–3519 (2000).
DOI: 10.1016/S0013-4686(00)00434-5

[23] Musto P., Abbate M., Ragosta G., Scarinzi G.: A study by Raman, near-infrared and dynamic-mechanical spectroscopies on the curing behaviour, molecular structure and viscoelastic properties of epoxy/anhydride networks. Polymer, **48**, 3703–3716 (2007).
DOI: 10.1016/j.polymer.2007.04.042

[24] deBakker C. J., George G. A., St John N. A., Fredericks P. M.: The kinetics of the cure of an advanced epoxy resin by Fourier transform Raman and near-IR spectroscopy. Spectrochimica Acta Part A: Molecular Spectroscopy, **49**, 739–752 (1993).
DOI: 10.1016/0584-8539(93)80098-U

[25] Merad L., Cochez M., Margueron S., Jauchem F., Ferriol M., Benyoucef B., Bourson P.: *In-situ* monitoring of the curing of epoxy resins by Raman spectroscopy. Polymer Testing, **28**, 42–45 (2009).
DOI: 10.1016/j.polymertesting.2008.10.006

[26] Bennett J. A., Young R. J.: Micromechanical aspects of fibre/crack interactions in an aramid/epoxy composite. Composites Science and Technology, **57**, 945–956 (1997).
DOI: 10.1016/S0266-3538(97)00023-7

[27] Kister G., Cassanas G., Vert M.: Effects of morphology, conformation and configuration on the IR and Raman spectra of various poly(lactic acid)s. Polymer, **39**, 267–273 (1998).
DOI: 10.1016/S0032-3861(97)00229-2

[28] Wang Y., Spencer P.: Hybridization efficiency of the adhesive/dentin interface with wet bonding. Journal of Dental Research, **82**, 141–145 (2003).
DOI: 10.1177/154405910308200213

eXPRESS Polymer Letters Vol.8, No.5 (2014) 322–335
Available online at www.expresspolymlett.com
DOI: 10.3144/expresspolymlett.2014.36

LBL coating of type I collagen and hyaluronic acid on aminolyzed PLLA to enhance the cell-material interaction

M. Y. Zhao[1,2], *L. H. Li*[1,2*], *B. Li*[1], *C. R. Zhou*[1,2]

[1]Department of Materials Science and Engineering, Jinan University, 510630 Guangzhou, China
[2]Engineering Research Center of Artificial Organs and Materials, Ministry of Education, 510630 Guangzhou, China

Received 6 October 2013; accepted in revised form 23 December 2013

Abstract. The aim of the present work is to assemble extracellular matrix components onto poly (L-lactic acid) (PLLA) films using layer-by-layer (LBL) depositing method to enhance the cell-material interaction. To introduce charges onto the hydrophobic and neutral PLLA surface so that the electronic assembly can be processed, poly (ethylene imine) (PEI) was covalently bonded to modify the PLLA films. Positively charged collagen I (Col I) was then deposited onto the aminolyzed PLLA film surface in a LBL assembly manner using hyaluronic acid (HA) as a negatively charged polyelectrolyte. The PEI modification efficiency was monitored via X-ray photoelectron spectroscopy (XPS) measurements. The results of Surface Plasmon Resonance (SPR) and Water contact angle (WCA) monitoring the LBL assemble process presented that the HA/Col I deposited alternately onto the PLLA surface. The surface topography of the films was observed by Atomic force microscope (AFM). *In vitro* osteoblast culture found that the presence of Col I layer greatly improved the cytocompatibility of the PLLA films in terms of cell viability, cell proliferation and Alkaline Phosphatase (ALP) expression. Furthermore, osteoblast extensions were found to be directed by contact guidance of the aligned Col I fibrils. Thus, these very flexible systems may allow broad applications for improve the bioactivity of polymeric materials, which might be a potential application for bone tissue engineering.

Keywords: *biocompatible polymers, layer by layer, type I collagen, hyaluronic acid, osteoblast*

1. Introduction

Specially designed three-dimensional biomaterials provide one of the fundamental tools to shape and guide the tissue development *in vitro* and *in vivo*. Modern biomaterials for tissue-engineering applications must possess excellent biocompatibility, easily processed to have a variety of configurations, mechanical strength that needed for the creation of macroporous scaffold that will retain its structure after implantation as well as appropriate biodegradability. They should also provide the necessary physical and chemical cues to guide cell attachment, growth and differentiation to finally obtain a three-dimensional tissue [1, 2] in which surfaces play an important role in a biological system for most biological reactions occurring at surfaces and interfaces [3]. Thus, the development of biomaterials for tissue engineering is to design a material with relatively high mechanical strength and create perfect surfaces which can provoke specific cellular responses and direct new tissue regeneration. However, few scaffolds can fit all of these qualifications. Among the variety of biomaterials used in the biomedical field, poly (L-lactic acid) (PLLA) is one of the polymers most widely employed for the regeneration of different tissues or organs, like bone [4, 5], cartilage [6] and skin [7], because of its relatively good mechanical and manufacturing properties. However, the biomedical applications of PLLA are hampered to a certain extent by its high hydro-

*Corresponding author, e-mail: tlihuali@jnu.edu.cn

phobicity and lack of physiological activity [8, 9]. It has been shown in a number of studies that PLLA does not provide a favorable surface for cell attachment and proliferation due to lack of specific cell-recognition signals [10]. Since implants and tissue-engineering scaffolds interact with the biological environment via their surface, modification of the outermost part of materials may be sufficient to tailor its biocompatibility, while the bulk properties of the material are maintained [11]. However, the high hydrophobicity of PLLA material has made it difficult to get a stable biomimetic coating of hydrophilic natural biomacromolecules, and the lack of reactive side-chain groups to covalent cell-recognition molecules to PLLA molecules has limited its further application in tissue engineering and other biomedical areas. Though different strategies have been proposed [12, 13] like coating [14], plasma treatment [15], and entrapment [16], very few examples have considered assembling homogenously extracellular matrix components onto the PLLA film or scaffold. Therefore, how to introduce functional groups or molecules to polyester surfaces, which ideally adjust cell/tissue biological functions, becomes more and more important.

In nature, the biological world is built up via precise self-assembly of biomacromolecules. It provided a great inspiration for researchers to explore an engineered scaffold via macromolecules self-assembly [17, 18]. Layer-by-layer (LBL) electrostatic self-assembly (ESA) of polyelectrolytes constitutes a novel and promising technique to modify surfaces in a controlled way [19, 20]. This technique allows the build-up of thin films simply by the alternating deposition of polyanions and polycations to modify polymer surface and reconstruct ECM environment on biopolymer surface [21, 22]. The ideal cell-carrier scaffold should probably mimic the naturally occurring environment in the cell matrix, for bone which is composed of collagen, especially type I, proteoglycans and hydroxyapatite. These biomacromolecules form physically or chemically cross-linked networks, regulating the expression of phenotype of the osteoblast and supporting osteogenesis both *in vitro* and *in vivo* [23, 24]. Therefore, many natural extracellular matrixes (ECM)-like macromolecules, such as hyaluronic acid (HA) or collagen, have been incorporated into the 3-D scaffolds for bone regeneration [24–26].

Herein we describe the assembly of ECM components onto the biodegradable PLLA using LBL assembly technique to enhance the cell-material interaction after PEI modification. HA and Col I were chosen as the building blocks to build biomimetic layers on the PLLA films. Col I, an important ECM component of native bone tissue, has been verified as possessing osteoprotective ability [24, 25]. Moreover, it is positively charged in solution below isoelectric point [26], which allows Col I to be used as a polycation in a LBL assembly system, on which various polyanions can be adsorbed. In addition, HA is a major component of the extracellular matrix and of the synovial fluid, is also a negatively charged polyelectrolyte which has been used widely in a LBL assembly system [26, 27]. Therefore, Col I and HA were chosen as the polymer combination because of both the cytocompatibility and the layer stability in culture medium (pH 7.4) [26]. This work concerns the construction of assembly films with HA and Col I on the PEI modified PLLA film surface via LBL deposition. The culture of osteoblast *in vitro* showed that the cytocompatibility of the modified PLLA was improved obviously. In addition, osteoblast cells spread well in an aligned morphology and higher ALP expression only on the Col I terminated films. Therefore the ability to construct ECM-based films on PLLA may be a potential application for bone tissue engineering.

2. Materials and methods

2.1. Materials

Poly-L-Lactide (PLLA, P), (M_W 100,000 with a viscosity of 2.3 dL/g) was obtained from Shandong Institute of Medical Instruments, China. Hyaluronic acid (HA, H, 1000 kDa) was obtained from Shandong Freda Bio-Chemical Co., Ltd, China. Poly (ethylene imine) (PEI, P) (M_W 250 000 g/mol) was from Sigma, St. Louis, MO. N-(3 Dimethylaminopropyl)-N′-ethylcarbod- imide hydrochloride (EDAC) and N-Hydroxy-Succinimidr (NHS) were obtained from Aldrich, China. High glucose DMEM and fetal calf serum were from Hyclone, China. 0.25% trypsin-EDTA was purchased from GIBCO, China. Osteoblast was supplied by Guangzhou First Affiliated Hospital of Jinan University. All other chemicals and reagents used were of analytical grade.

2.2. Extraction and purification of collagen type I

Tail tendons were obtained from adult white rats. After pre-treated with 75% ethanol for 30 min, rat tail tendons were kept in 0.05 M Tris-HCl buffer (pH = 7.5) for overnight. Then the chopped tendons were transferred and partially dissolved in 0.5 M acetic acid (HAc) for 3 days. Pepsin was then introduced into the above solution at a ratio of 10:1 (w/v) and kept stirring for another 5 days under 4°C. The obtained solution was filtered with cloth to remove the insoluble impurities and then precipitated out using 0.7 M sodium chloride (NaCl); under acidic conditions, this concentration of NaCl has been shown to precipitate collagen types I–IV [28]. The collagen protein was collected via filtration and re-dissolved in 0.5 M HAc, followed by thorough dialysis against 0.5 M HAc. The final dry products were obtained by freeze-drying.

2.3. Fabrication of PLLA films

PLLA powder was dissolved in dichloromethane with magnetic stirring to obtain a homogenous 1.5 wt% solution, and then kept still for 10 minutes to remove the bubbles. Afterwards the solution was cast into a glass culture dish in a fume hood at room temperature. Plastic wrap was introduced to cover the dish to prevent fast evaporation of the solvent. After evaporation of the solvent, the translucent PLLA films with the thickness of 5 μm were taken out from the dish and cut into discs with the diameter of 14 mm.

2.4. Surface modification of PLLA with PEI

The two-step activation method was used for surface functionalization of PLLA, which has been described previously [29] and with some modification. Briefly, PLLA films were kept in 0.1 M NaOH for 20 min and then washed by distilled water and immersed in ethanol/water (1:1, v/v) at room temperature for 30 min to clean organic residue. After washing, the PLLA films were transferred into EDC and NHS (3 and 5 mg/mL, respectively, pH = 6.0) aqueous solution for 30 min under constant shaking. After rinsing with a large amount of water, films were dipped in 10 mg/mL PEI (pH 7.4) solution and kept shaking for 5 h at 40°C before being cleaned and dried.

2.5. Surface snalysis of PEI-modified PLLA

The surface chemical composition of PLLA film before and after PEI treatment was investigated by X-ray Photoelectron Spectroscopy (XPS). XPS spectra of the samples were acquired on an ESCALAB 250 XPS spectrometer. High resolution spectra of C1s, O1s, and N1s peaks were also recorded and used to quantify the chemical composition of polar groups on the surface of the PEI-treated films by deconvolution and curve-fitting of the peaks.

2.6. Build up of the polyelectrolyte multilayered films (PEMs)

Col I (5 mg/mL in 0.2 M acetic acid) and HA (5 mg/mL in MilliQ water) were used for Zeta potential measurement, which was determined with a Zetasizer Nano-Zs. Before each measurement, stored Col I and HA solution were adjusted to different pH value in Hepes-NaOH buffer (pH = 6.5). Measurements were carried out in triplicate at 25°C on three independent preparations. According to the Zeta potential results (Table 1) we chose pH = 5 as the working solution, as Col I easily forms fibers in a relative high pH value [30]. Then the LBL assembly processes were carried out as the following steps (the schematic illustration was shown in Figure 1).

Table 1. Zeta potential of Col I and HA under pH = 5; results are the means±SD of three independent experiments

Samples	HA	Col I
Zeta potential [mV]	–50.07±8.42	24.73±1.10

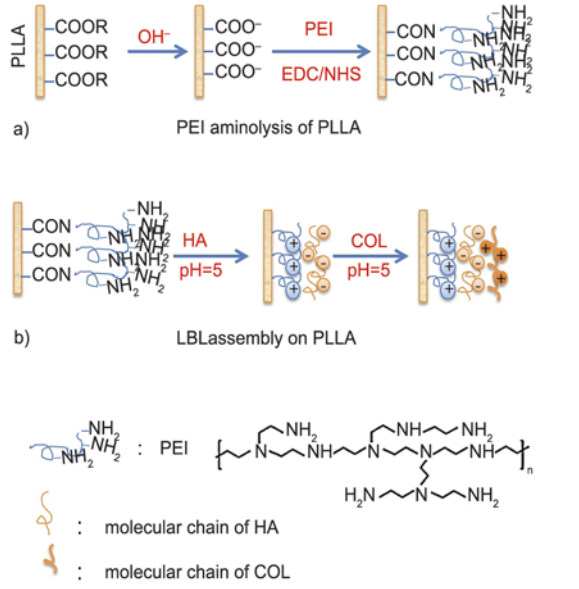

Figure 1. Schematic illustration of the surface modification strategy of PLLA, a) PEI modification of PLLA, b) build-up of polyelectrolyte multilayer

First, the films were immersed into HA (1 mg/mL in MilliQ water, pH = 5) aqueous solution for 15 min following with MilliQ water (pH = 5) washing. Then, the films were placed into the Col I solution (1 mg/mL in 0.2 M Hac, pH = 5) for 20 min, following by MilliQ water (pH = 5) washing in a row. By repeating those steps, multilayers were built up to 10 and 11 layers, which abbreviated as $PP(HC)_5$ (PLLA substrate modified with PEI plus 5 bilayers of HA and Col I) and $PP(HC)_5H$ (PLLA substrate modified with PEI plus 5 bilayers of HA and Col I plus HA); the PLLA film and PLLA film modified with PEI were abbreviated as P and PP respectively. Finally, the films were dried with flow of nitrogen.

2.7. Characterization of PEM formation by surface plasmon resonance (SPR) and water contact angle (WCA) measurements

The construction process of the PEM was monitored by SPR (IBIS Technologies B.V.) and static WCA measurements. SPR is based on the detection of changes in the refractive index (RI) at the gold-liquid interface of the SPR gold sensor surface caused by the adsorption of molecules. The resulting change in the SPR angle shift [m°] is proportional to the mass (Γ) of adsorbed molecules on the surface as shown by Equation (1) [31]:

$$122\ m° \approx 1\ ng/mm^2\ (\Gamma) \quad (1)$$

Hence, subsequent adsorption of layers should lead to a step-wise change in angle shift, which demonstrates multilayer formation. To detect PEM formation, the sensor used here was spin-coated with an ultrathin layer of PLLA at first. After chemical modification with PEI as described above, the sensor was mounted on the prism. Shift in resonance angles from 10 regions of interest defined on the sensor surface were recorded using the SPR software. LBL assembly on PEI-modified sensor was not started until a stable basal curve was obtained. HA solution was flowing over the sensor surface for 15 min, then MilliQ water (pH = 5) was used to rinse for 3×5 min times. Col I solution was used for another 20 min before rinsed again with MilliQ water (pH = 5). This process was repeated several times. The assembly process was monitored in-situ by angular scan mode; the averaged value of angle shift was given by the software of the device.

WCA measurement was performed using a sessile drop method with an OCR 15 plus device from Dataphysics, (Filderstadt, Germany). Water drops with a volume of 1 μL were placed onto the sample which was fixed on a cover slide with double-side tape. 5-Point measurements once a water droplet contacted the sample surface for 15 seconds were performed at positions selected randomly. Thereafter, the contact angles were determined with specific software and the average value of the 5-point measurements was regarded as the contact angle of the samples.

2.8. Atomic force microscopy (AFM) analysis

The surface morphology of the PLLA films was obtained by AFM in the tapping mode. AFM measurements were performed in ambient conditions at room temperature using an Auto Probe CP Research AFM (Thermo Microscopes Inc., Sunnyvale, CA, precently named Veeco Instruments). Images were scanned using a tip with typical spring constant of 3 N/m, a resonant frequency of ~80 kHz (MPP-21123, Veeco Instruments). The scan area was 5×5 and 2×2 μm respectively. Image processing and data analysis were performed using Proscan Image Processing Software Version 2.1 provided with the instrument.

2.9. Osteoblast culture

Osteoblast isolated from the skull of 1–2 day newly born SD rat was used for cell culture experiments *in vitro*. The cells were grown in culture petri dishes (100 mm) with high-glucose DMEM medium supplemented with 10% (v/v) fetal bovine serum (FBS). Cell culture was maintained in an incubator equilibrated with 5% CO_2 at 37°C. Cells after almost confluent were washed once with sterile PBS and followed by treatment with 0.25% (w/v) EDTA-trypsin for 5 min at 37°C. Cells were harvested and resuspended in culture medium after centrigugation for 5 min at 1000 r/min. Before cell seeding, the P, PP, $PP(HC)_5$ and $PP(HC)_5H$ films were placed into the 24 well tissue culture plates (TCPS, 24 Well) and sterilized by 75% ethanol and then were incubated in PBS for 1 day to exchange the ethanol and further were exchanged with cell culture medium overnight. Next, 1 mL of osteoblast suspension ($2.5 \cdot 10^4$ cells/mL) was dropped directly onto the surface of the films. Media was changed every two days during this experiment.

2.10. Cell viability and proliferation

The control and the modified P films were placed on the bottom of TCPS. Live/dead staining was carried out to evaluate cell viability using Calcein-AM (live cell: green) and Propidium Iodide (dead cell: red) staining reagents kit (abcam, Hongkong) at 3 and 5 days with a seeding density of $2.5 \cdot 10^4$ cells/well. The cell viability was calculated according to Equation (2) (n = 3):

$$\text{Cell viability} = \frac{\text{number of green–stained cell}}{\text{number of green–stained cell} + \text{number of red–stained cell}} \quad (2)$$

Where the green-stained cells presented live cells and the red-stained cells represent dead cells.

The cell proliferation ratio was assessed by MTT (3-(4, 5-dimethylthiazol-2-yl)-2, 5-diphenyl tetrazolium bromide) assay. After incubated for 2, 4, and 6 days with a seeding density of $2.5 \cdot 10^4$ cells/well, 20 μL MTT solution was added to each well and then incubated at 37°C for 4 h. Thereafter, 200 μL dimethylsulfoxide (DMSO) was added after supernatant medium was removed and the absorbency value (OD value) was recorded at a wave length of 490 nm.

2.11. Cell distribution and morphology observation

To observe the morphology of the osteoblast, the samples were transferred into new 24 well plates, rinsed three times with PBS (5 min/times), and followed by fixing with 2.5% glutaraldehyde (GA) at 4 °C for 30 min. After thoroughly rinsing with PBS, samples were gradiently dehydrated by ethanol and freeze-dried. Thereafter, samples were coated with gold for SEM observation.

To further observe the cell cytoskeleton distribution under laser confocal scanning microscope (CLSM), the cell-films constructs were taken out from the well plate and fixed for 15 min with 3.7% formaldehyde in PBS. After properply rinsed with PBS, the cells were permeabilized with 0.5% (v/v in PBS) Triton X-100 for another 15 min. After rinsing twice again with PBS the non-specific binding sites were blocked by incubation with 3% non-fat dry milk in PBS at 4°C for 1 hour. Filamentous actin was stained by incubatation with rhodamine-conjugated phalloidin (Biotium, USA) for 30 min in darkness at room temperature. Samples were followed by incubation with DAPI (Invitorgen, USA) for 10 min at 37°Cto visualize the Nuclei.

2.12. Alkaline phosphatase (ALP) activity test

ALP is known to be associated with bone metabolism and differentiation of osteoblasts. To assay for ALP activity, cells were cultured on films for 7 and 14 days at an initial seeding density of $2.5 \cdot 10^4$ cells/well. At harvest, cell layers were washed with PBS and a volume of 200 μL of 0.2% Triton X-100 was added to each well to study the lysis of cells. The total intracellular protein content in the cell lysates was measured spectrophotometrically using a BCA protein assay (Nanjing Jiancheng Bioengineering Institute, China) according to the manufacturer's instructions. ALP activity was assayed as the release of p-nitrophenol from p-nitrophenyl phosphate using a commercial kit (Nanjing Jiancheng Bioengineering Institute, China). Aliquots of the same solutions used for calculating total protein content were assayed for measuring ALP activity. Results were expressed as ALP activity (U/gprot) normalized by the total protein content.

2.13. Statistics

All data are represented as mean values±standard deviations (SD). Statistical analysis was performed using origin with ANOVA test (One way). The number of samples has been indicated in the figures and table captions. Statistical significance was considered for $P<0.05$ (*), $P<0.01$ (**) and $P<0.01$ (***).

3. Results and discussion

3.1. X-ray photoelectron spectroscopy (XPS)

XPS is an effective method to characterize the chemical composition of surfaces. For plain PLLA (Figure 2a), two peaks appeared in the XPS survey spectrum, which could be assigned to the elements carbon and oxygen. After PEI modification (Figure 2b), a new nitrogen peak emerged. The quantities of different elements for the PLLA modifica-

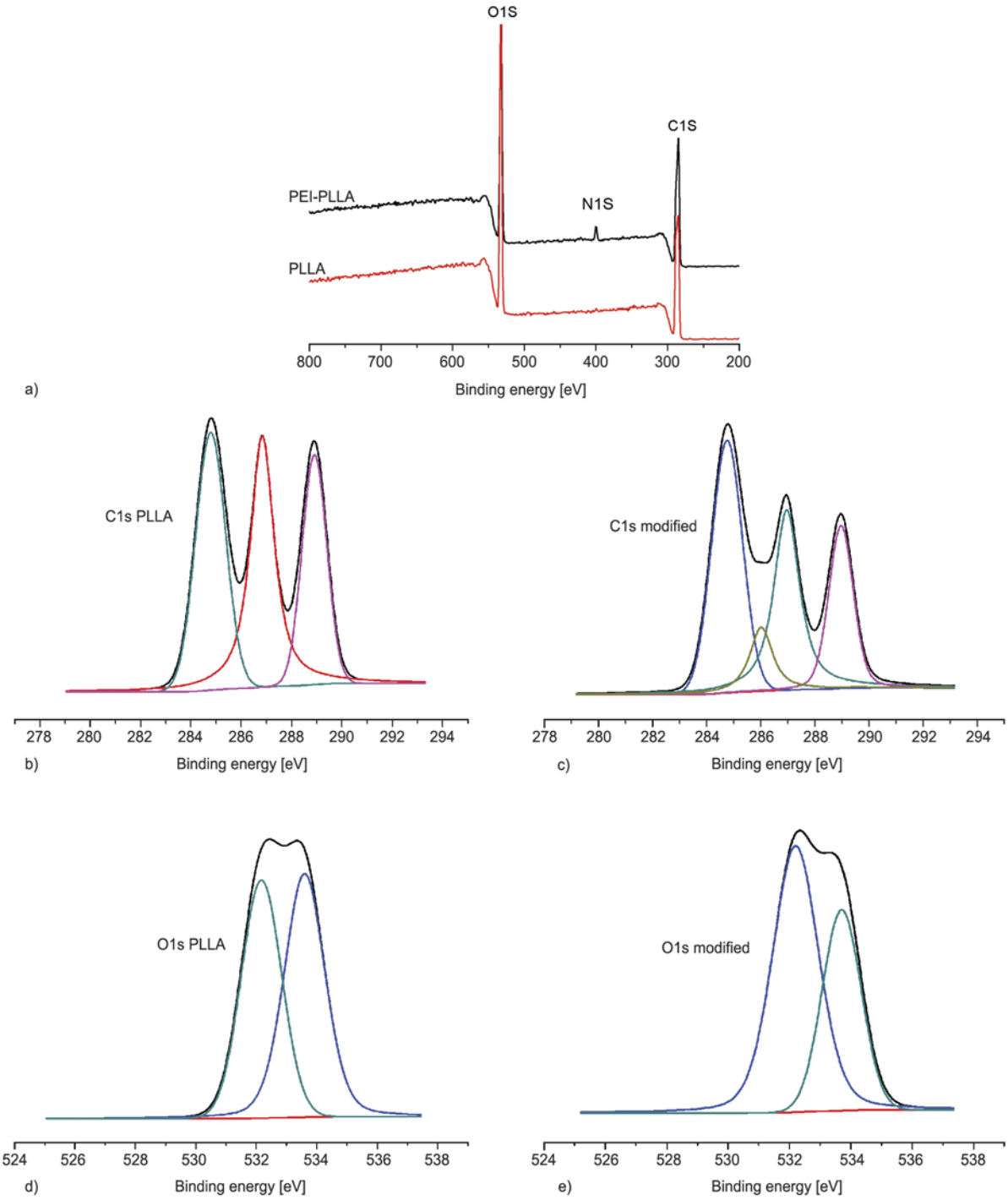

Figure 2. XPS survey spectra for different PLLA surfaces and fitting analysis of the C1s and O1s spectra to quantify the different functional groups at the surface of plain PLLA and PEI-PLLA, a) XPS survey spectra of different PLLA surfaces, b) C1s spectra of PLLA, c) C1s spectra of PEI-PLLA, d) O1s spectra of PLLA, e) O1s spectra of PEI-PLLA

Table 2. Atomic percentages on the surface of different PLLA samples obtained from the XPS measurements

Sample	C [%]	N [%]	O [%]
P	58.18	0.17	41.58
PP	60.16	2.85	36.27

tion are listed in Table 2. These data are a further proof for immobilization of PEI onto PLLA films. Curve-fittings of high-resolution spectra for the different elements on blank and PEI-modified PLLA surface are shown in Figure 2. For C1s core level spectrum, PLLA contains three peaks at binding energy (BE) of 284.78, 286.83, and 288.91 eV,

which was attributed to the C–H, C–H_2 or C–H_3 binding, C–O and C=O or COOH groups respectively, in correspondce well with the chemical structure of PLLA. After modification by PEI, a new type of carbon bond, attributed to the C–N binding appeared, it can be ascribed to covalent binding from PEI amino groups to carboxylic groups of PLLA.

For O1s core-level spectra, there are two types of oxygen bonds on blank PLLA, which was ascribed to –C–O–C– or C=O bonds. After the chemical reaction between the carboxylic groups and the amino groups, the content of C=O bond decreased due to replacement by the amide bond, which is confirmed in Figure 2.

3.2. Multilayer formation

To assemble extracellular matrix components onto the surface of PLLA film to improve its cell affinity, HA and Col I are used as the building blocks to cover the PLLA films with a multilayer thin coating. The HA/Col I alternate deposition for individual layers on PLLA film was monitored *in situ* with the SPR. The SPR technology allows time-resolved monitoring of dynamic processes and is therefore also an attractive alternative method for ultrathin film characterization.

The adsorbed mass (Equation (1)) of polyelectrolytes after washing was presented by SPR measurement (Figure 3). The multilayer growth seemed to be linear in all cases. It must be pointed out here that the collagen deposition behaviour was somewhat different from that of HA. For HA, a slight increase was recorded immediately after the introduction of HA to the analytical chamber, due to the negative charged HA adsorbing on the aminolyzed positive charged PLLA film surface through electrostatic attraction. After washing a little increase indicates that there was a mass increase after the washing procedure, as the HA is known to be highly hydrophilic and is able to bind large amounts of water [32], so the mass increase may be due to the trap of water in HA. Similar trend was found in the Col I formation on the surface except that there is mass decrease after the washing step. Overall, it can be obviously observed in Figure 3 that the adsorbed mass increased dramatically with the layer deposition.

Static WCA measurements have been widely applied to determine the change of terminal layer composition during assembly of multilayers and were used here to study wettability after the deposition of each layer. Figure 3 presented that, after modification of PLLA with PEI, a slight drop in WCA value occurred. During the first modification step with HA, there is a drop occurred while after again the adsorption of Col I, a slight increase in WCA was appeared. Thereafter, a regular multilayer formation process was observed indicated by oscillation of WCA with a continuous drop. The alternating contact angles between HA and Col I layers contributed to the change in the composition of the terminating molecule layer. Since pure Col I films have been characterized as quite hydrophobic (WCA ≈ 110°) [33],

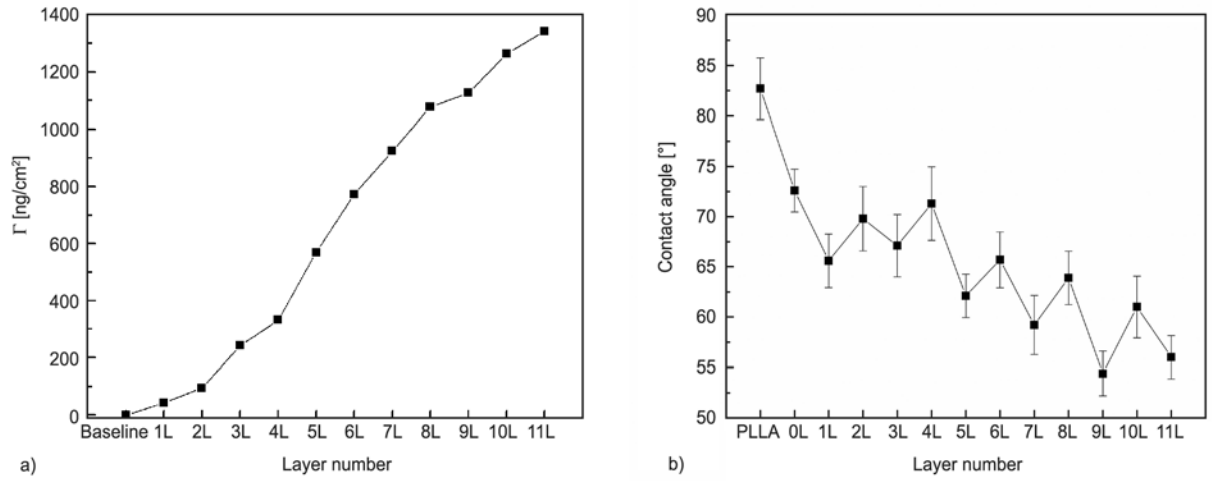

Figure 3. Accumulated mass during multilayer formation up to 11 layers calculated from SPR and changes of WCA during the multilayer formation). (0–11; 0 = poly (ethylene imine), all odd numbers = HA and even numbers = Col I). (The procession is based on the alternating adsorption of oppositely charged HA and Col I onto a positively charged pre-modified PLLA substrate), a) accumulated mass calculated from SPR, b) WCA value during the multilayer formation

while HA as hydrophilic (WCA ≈ 30°) [34]. The difference in WCA between the layers indicated a dominance of either HA or Col I in the outer layers after the corresponding coating step. Overall, the change of the WCA indicated that the hydrophilicity of the PLLA surface was greatly increased by modification with the alternate deposition of HA/Col I.

3.3. Atomic force microscope (AFM)

AFM measurement presented the surface morphology of the P (a, b) and PP $(HC)_5$ (c, d) film as shown in Figure 4. Results showed that there was no significant feature on the surface of the PLLA film while after the alternate deposition of HA/Col I, the topography displays large and long fibers whose width ranges from 100 to 120 nm and which were several micrometer long. These fibrils are tightly entangled into networks in a large scale (Figure 4c) while assembled to an aligned form in a relative small scale (Figure 4d). *In vivo*, collagen fibrils are arranged in complex three-dimensional arrays, often in an aligned manner to fulfill certain biomechanical functions. This aligned collagen fibrils organization *in vitro* has proved to impact cellular function, including adhesion, orientation, proliferation and differentiation [35, 36].

3.4. The cytocompatibility of the modified PLLA films

The alternatively deposition of HA and Col I onto the PEI modified PLLA films provided the possibility of improving the film's cytocompatibility. Firstly, osteoblast culture was performed to assess the cell response to the modified PLLA films as a function of layer number. The results show that all the modified PLLA films could effectively increase the cell proliferation (Figure 5) and viability (Equation (2)) (Figure 6 and Table 3) compared with the control PLLA film. An overall improvement in the cell–material interaction was achieved when Col I sup-

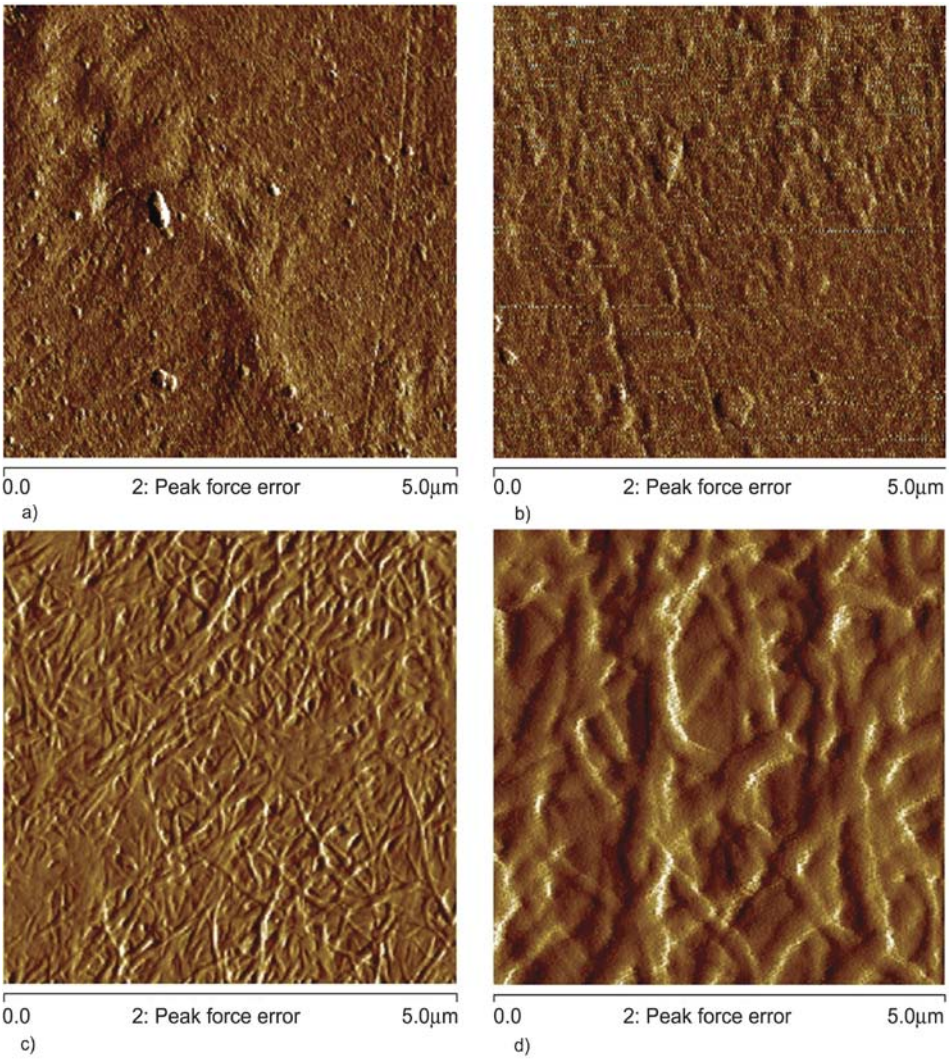

Figure 4. AFM image of the P (a, b) and PP$(HC)_5$ film (c, d)

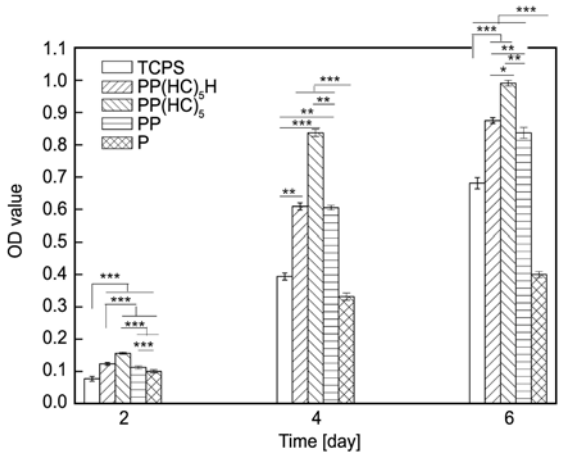

Figure 5. Cell viability (MTT assay) of osteoblasts cultured for 2, 4, 6 days respectively; results are the means±SD of three independent experiments, [n = 5, *P<0.05, **P<0.01, ***P<0.001]

Table 3. The viability of osteoblast cultured on different kinds of films for 3 and 5 days respectively [%]; results are the means±SD of three independent experiments

Samples	3 days	5 days
P	66.78±4.76	64.56±3.78
PP	76.47±5.41	71.80±4.10
$PP(HC)_5$	96.45±3.87	95.47±2.17
$PP(HC)_5H$	81.21±3.90	74.69±2.98

plied as the outermost layer. In particular, the cell proliferation ratios on the Col I terminated films were greatly improved, with values more than that of TCPS. The highest cell viability (shown in Table 2) also observedon the Col I terminated films. This could be attributed to the uniform Col I coating formation on the surface, a previous study found that Col I enhanced HOS proliferation [37]. Therefore the presence of native, fibrils structure of the Col I coating layer contributed significant to the improved cytocompatibility of the PLLA film.

3.5. Cell morphology

Scanning electron microscope (SEM, JSM26390LV) images after osteoblast cultured for 3 and 5 days were shown in Figure 7, some of the cells on the control PLLA (Figure 7d, 7h) film seemed to be shrinkage and detached from the substrate, and the cell number was also very small. On the other hand, the osteoblast on the $PP(HC)_5$ (Figure7a, 7e), PP (Figure 7c, 7g) and $PP(HC)_5H$ (Figure 7b, 7f) films displayed flatten shapes and a spreading morphology on the substrate, while the forming of confluent and aligned cell layers during the observation time only achieved on the Col I terminated films. In addition, on the Col I terminated films, SEM micrographs of the cells showed cell projections and extensions. Those cell extensions seemed to be in a regular way, which might be created by the contact guidance of the Col I fibrils. In contrast, cells on other groups showed a randomly extension.

A similar conclusion could be made after observation by CLSM (Figure 8). Figure 8 shows that most of the osteoblasts on the control PLLA film spread not so well and seemed to shrink. In the other three groups, cells maintained their typical morphology, while the cellular morphology was different in different groups. Numerous well defined actin filaments were observed in PEI modified and HA ended samples, and interestingly, actin filaments extended in irregular directions in both groups, while more dense, spreading and aligned osteoblasts existed on the PLLA films covered with Col I as the outermost layer (Figure 8a). The actin filament distribution was fully spread in $PP(HC)_5$ film (Figure 8a). Moreover, all of the actin filaments with regular directions in $PP(HC)_5$ film were well-defined and the actin microfilament system ran parallel to the long axis of the cells while it ran in irregular directions in the other groups (Figure 8b, 8c, 8d). This probably indicates weak cellular adhesion on other samples as compared to Col I ending ones. As well known, Col I is a structural protein present in the ECM and is extensively used to form scaffolds or films as promoter for cell adhesion, spreading and so on [36]. The natural structure of collagen fibers are proved to enhance cell attachment to synthetic surfaces [38] and it has been reported that fibroblasts align along oriented collagen fibril matrices via contact guidance [39, 40].

3.6. Alkaline phosphatase (ALP activity)

In accordance with expectations, the ALP level increased in all cultures. Cells cultured on the $PP(HC)_5$ films presented highest activity of ALP than the other three groups at 7^{th} and 14^{th} day which was shown in Figure 9. However there were no significant differences between PP and $PP(HC)_5$ H groups. While the activity of ALP on the control PLLA film was the lowest among all the samples. It demonstrated that after the modification of the PLLA, especially with the Col I terminated films, the present of ALP was obviously improved.

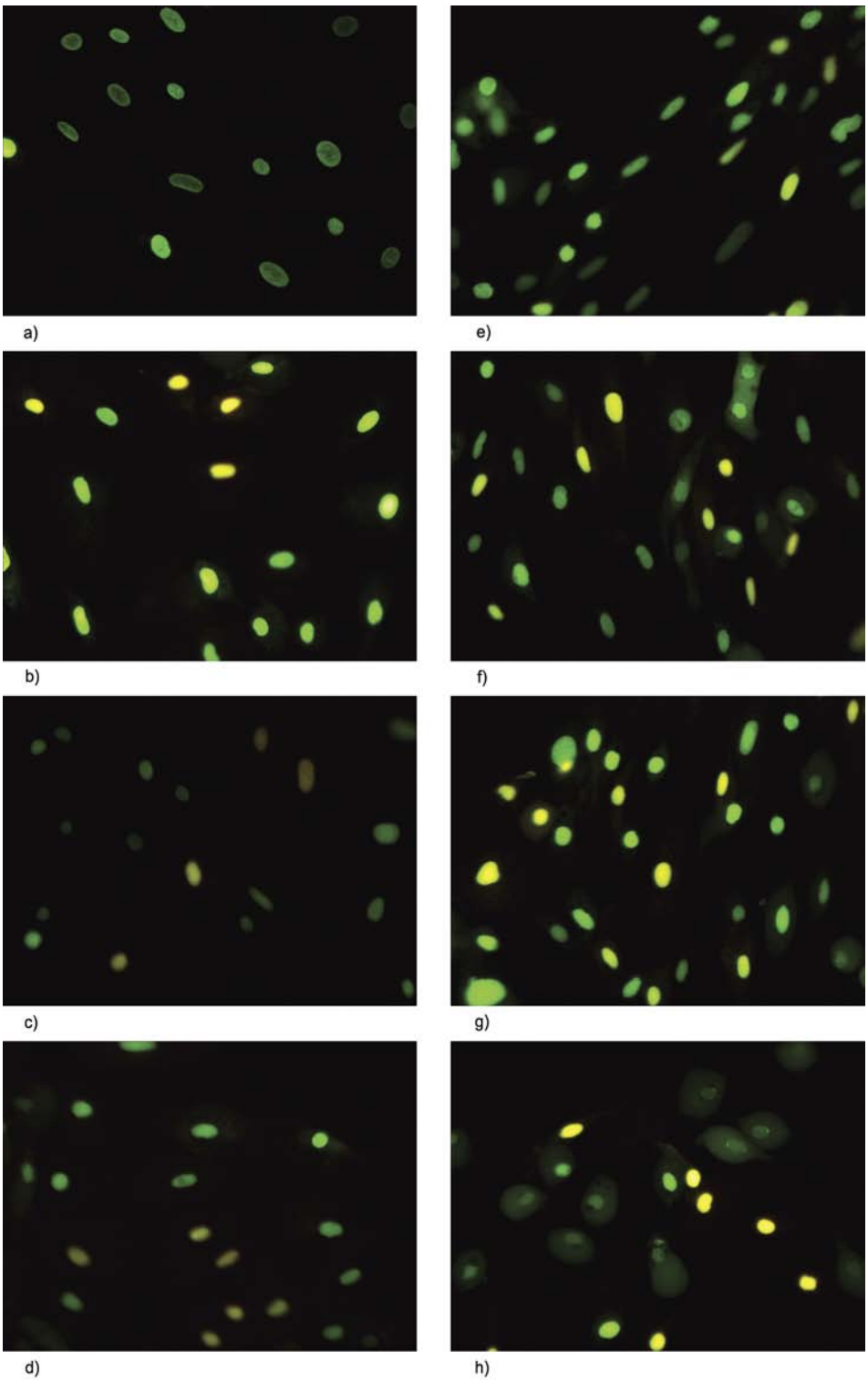

Figure 6. Calcein-AM/PI live/dead staining of osteoblast on $PP(HC)_5$ (a 3 days, e 5 days), $PP(HC)_5H$ (b 3 days, f 5 days), PP (c 3 days, g 5 days) and P (d 3 days, h 5 days) film respectively. Live cells stain green and dead cells stain red. (Original magnification ×200)

4. Conclusions

To improve the cell biocompatibility and cell affinity of PLLA films, the extracellular matrix components HA and Col I have been successfully deposited onto the PEI modified PLLA films using LBL assembly technique. The buildup of multilayer films exhibits a linear growth regime with the successive layer depositions, the Col I terminated samples leading to a uniform and relative aligned fibril network covering on the surface of the PLLA film. WCA

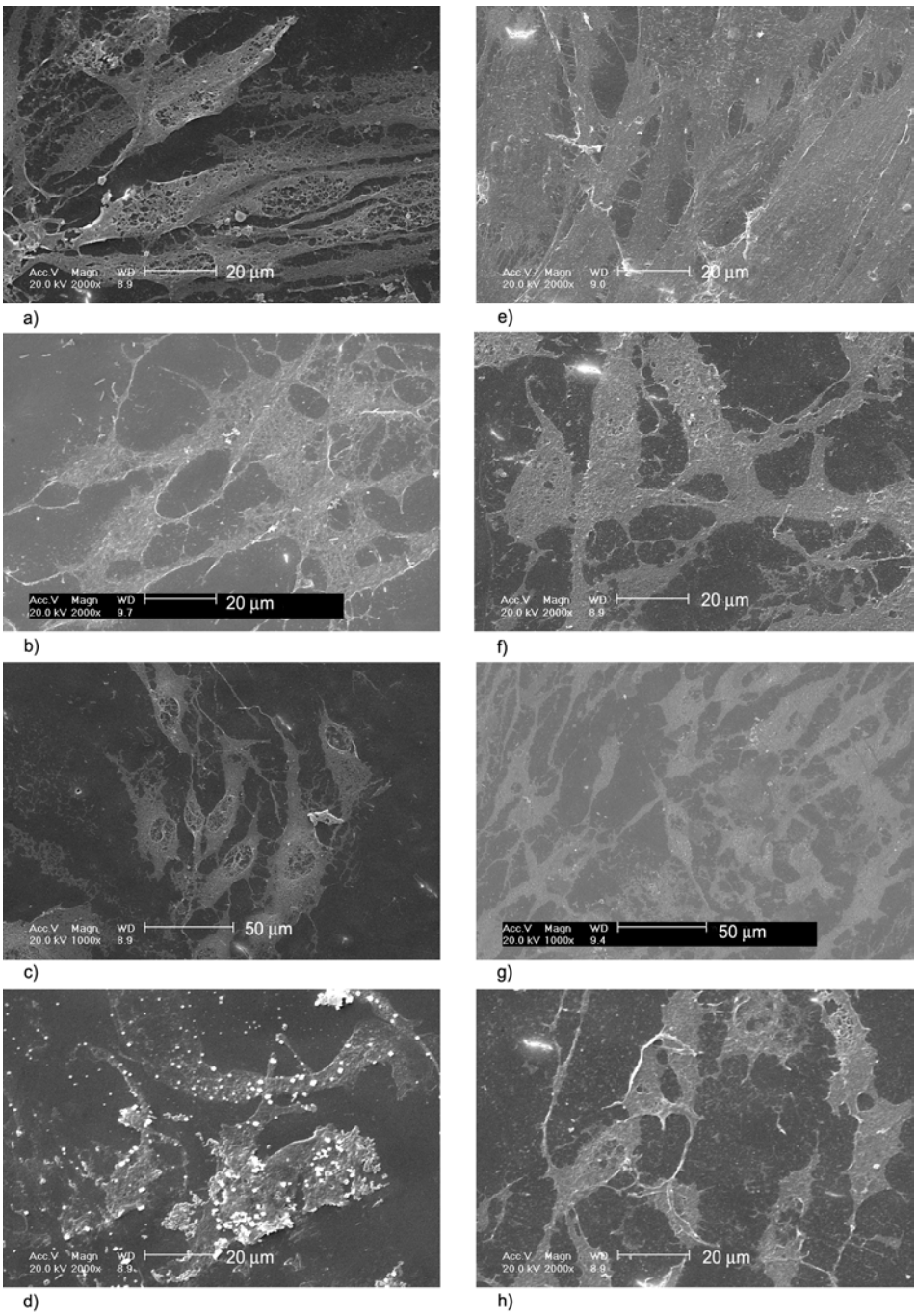

Figure 7. SEM image of osteoblast morphology on $PP(HC)_5$ (a, e); $PP(HC)_5H$ (b, f); 0L (c, g); PLLA (d, h) film for 3 and 5 days respectively

results showed that after the LBL modification, the hydrophilicity of the film was dramatically enhanced. Cell viability and proliferation were apparently improved after LBL modification of the PLLA film. Moreover, cells presented highest viability, proliferation and ALP expression on the Col I terminated films, and osteoblast extensions were found to be directed by contact guidance of the aligned Col I fibrils. This study further demonstrated that the coating of ECM on to the organic PLLA film surface dramatically improved its cell compatibility. Comparing with conventional coating methods, polyelectrolyte multilayer is easy to prepare using LBL technique. Therefore, it may be an ideal choice to construct ECM-based films or 3D scaffolds for tissue engineering. Moreover, these very flexible systems may allow broad applications for improve the bioactivity of polymeric materials.

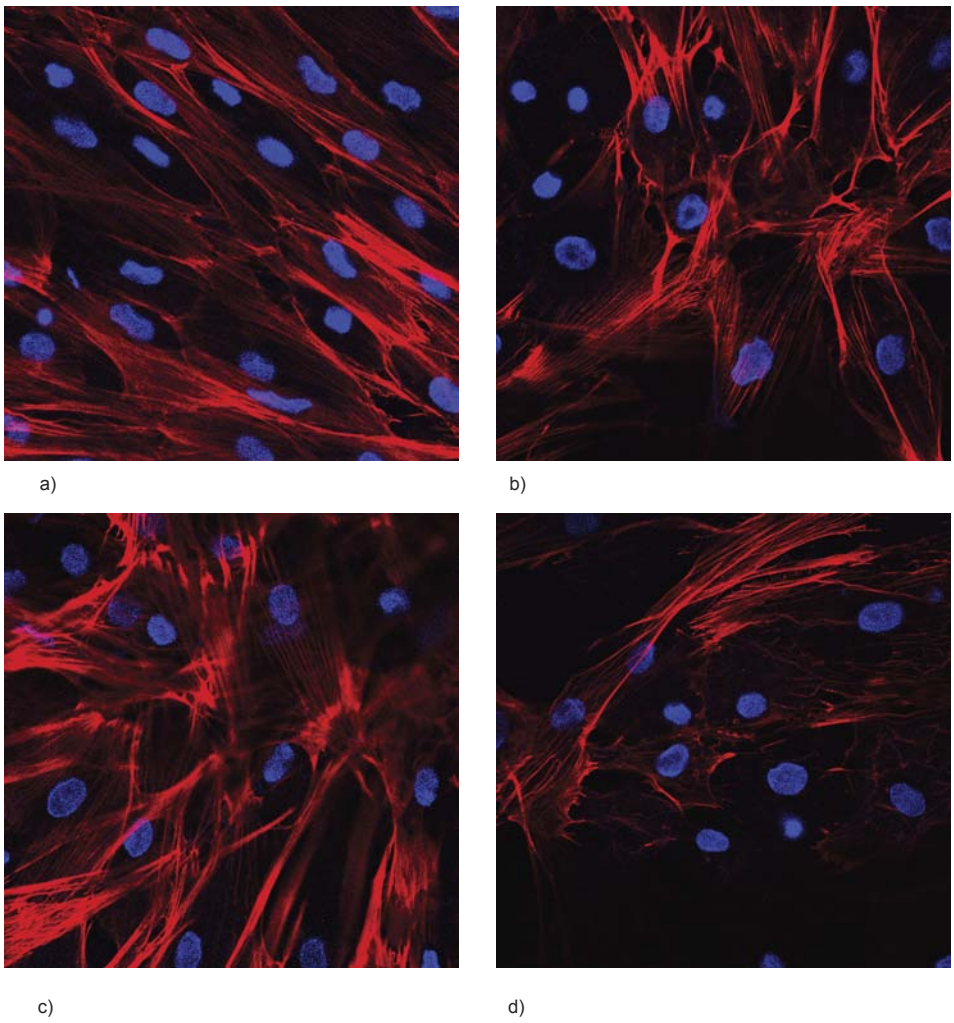

Figure 8. CLSM image of osteoblast cultured on $PP(HC)_5$ (a); $PP(HC)_5H$ (b); PP (c); P (d) films for 7 days. F-actin was stained in red, nucleuses was stained in blue. (Original magnification ×400)

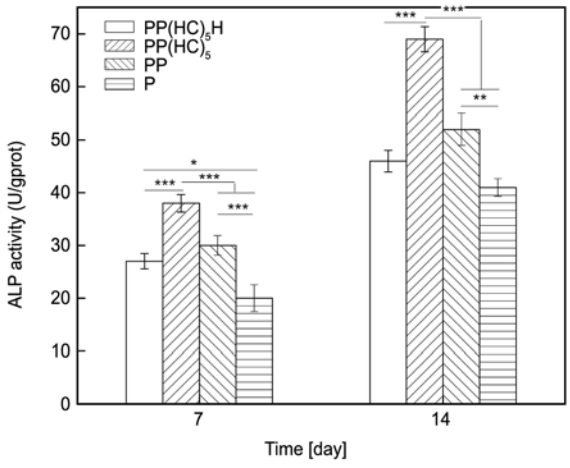

Figure 9. ALP activity of the osteoblast on different films after 7 and 14 days culturing; results are the means±SD of three independent experiments, [$n = 3$, *P<0.05, **P<0.01, ***P<0.001]

Acknowledgements

The work was supported by National Natural Science Foundation of China (81171459 and 31270021) and Guangzhou 'Zhujiang River' excellent young scientists program (2011J2200037).

References

[1] Griffith L. G., Naughton G.: Tissue engineering – Current challenges and expanding opportunities. Science, **295**, 1009–1014 (2002). DOI: 10.1126/science.1069210

[2] Vert M.: Polymeric biomaterials: Strategies of the past vs. strategies of the future. Progress in Polymer Science, **32**, 755–761 (2007). DOI: 10.1016/j.progpolymsci.2007.05.006

[3] Nishikawa T., Nishida J., Ookura R., Nishimura S-I., Wada S., Karino T., Shimomura S.: Honeycomb-patterned thin films of amphiphilic polymers as cell culture substrates. Materials Science and Engineering: C, **8–9**, 495–500 (1999). DOI: 10.1016/S0928-4931(99)00075-2

[4] Zhang Q., Mochalin V. N., Neitzel I., Hazeli K., Niu J., Kontsos A., Zhou J. G., Lelkes P. I., Gogotsi Y.: Mechanical properties and biomineralization of multifunctional nanodiamond-PLLA composites for bone tissue engineering. Biomaterials, **33**, 5067–5075 (2012). DOI: 10.1016/j.biomaterials.2012.03.063

[5] Mallick K. K., Winnett J.: Preparation and characterization of porous Bioglass® and PLLA scaffolds for tissue engineering applications. Journal of the American Ceramic Society, **95**, 2680–2686 (2012). DOI: 10.1111/j.1551-2916.2012.05071.x

[6] Chen J-P., Su C-H.: Surface modification of electrospun PLLA nanofibers by plasma treatment and cationized gelatin immobilization for cartilage tissue engineering. Acta Biomaterialia, **7**, 234–243 (2011). DOI: 10.1016/j.actbio.2010.08.015

[7] Garric X., Molès J. P., Garreau H., Guilhou J. J., Vert M.: Human skin cell cultures onto PLA_{50} (PDLLA) bioresorbable polymers: Influence of chemical and morphological surface modifications. Journal of Biomedical Materials Research Part A, **72**, 180–189 (2005). DOI: 10.1002/jbm.a.30216

[8] Jahno V. D., Ribeiro G. B. M., dos Santos L. A., Ligabue R., Einloft S., Ferreira M. R. W., Bombonato-Prado K. F.: Chemical synthesis and *in vitro* biocompatibility tests of poly (L-lactic acid). Journal of Biomedical Materials Research Part A, **83**, 209–215 (2007). DOI: 10.1002/jbm.a.31210

[9] Kim S-S., Park M. S., Jeon O., Choi C. Y., Kim B-S.: Poly(lactide-*co*-glycolide)/hydroxyapatite composite scaffolds for bone tissue engineering. Biomaterials, **27**, 1399–1409 (2006). DOI: 10.1016/j.biomaterials.2005.08.016

[10] Ravichandran R., Venugopal J. R., Sundarrajan S., Mukherjee S., Ramakrishna S.: Precipitation of nanohydroxyapatite on PLLA/PBLG/collagen nanofibrous structures for the differentiation of adipose derived stem cells to osteogenic lineage. Biomaterials, **33**, 846–855 (2012). DOI: 10.1016/j.biomaterials.2011.10.030

[11] Tzoneva R., Seifert B., Albrecht W., Richau K., Groth T., Lendlein A.: Hemocompatibility of poly(ether imide) membranes functionalized with carboxylic groups. Journal of Materials Science: Materials in Medicine, **19**, 3203–3210 (2008). DOI: 10.1007/s10856-008-3456-8

[12] Diao H., Si Y., Zhu A., Ji L., Shi H.: Surface modified nano-hydroxyapatite/poly(lactide acid) composite and its osteocyte compatibility. Materials Science and Engineering: C, **32**, 1796–1801 (2012). DOI: 10.1016/j.msec.2012.04.065

[13] Zhao M., Li L., Li X., Zhou C., Li B.: Three-dimensional honeycomb-patterned chitosan/poly(L-lactic acid) scaffolds with improved mechanical and cell compatibility. Journal of Biomedical Materials Research Part A, **98**, 434–441 (2011). DOI: 10.1002/jbm.a.33132

[14] Atthoff B., Hilborn J.: Protein adsorption onto polyester surfaces: Is there a need for surface activation? Journal of Biomedical Materials Research Part B: Applied Biomaterials, **80**, 121–130 (2007). DOI: 10.1002/jbm.b.30576

[15] Khorasani M. T., Mirzadeh H., Irani S.: Plasma surface modification of poly (L-lactic acid) and poly (lactic-*co*-glycolic acid) films for improvement of nerve cells adhesion. Radiation Physics and Chemistry, **77**, 280–287 (2008). DOI: 10.1016/j.radphyschem.2007.05.013

[16] Zhu H., Ji J., Shen J.: Surface engineering of poly(DL-lactic acid) by entrapment of biomacromolecules. Macromolecular Rapid Communications, **23**, 819–823 (2002). DOI: 10.1002/1521-3927(20021001)23:14<819::AID-MARC819>3.0.CO;2-9

[17] Kim B. Y., Bruening M. L.: pH-dependent growth and morphology of multilayer dendrimer/poly(acrylic acid) films. Langmuir, **19**, 94–99 (2003). DOI: 10.1021/la026353o

[18] Huang R., Li Y., Zhou X., Zhang Q., Jin H., Zhao J., Pan S., Deng H.: LBL fabricated biopolymer-layered silicate based nanofibrous mats and their cell compatibility studies. Carbohydrate Polymers, **90**, 957–966 (2012). DOI: 10.1016/j.carbpol.2012.06.026

[19] Hammond P. T.: Engineering materials layer-by-layer: Challenges and opportunities in multilayer assembly. AIChE Journal, **57**, 2928–2940 (2011). DOI: 10.1002/aic.12769

[20] Ni Y., Liu Z., Gao W., Qu S., Weng J., Feng B.: Characterization of self-assembled decyl bis phosphonate–collagen layers on titanium by QCM-D and osteoblast-compatibility. Applied Surface Science, **257**, 9287–9292 (2011). DOI: 10.1016/j.apsusc.2011.05.007

[21] Mhanna R. F., Vörös J., Zenobi-Wong M.: Layer-by-layer films made from extracellular matrix macromolecules on silicone substrates. Biomacromolecules, **12**, 609–616 (2011). DOI: 10.1021/bm1012772

[22] Mathews S., Bhonde R., Gupta P. K., Totey S.: Extracellular matrix protein mediated regulation of the osteoblast differentiation of bone marrow derived human mesenchymal stem cells. Differentiation, **84**, 185–192 (2012). DOI: 10.1016/j.diff.2012.05.001

[23] Datta N., Holtorf H. L., Sikavitsas V. I., Jansen J. A., Mikos A. G.: Effect of bone extracellular matrix synthesized *in vitro* on the osteoblastic differentiation of marrow stromal cells. Biomaterials, **26**, 971–977 (2005). DOI: 10.1016/j.biomaterials.2004.04.001

[24] Yu H-S., Jin G-Z., Won J-E., Wall I., Kim H-W.: Macrochanneled bioactive ceramic scaffolds in combination with collagen hydrogel: A new tool for bone tissue engineering. Journal of Biomedical Materials Research Part A, **100**, 2431–2440 (2012). DOI: 10.1002/jbm.a.34163

[25] Hoyer B., Bernhardt A., Heinemann S., Stachel I., Meyer M, Gelinsky M.: Biomimetically mineralized salmon collagen scaffolds for application in bone tissue engineering. Biomacromolecules, **13**, 1059–1066 (2012). DOI: 10.1021/bm201776r

[26] Zhang J., Senger B., Vautier D., Picart C., Schaaf P., Voegel J-C., Lavalle P.: Natural polyelectrolyte films based on layer-by layer deposition of collagen and hyaluronic acid. Biomaterials, **26**, 3353–3361 (2005). DOI: 10.1016/j.biomaterials.2004.08.019

[27] Khademhosseini A., Suh K. Y., Yang J. M., Eng G., Yeh J., Levenberg S., Langer R.: Layer-by-layer deposition of hyaluronic acid and poly-L-lysine for patterned cell co-cultures. Biomaterials, **26**, 3583–3592 (2004). DOI: 10.1016/j.biomaterials.2003.10.033

[28] Deyl Z., Rohlicek V., Adam M.: Separation of collagens by capillary zone electrophoresis. Journal of Chromatography A, **480**, 371–378 (1989). DOI: 10.1016/S0021-9673(01)84306-5

[29] Liu Z-M., Lee S-Y., Sarun S., Moeller S., Schnabelrauch M., Groth T.: Biocompatibility of poly(L-lactide) films modified with poly(ethylene imine) and polyelectrolyte multilayers. Journal of Biomaterials Science, Polymer Edition, **21**, 893–912 (2010). DOI: 10.1163/156856209X450748

[30] Jiang F., Hörber H., Howard J., Müller D. J.: Assembly of collagen into microribbons: Effects of pH and electrolytes. Journal of Structural Biology, **148**, 268–278 (2004). DOI: 10.1016/j.jsb.2004.07.001

[31] Schasfoort R. B. M., Tudos A. J.: Handbook of surface plasmon resonance. RSC Publishing. Cambridge (2008).

[32] Whitson K. B., Lukan A. M., Marlowe R. L., Lee S. A., Anthony L., Rupprecht A.: Binding of the water of primary hydration to the sodium and cesium salts of deoxyribonucleic acid and potassium hyaluronate. Physical Review E, **58**, 2370–2377 (1998). DOI: 10.1103/PhysRevE.58.2370

[33] Taraballi F., Zanini S., Lupo C., Panseri S., Cunha C., Riccardi C., Marcacci M., Campione M., Cipolla L.: Amino and carboxyl plasma functionalization of collagen films for tissue engineering applications. Journal of Colloid and Interface Science, **394**, 590–597 (2013). DOI: 10.1016/j.jcis.2012.11.041

[34] Köwitsch A., Yang Y., Ma N., Kuntsche J., Mäder K., Groth T.: Bioactivity of immobilized hyaluronic acid derivatives regarding protein adsorption and cell adhesion. Biotechnology and Applied Biochemistry, **58**, 376–389 (2011). DOI: 10.1002/bab.41

[35] Rezwan K., Chen Q. Z., Blaker J. J., Boccaccini A. R.: Biodegradable and bioactive porous polymer/inorganic composite scaffolds for bone tissue engineering. Biomaterials, **27**, 3413–3431 (2006). DOI: 10.1016/j.biomaterials.2006.01.039

[36] Lee C. H., Singla A., Lee Y.: Biomedical applications of collagen. International Journal of Pharmaceutics, **221**, 1–22 (2001). DOI: 10.1016/S0378-5173(01)00691-3

[37] Wang R. C-C., Hsieh M-C., Yang S-P., Chuang P-K., Lin J-C.,Yang C-Y., Lee T-M.: Characteristics and cyto-compatibility of collagen/Ca–P coatings on Ti_6Al_4V substrate. Surface and Coatings Technology, **205**, 4683–4689 (2011). DOI: 10.1016/j.surfcoat.2011.04.029

[38] Sinani V. A., Koktysh D. S., Yun B-G., Matts R. L., Pappas T. C., Motamedi M., Thomas S. N., Kotov N. A.: Collagen coating promotes biocompatibility of semiconductor nanoparticles in stratified LBL films. Nano Letters, **3**, 1177–1182 (2003). DOI: 10.1021/nl0255045

[39] Elsdale T. R.: Parallel orientation of fibroblasts *in vitro*. Experimental Cell Research, **51**, 439–450 (1968). DOI: 10.1016/0014-4827(68)90134-1

[40] Guido S., Tranquillo R. T.: A methodology for the systematic and quantitative study of cell contact guidance in oriented collagen gels. Correlation of fibroblast orientation and gel birefringence. Journal of Cell Science, **105**, 317–331 (1993).

eXPRESS Polymer Letters Vol.8, No.5 (2014) 336–344
Available online at www.expresspolymlett.com
DOI: 10.3144/expresspolymlett.2014.37

Tailoring the toughness and CTE of high temperature bisphenol E cyanate ester (BECy) resin

M. Thunga[1,2], *M. Akinc*[1,2], *M. R. Kessler*[1,2,3*]

[1]Department of Materials Science and Engineering, Iowa State University, Ames, IA, USA
[2]Ames Laboratory, US Dept. of Energy, Ames, IA, USA
[3]School of Mechanical and Materials Engineering, Washington State University, Pullman, WA, USA

Received 21 August 2013; accepted in revised form 26 December 2013

Abstract. The objective of the present work is to enhancing the toughness and minimizing the CTE of a special class of bisphenol E cyanate ester (BECy) resin by blending it with a thermoplastic toughening agent. Poly(ether sulfone) was chosen as a high temperature resistant thermoplastic resin to enhance the thermo-mechanical properties of BECy. The influence of poly(ether sulfone)/BECy blend composition on the morphology and phase behavior was studied using scanning electron microscopy and dynamic mechanical analysis. The mechanical properties of the blends were evaluated by flexural tests, which demonstrated significant enhancement in the material's toughness with an increase in PES concentration from 0 to 15 wt%. The coefficient of thermal expansion of pure BECy was reduced from 61 to 48 ppm/°C in the blends with PES, emphasizing the multi-functional benefits of PES as a toughening agent in BECy.

Keywords: *thermosetting resins, bisphenol E cyanate ester, polymer matrix composites, injection repair, polymer blends and alloys*

1. Introduction

The growing demand for strong and lightweight materials from polymer matrix composites (PMCs) has driven recent interest in engineering their functional properties. Under extreme service conditions, the toughness and the coefficient of thermal expansion (CTE) of the polymer matrix play an important role in controlling the durability of composite materials. Polycyanurates are used extensively to manufacture structural composites because of their excellent mechanical, thermal, and adhesive properties. Cyanate ester monomers with two or more cyanate ester (–O–C≡N) functional groups undergo a thermally initiated cyclotrimerization reaction to form densely packed cross-linked thermosets [1, 2]. Because of their high crosslinking density they exhibit high glass transition temperatures, moderate fracture toughness after cure, low toxicity, and long-term stability [3]. The properties of dicyanate ester resins meet several service requirements for applications in extreme environments. Polycyanurates are also widely used in electronic circuit boards because of their low dielectric constant [4]. Another major advantage of cyanate ester resins is the ease of processability compared to typical thermoset resins used to manufacture polymer matric composites (PMCs). The low room temperature viscosity and good compatibility with the reinforcing fibers phase makes them matrix resin of choice for PMCs.

Bisphenol E cyanate ester (BECy) is considered a unique polycyanurate resin for composite applications because of its distinctive combination of high T_g and low viscosity at room temperature [5, 6]. BECy's low viscosity, caused by the rotational flexibility of the BECy monomer structure (Figure 1), makes it easy to process at low temperatures [1].

*Corresponding author, e-mail: MichaelR.Kessler@wsu.edu

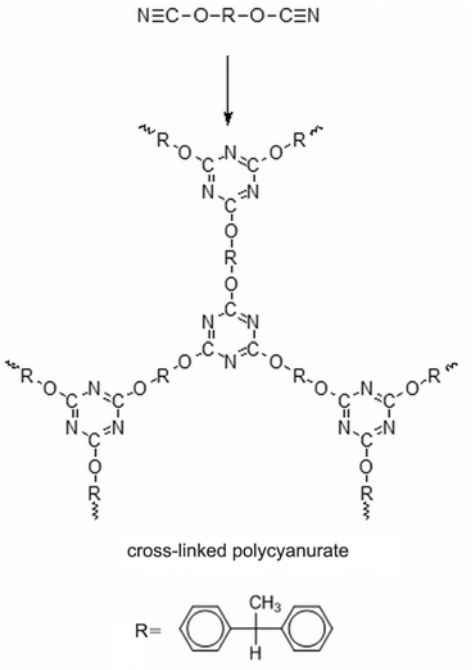

Figure 1. BECy monomer transforming into a cross-linked networked structure (cured)

Good fiber wetting together with a glass transition temperature of 270°C when fully cured qualifies BECy for high service temperature applications. In our previous work, it was demonstrated that BECy outperformed a bisphenol A-based bifunctional epoxy in all mechanical tests, even at high temperatures (200°C) [7]. Bisphenol E cyanate ester resin was also identified as a unique adhesive for injection repair of damages in high temperature polymer matrix composites [8]. However, the inherent brittle behavior of BECy is a major disadvantage in functional applications. In addition, when BECy is used as the matrix resin in carbon fiber reinforced polymer composites, the high CTE of BECy (~60 ppm/°C) when compared to nearly negligible CTE of carbon fiber, results in a significant mismatch in the thermal expansivities of BECy and the reinforcing fiber phase. This mismatch in CTE results in residual stress in the composites leading to loss in dimensional stability of the produced parts.

While the current efforts to develop new thermoset resins with advanced thermal and mechanical properties were based on new synthesis routes [9, 10], blending of polymers offers a simple and easy alternative over complex synthesis techniques. Multiphase polymer blends prepared to create or improve desired functional properties in thermoset polymers are considered potential alternatives in the literature [11–14]. In the present work, poly(ether sulfone) (PES) was used as a high temperature resistant thermoplastic toughening agent for BECy. The molecular structure of PES is shown in Figure 2. PES is a well-known engineering thermoplastic with good mechanical and thermal stability at elevated temperatures [15]. Typical applications of PES include high temperature coating formulations, advanced high temperature composites, and specialty adhesives. In a recent work, Grishchuk *et al*. [16] have investigated the influence of blending PES in a tetrafunctional, anhydride hardened epoxy resin. The phase behavior and fracture mechanical of these thermoplastic-thermoset blends have been studied. Blending of this high performance engineering thermoplastic with BECy could reduce the brittleness of BECy without sacrificing its modulus and glass transition temperature (T_g). In addition to the improvement in toughness, the low CTE of PES compared to BECy is expected to reduce the CTE of BECy.

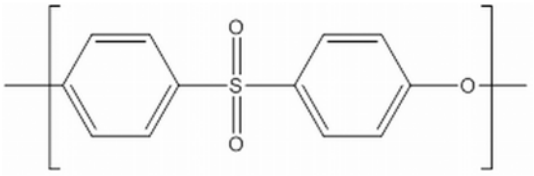

Figure 2. Molecular structure of poly(ether sulfone)

The objective of the work presented here was to study the toughening mechanism of BECy/PES blends for high temperature service applications. The phase behavior of BECy and PES blends was investigated qualitatively using SEM and thermo-mechanical techniques. Further, the CTE of BECy is engineered by blending with PES.

2. Experimental

2.1. Materials

Bisphenol E cyanate ester (BECy) was purchased from Tencate Technologies, Almelo, The Netherlands. Poly(ether sulfone) (RADEL A-304P) was kindly supplied by Solvay Advanced Polymers, Alpharetta, GA, USA. A melt mixing technique was used to blend BECy and PES following a procedure described earlier [14]. During the melt mixing procedure, pure BECy was initially heated to 160°C in a round bottom flask followed by blending PES in different blend concentrations of 5, 10, 15, 20 and 30 wt% in BECy. Using a mechanical stirrer, both blend components were continuously stirred until a clear, transparent solution was observed. A liquid

phase organometallic-based catalyst (EX-1510-B, Tencate Technologies, Almelo, The Netherlands) was added as a curing agent to cure the clear solutions (3 ppm). A standard curing schedule consisting of a pre-cure at 180°C for 2 h followed by a post-cure at 250°C for 2 h was used for all the samples.

2.2. Thermal analysis

The influence of blend composition on the phase behavior was studied by dynamic mechanical analysis (DMA). The temperature dependent dynamic mechanical properties were characterized by using a DMA Q-800 from TA Instruments, New Castle, DE, USA. DMA tests were conducted on 12×6×0.5 mm samples in tensile mode geometry between 30 to 320°C. A heating rate of 3°C/min, frequency of 1 Hz and a strain amplitude of 0.05% was used for the tests. The thermal stability of the neat polymers and their blends were determined by thermogravimetric analysis (TGA) using a TGA-Q50 from TA Instruments. TGA results were obtained in air for a temperature range from room temperature (*RT*) to 700°C at a heating rate of 20°C/min. The CTE of the samples was measured using a Q-400 thermo mechanical analyzer (TMA) from TA Instruments. The thermomechanical properties of the composites were characterized using the second heating scan of a heat/cool/heat cycle performed at 5°C/min from 25 to 320°C.

2.3. Mechanical properties

Specimens for flexural tests were machined from a 60×40×20 mm bulk sample using a slow-speed diamond edge saw. Flexural specimens with dimensions of 50×30×1 mm were tested in three-point bending mode with a span length of 30 mm. The flexural tests were performed using an Instron universal testing machine (model 4502), Norwood, MA, USA with a crosshead speed of 1 mm/min.

2.4. Morphology

The fracture surfaces of the flexural specimens were examined by scanning electron microscopy (SEM) using a Hitachi S-2460N, Japan. The SEM images were collected using backscattered electron signals from a working distance of 25 mm. Fracture morphology images of the blends were correlated with the mechanical properties of the samples.

3. Results and discussion

3.1. Morphology of BECy/PES blends

The phase morphologies of BECy/PES blends prepared by melt mixing were investigated by SEM analysis. During the sample preparation process, pre-cured BECy and PES blends were completely miscible, forming a clear solution. However, after curing, the samples appeared to lose their transparency. The change in the transparency of BECy/PES blends after curing was attributed to cure-induced phase separation in the blends. Figure 3 depicts the morphologies of the fracture surfaces of the investigated samples. The dark and light areas correspond to BECy and PES phases, respectively. Pure BECy samples exhibited a smooth fracture surface with traces of shear bands in the SEM micrographs, whereas BECy/PES blends showed microphase separation in all blend compositions. A systematic change in the microstructure was observed with an increase in PES concentration in the blends. Similar morphologies were observed previously in thermoset/thermoplastic blends tailored to improve the toughness of the materials [11, 14]. The PES minor phase initially appeared to form finely dispersed, spherical nano-domains inside the continuous BECy phase. With an increase in PES concentration from 5 to 15 wt%, the size and number of these PES micro domains increased along with a simultaneous decrease of the BECy phase. At 20 wt% PES, the BECy phase underwent a morphological transformation from a continuous to a discontinuous structure, revealing composition-dependent phase inversion.

The SEM micrographs of blends with high PES concentrations (blends containing 30 wt% of PES) exhibited large BECy micro domains distributed inside the separated BECY/PES microphase structure. Due to large discrepancy in the phase separation, a low magnification SEM micrograph is used in Figure 3f, to present a representative local morphology of 30 wt% PES sample. In general, such morphologies are identified as non-uniform phase separated morphologies. The observed inhomogeneity in the microstructure of blends with high PES concentration was primarily driven by the viscosity of the un-cured resin. Uniform distribution of the binary phases in 30 wt% PES sample may be hindered due to the high viscosity of the melt . To overcome this problem, various research groups previ-

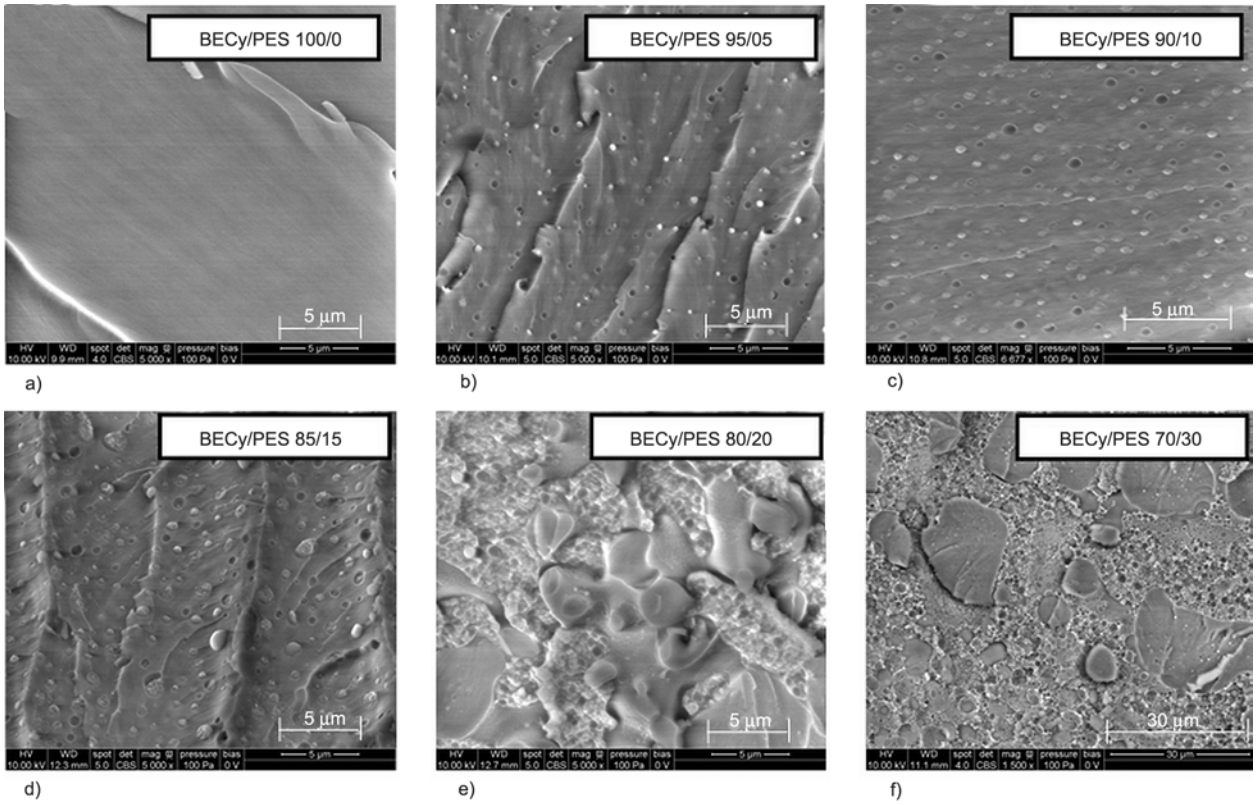

Figure 3. SEM micrographs of BECy/PES blends containing: a) 0, b) 5, c) 10, d) 15, e) 20, and f) 30 wt% PES

ously used solution casting techniques as an approach to achieve an equilibrium microstructure in blends, even at high PES concentrations [12, 17].

3.2. Dynamic mechanical analysis

The dynamic mechanical properties of BECy/PES blends were studied to understand the effect of phase separation on their temperature-dependent mechanical properties. The loss modulus (E'') and storage modulus (E') curves of BECy/PES blends are shown in Figure 4.

The influence of blend composition on the T_g behavior of the PES-rich phase was determined from the loss modulus (E'') curves. Figure 4a shows a decrease in T_g peak intensity with an increase in PES concentration. At low PES concentrations (0 to 15 wt%), as BECy formed a continuous phase with finely dispersed PES micro domains, the physical interactions between PES and the surrounding BECy phase hindered the segmental relaxation in the PES phase, resulting in reduced relaxation peak intensity in the blends [18].

The loss modulus curve of pure BECy exhibited a single peak at 270°C, indicating the glass transition (T_g) temperature of BECy. Blending PES with BECy resulted in a decrease in T_g compared to BECy, together with a simultaneous reduction in peak intensity. The E'' curve showed a secondary peak at a lower temperature corresponding to the T_g of PES. With an increase in weight percent of PES in the blends, the secondary peak intensity gradually increased, approaching the T_g of the PES-rich phase near 240°C. The presence of two distinct T_g's verified phase separation of the blends. The composition-dependent changes in glass transition temperatures of the BECy and PES phases are listed in Table 1. Generally, immiscible polymer blends show multiple glass transition peaks, whereas miscible blends show a single transition peak in the E'' curve [19, 20]. However, for partially miscible blends, the T_g peak becomes broader and the peak positions shift to either higher or lower temperatures [21, 22]. With the T_g of the PES (240°C) below the T_g of the BECy (270°C), a reduction in T_g for the BECy-rich phase with an increase in PES composition in the blends was expected. With an increase in PES concentration from 0 to 15 wt%, the T_g of the BECy-rich phase was reduced from 270 to 258.

As the peak position of T_g is primarily controlled by the mobility of the polymer chain segments, the presence of PES chains inside the cross-linked network of BECy may increase the segmental mobility, resulting in a shift of the T_g of BECy-rich phase to lower temperatures. Another potential reason for the

observed shift in the T_g behavior of the BECy-rich phase is the crosslinking density. Blending PES with BECy monomer may have adversely affected on the cure behavior of BECy, resulting in a lower crosslinking density. The degree of cure in BECy may be significantly affected by the functional groups on the blend component [23]. As glass transition temperature in thermoset polymers is directly proportional to the crosslinking density, the observed change in the glass transition temperature of the BECy-rich phase can be directly related to its inherent crosslinking density.

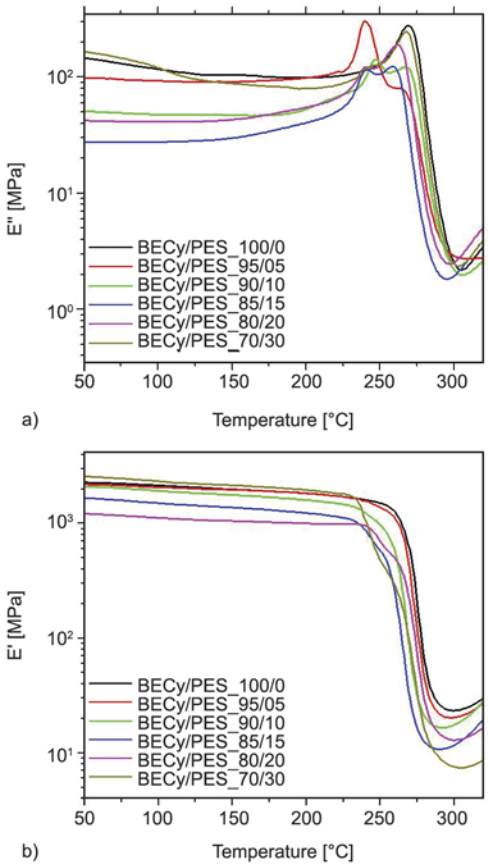

Figure 4. Influence of blend composition on the dynamic mechanical properties; a) temperature-dependent loss modulus (E'') curves of BECy/PES blends with different blend compositions; b) temperature-dependent storage modules (E') of blends

The dynamic mechanical storage modulus (E') is used as another valuable tool to describe the influence of blend composition on the stiffness of a material over a broad temperature range. The changes in the storage modulus with PES concentration in the blends is shown in Figure 4b. The E' curves of pure BECy and BECy/PES blends showed an extended glassy plateau until the temperature reached the glass transition temperature of the inherent phases. The modulus of the material measured at 50°C within the glassy regime is listed in Table 1. With an increase in PES concentration from 0 to 10 wt%, a slight reduction in glassy modulus from 2.27 to 2.10 GPa was observed for the blends. Further increase in PES content above 10 wt% resulted in a significant reduction in modulus from 2.10 to 1.12 GPa. The composition-dependent change in the modulus of the blends was attributed to the phase separated microstructure. At low PES concentrations, as the BECy phase formed a continuous phase, the mechanical properties were primarily dominated by the properties of BECy. However, at high PES concentrations, the transition in the morphology of the blends from a continuous to a discontinuous BECy phase resulted decrease in the storage modulus of the blends, as the modulus of PES is lower than that of BECy.

3.3. Influence of PES concentration on flexural properties of BECy/PES blends

In order to further investigate the influence of PES concentration on the mechanical properties of BECy/PES blends, flexural properties were evaluated using three-point bending tests. Flexural stress and ultimate strain to break are shown in Figure 5a and 5b, respectively. The toughness of the samples was determined by the area under the corresponding flexural stress-strain curves in Figure 5c. With an increase in PES concentration, the flexural mechanical properties (flexural stress, ultimate strain, and toughness)

Table 1. Influence of blend composition on storage modules (E') and glass transition temperature of BECy and PES phases

Samples	Storage modulus, E′ at 50°C [MPa]	Glass transition temperature, T_g [°C]	
		BECy-rich phase	PES-rich phase
BECy	2.27	270	NA
BECy/PES 95/05	2.19	267	243
BECy/PES 90/10	2.10	261	240
BECy/PES 85/15	1.67	258	240
BECy/PES 80/20	1.22	267	247
BECy/PES 70/30	2.57	265	240

increased initially, followed by a significant drop at high PES concentrations (above 15 wt%). In general, the mechanical properties of phase separated polymer blends primarily depend on the interfacial adhesion between the binary phases. Strong interactions between the binary phases provide a synergetic effect and maintain the best bulk material properties from both blend components. In addition to these physical interactions, the crosslinking density of the BECy phase may further influence the mechanical properties. Park *et al*. [24] observed a composition dependent decrease in crosslinking density of epoxy resins after blending with PES. In a more recent work, we reported that the crosslinking density of pure BECy has a significant influence on the mechanical properties [25].

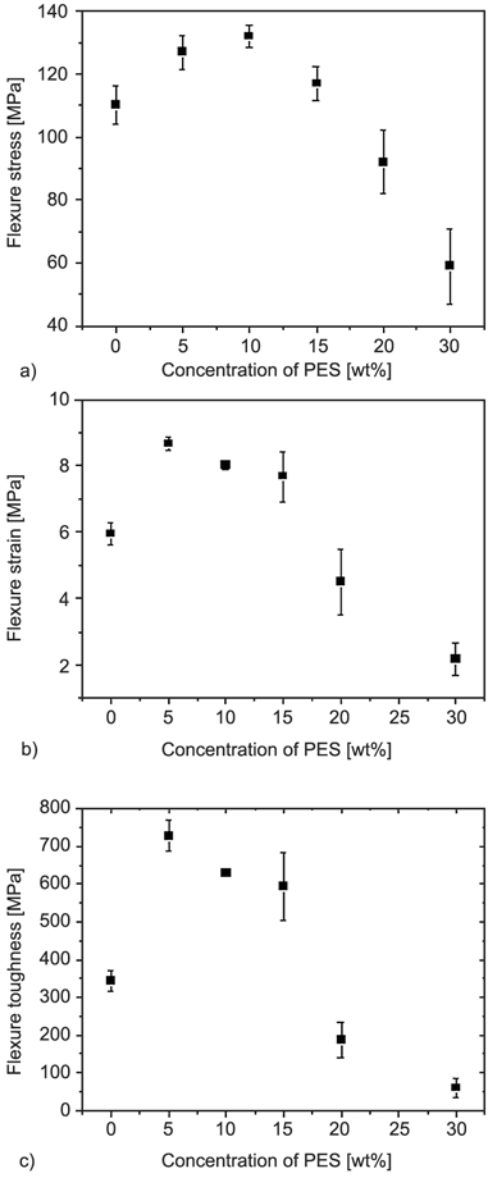

Figure 5. Influence of blend composition on the flexural properties: change in a) flexural stress; b) flexural strain; c) flexural toughness

In the present work, the pronounced enhancement in mechanical properties of blends of BECy with 0 to 10 wt% PES was attributed to the strong interfacial adhesion between the binary phases and the optimum crosslinking density of the BECy phase in the blends. However, in the intermediate PES concentration range (5 to 15 wt%), the observed nominal decrease in mechanical properties was caused by the decrease in crosslinking density of the BECy phase. At higher PES concentrations (20–30 wt%), the significant decrease in mechanical properties was attributed to the transition of the blends from a continuous to a discontinuous BECy phase, as observed in the SEM micrographs. Therefore, in BECy/PES blends, the transition in phase morphology and the change in crosslinking density of the BECy phase were determined to be the root causes for the observed change in mechanical properties of the blends.

3.4. Influence of PES concentration on the thermal stability of the blends

Cyanate ester resins are well recognized as excellent high temperature resistant materials [26]. Blending cyanate esters with thermoplastic polymers may significantly reduce their ultimate thermal stability because most thermoplastic polymers are less stable at elevated temperatures. However, PES is classified under polysulfones which are known to be thermoplastic polymers with high thermal stability. Therefore, PES was selected as a potential candidate to enhance the physical and mechanical properties of BECy without sacrificing its thermal stability. The thermal stability of BECy, PES, and their blends were investigated using thermogravimetric analysis (TGA) and the corresponding TGA and derivative TGA traces are shown in Figure 6a and 6b, respectively. Table 2 shows the temperature at which 5% weight loss measured from the TGA curve and the maximum degradation temperatures (T_{max}) determined by the peak position of the derivative TGA curve. The TGA curves reveal that both BECy and PES decompose in two steps, with major mass loss at 436°C for BECy and 524°C for PES. Figure 6a and Table 2 show that pure PES exhibits higher thermal stability than BECy. However, blending of PES with BECy did not improve the thermal stability, neither in the initial (5 % weight loss) nor in the maximum

Table 2. TGA analysis of BECy, PES, and their blends

Samples	5 % weight loss temperature [°C]	Stage 1: T_{max} from derivative TGA peak	Stage 2: T_{max} from derivative TGA peak
BECy	412	436	516
BECy/PES 85/15	417	437	516
BECy/PES 70/30	390	438	514
PES	482	524	612

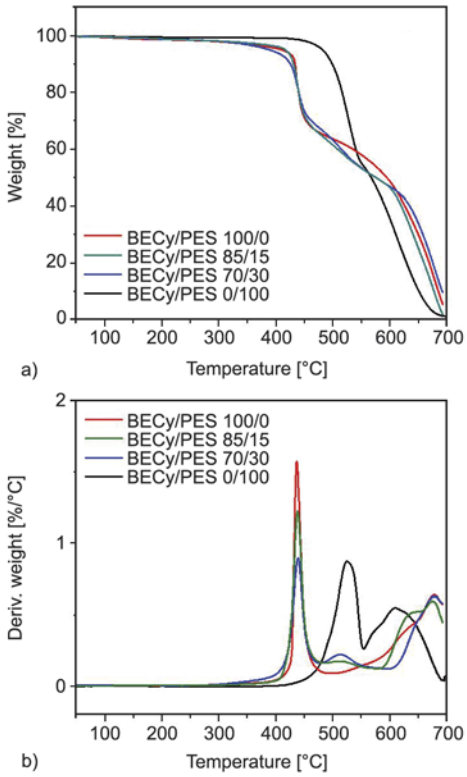

Figure 6. Thermogravimetric analysis (TGA) of pure BECy, PES, and their blends (BECy/PES 85/15, BECy/PES 70/30); a) TGA curves of BECy/PES blends illustrating the onset of thermal degradation; b) DTG curves of BECy/PES blends showing the shift in T_{max} with blend composition

(T_{max}) decomposition stages. In fact, a slight decrease in the initial decomposition temperature in the BECy/PES 70/30 blend was observed when compared to pure BECy. In thermoset polymers the crosslinking density plays a significant role in controlling their thermal stability; therefore, the slight drop in the initial decomposition temperature in the blends may be associated with the decrease in crosslinking density.

3.5. Influence of PES on the CTE of blends with BECy

Cyclic, high temperature thermo-mechanical loading of polymer matrix composites results in residual stresses in the composites caused by the mismatch in CTE between polymer matrix and reinforcing phase [27]. Therefore, low CTE polymer resins are preferred for high temperature resistant polymer matrix composite materials. In general, the residual thermal stresses in composites negatively influence dimensional stability, resulting in decreasing structural strength of the composites. As PES exhibits a considerably lower CTE (~25 ppm/°C) than BECy (~60 ppm/°C) at room temperature, blending PES with BECy reduced the CTE of BECy-rich phase along while improving the toughness of the composites. The CTE values determined from the slopes of the thermal strain curves, both in the glassy and rubbery range, are plotted in Figure 7. In the glassy region, the CTE ranged between 100 and 150°C, and in rubbery region, it ranged between 250 and 300°C. The glassy CTE of BECy decreased from 61 to 48 ppm/°C with PES concentration increasing from 0 to 30 wt%, while the rubbery CTE increased from 209 to 229 ppm/°C. The rubbery CTE values were much higher than glassy CTE because of the high segmental motion of the polymer chains above T_g. In this temperature range, most thermoplastic polymers show terminal relaxation with liquid-like flow behavior, whereas in thermosets the segmental mobility is constrained by the cross-linked network. Therefore, the observed difference in CTE between BECy and BECy/PES in the rubbery region is primarily caused by the onset of terminal relaxation in the PES phase.

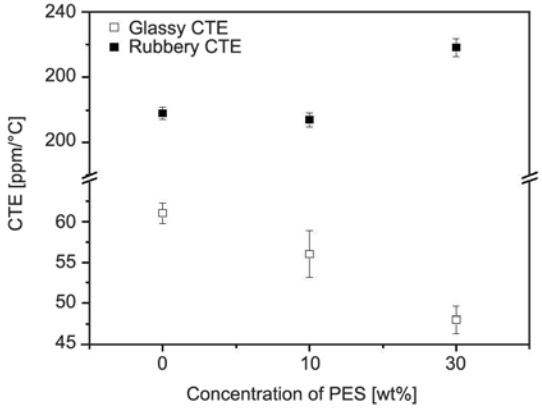

Figure 7. Influence of BECy/PES blend composition on the coefficient of thermal expansion (CTE) in the glassy and rubbery regions

4. Conclusions

The present work successfully explored the possibility of incorporation of poly(ether sulfone) (PES) into bisphenol E cyanate ester (BECy) resin by a simple blending process. The microphase separation in the blends observed by SEM images revealed both BECy and PES are forming miscible blends at all concentrations. DMA and TGA tests showed that the toughness of BECy resin increased considerably without significantly sacrificing the glass transition temperature after blending with PES. BECy/PES blends exhibited a reduction in CTE with increasing PES concentration, indicating that this blending strategy may be a simple alternative to the development of new polymer resins for the production of dimensionally stable, high temperature resistant composite materials.

References

[1] Hamerton I.: Chemistry and technology of cyanate ester resins. Chapman and Hall, London (1994).

[2] Grigat E., Pütter R.: Synthesis and reactions of cyanic esters. Angewandte Chemie International Edition in English, **6**, 206–218 (1967).
DOI: 10.1002/anie.196702061

[3] Russell A. J., Bowers C. P.: Resin requirements for successful repair of delaminations. in 'Proceedings of the 36th international SAMPE symposium, San Diego, California' 2279–2290 (1991).

[4] Kubens R., Schultheis H., Wolf R., Grigat E.: Aromatische Cyansaureester als Grundstoff für neue Harze in der Laminiertechnik. Kunststoffe, **58**, 827–832 (1968).

[5] Shimp D. A., Craig Jr. W. M.: New liquid dicyanate monomer for rapid impregnation of reinforcing fibers. in 'Proceedings of the 34th international SAMPE symposium, Reno, USA', 1336–1346 (1989).

[6] Sheng X., Akinc M., Kessler M. R.: Rheology and dynamic mechanical analysis of bisphenol E cyanate ester/alumina nanocomposites. Polymer Engineering and Science, **50**, 302–311 (2010).
DOI: 10.1002/pen.21543

[7] Thunga M., Lio W. Y., Akinc M., Kessler M. R.: Adhesive repair of bismaleimide/carbon fiber composites with bisphenol E cyanate ester. Composites Science and Technology, **71**, 239–245 (2011).
DOI: 10.1016/j.compscitech.2010.11.021

[8] Thunga M., Larson K., Lio W. Y., Weerasekera T., Akinc M., Kessler M. R.: Low viscosity cyanate ester resin for the injection repair of hole-edge delaminations in bismaleimide/carbon fiber composites. Composites Part A: Applied Science and Manufacturing, **52**, 31–37 (2013).
DOI: 10.1016/j.compositesa.2013.05.001

[9] Srinivasan S. A., McGrath J. E.: Amorphous phenolphthalein-based poly(arylene ether) modified cyanate ester networks: 1. Effect of molecular weight and backbone chemistry on morphology and toughenability. Polymer, **39**, 2415–2427 (1998).
DOI: 10.1016/S0032-3861(97)00598-3

[10] Srinivasan S. A., McGrath J. E.: Amorphous bisphenol A based poly(arylene ether) modified cyanate ester networks. High Performance Polymers, **5**, 259–274 (1993).
DOI: 10.1088/0954-0083/5/4/001

[11] Kinloch A. J., Taylor A. C.: The toughening of cyanate-ester polymers: Part II Chemical modification. Journal of Materials Science, **38**, 65–79 (2003).
DOI: 10.1023/A:1021109731672

[12] Wooster T. J., Abrol S., Hey J. M., MacFarlane D. M.: The effect of particle matrix adhesion on the mechanical properties of silica filled cyanate ester composites. Macromolecular Materials and Engineering, **289**, 872–879 (2004).
DOI: 10.1002/mame.200400127

[13] Hwang J. W., Park S. D., Cho K., Kim J. K., Park C. E., Oh T. S.: Toughening of cyanate ester resins with cyanated polysulfones. Polymer, **38**, 1835–1843 (1997).
DOI: 10.1016/S0032-3861(96)00715-X

[14] Woo E. M., Shimp D. A., Seferis J. C.: Phase structure and toughening mechanism of a thermoplastic-modified aryl dicyanate. Polymer, **35**, 1658–1665 (1994).
DOI: 10.1016/0032-3861(94)90839-7

[15] Bucknall C. B., Partridge I. K.: Phase separation in crosslinked resins containing polymeric modifiers. Polymer Engineering and Science, **26**, 54–62 (1986).
DOI: 10.1002/pen.760260110

[16] Grishchuk S., Gryshchuk O., Weber M., Karger-Kocsis J.: Structure and toughness of polyethersulfone (PESU)-modified anhydride-cured tetrafunctional epoxy resin: Effect of PESU molecular mass. Journal of Applied Polymer Science, **123**, 1193–1200 (2012).
DOI: 10.1002/app.34610

[17] Woo E. M., Su C. C., Kuo J-F., Seferis J. C.: Model with experimental evidences for the morphology of binary blends of a thermosetting polycyanate with thermoplastics. Macromolecules, **27**, 5291–5296 (1994).
DOI: 10.1021/ma00097a008

[18] Pan Y., Xu Y., An L., Lu H., Yang Y., Chen W., Nutt S.: Hybrid network structure and mechanical properties of rodlike silicate/cyanate ester nanocomposites. Macromolecules, **41**, 9245–9258 (2008).
DOI: 10.1021/ma800819s

[19] Varughese K. T., Nando G. B., De P. P., De S. K.: Miscible blends from rigid poly(vinyl chloride) and epoxidized natural rubber. Journal of Materials Science, **23**, 3894–3902 (1988).
DOI: 10.1007/BF01106811

[20] Thomas S., Gupta B. R., De S. K.: Studies on morphology, mechanical properties and failure mode of blends of plasticized poly(vinyl chloride) and thermoplastic copolyester elastomer. Journal of Vinyl Technology, **9**, 71–85 (1987).
DOI: 10.1002/vnl.730090209

[21] Zhang X-R., Ma C-Y., Ke L., Jiang D.: Influence of compatibilization on the mechanical behavior and morphology of polyethersulfone/polycarbonate blends. High Performance Polymers, **23**, 212–218 (2011).
DOI: 10.1177/0954008311401440

[22] Thunga M., Satapathy B. K., Staudinger U., Weidisch R., Abdel-Goad M., Janke A., Knoll K.: Dynamic mechanical and rheological properties of binary S–(S/B)–S triblock copolymer blends. Journal of Polymer Science Part B: Polymer Physics, **46**, 329–343 (2007).
DOI: 10.1002/polb.21304

[23] Fainleib A., Bardash L., Boiteux G.: Catalytic effect of carbon nanotubes on polymerization of cyanate ester resins. Express Polymer Letters, **3**, 477–482 (2009).
DOI: 10.3144/expresspolymlett.2009.59

[24] Park S-J., Li K., Jin F-L.: Thermal stabilities and mechanical interfacial properties of polyethersulfone-modified epoxy resin. Journal of Industrial and Engineering Chemistry, **11**, 720–725 (2005).

[25] Bauer A., Thunga M., Obusek K., Akinc M., Kessler M. R.: Bisphenol E cyanate ester as a novel resin for repairing BMI/carbon fiber composites: Influence of cure temperature on adhesive bond strength. Polymer, **54**, 3994–4002 (2013).
DOI: 10.1016/j.polymer.2013.05.030

[26] Ramirez M. L., Walters R., Lyon R. E., Savitski E. P.: Thermal decomposition of cyanate ester resins. Polymer Degradation and Stability, **78**, 73–82 (2002).
DOI: 10.1016/S0141-3910(02)00121-0

[27] Badrinarayanan P., Rogalski M. K., Kessler M. R.: Carbon fiber-reinforced cyanate ester/nano-ZrW_2O_8 composites with tailored thermal expansion. ACS Applied Materials and Interfaces, **4**, 510–517 (2012).
DOI: 10.1021/am201165q

eXPRESS Polymer Letters Vol.8, No.5 (2014) 345–351
Available online at www.expresspolymlett.com
DOI: 10.3144/expresspolymlett.2014.38

Small-angle neutron scattering investigation of polyurethane aged in dry and wet air

Q. Tian[1], L. Almásy[2], G. Yan[1], G. Sun[1], X. Zhou[3], J. Liu[3], I. Krakovsky[4], M. Veres[2], L. Rosta[2], B. Chen[1]*

[1]Key Laboratory of Neutron Physics and Institute of Nuclear Physics and Chemistry, China Academy of Engineering Physics (CAEP), 621999 Mianyang, China
[2]Wigner Research Centre for Physics, Institute for Solid State Physics and Optics, P.O.Box 49, H-1525 Budapest, Hungary
[3]Institute of Chemical Materials, CAEP, 621999 Mianyang, China
[4]Department of Macromolecular Physics, Faculty of Mathematics & Physics, Charles University, V Holešovičkách 2, 180 00 Praha 8, Czech Republic

Received 14 September 2013; accepted in revised form 27 December 2013

Abstract. The microstructures of Estane 5703 aged at 70°C in dry and wet air have been studied by small-angle neutron scattering. The samples were swollen in deuterated toluene for enhancing the contrast. The scattering data show the characteristic domain structure of polyurethanes consisting of soft and hard segments. Debye-Anderson-Brumberger function used with hard sphere structure factor, and the Teubner-Strey model are used to analyze the two-phase domain structure of the polymer. The combined effects of temperature and humidity have a strong disruption effect on the microstructures of Estane. For the sample aged at 70°C in wet air for 1 month, the domain size, described by the correlation length, increases from 2.3 to 3.8 nm and their distance, expressed by hard-sphere interaction radius, increases from 8.4 to 10.6 nm. The structure development is attributed to degradation of polymer chains as revealed by gel permeation chromatography. The hydrolysis of ester links on polymer backbone at 70°C in the presence of water humidity is the main reason for the changes of the microstructure. These findings can contribute to developing predictive models for the safety, performance, and lifetime of polyurethanes.

Keywords: *material testing, SANS, Estane 5703, polyurethane, aging*

1. Introduction

Polyurethanes (PUs) are a very attractive type of segmented polymers with unique mechanical properties derived from thermodynamic incompatibility between flexible soft segments (SSs) and covalently attached hard segments (HSs). They have important applications, such as surface coatings and sealants, high performance adhesives, durable elastomeric wheels and tires, rigid foam insulation panels, blood contact medical devices and shape memory materials [1]. PUs are usually intended for long-term use. In general, the mechanical properties of PUs are highly dependent on the microstructural changes induced by extended exposure to various agents, such as temperature, humidity, and irradiation.

The subject of this work is a commercial segmented PU with low HS content, known as Estane 5703. It is incorporated into high explosive formulations to impart structural integrity to the composite and to decrease its sensitivity to undesired stimuli. Mang *et al*. [2] revealed that Estane mixed with nitroplasticizer has a significant change of microstructures after aging for 1.5 months at 70°C. Orler *et al*. [3] found that Estane 5703 aged at 70°C in dry air quickly restored its initial mechanical properties, while the mechanical properties of the samples aged at 70°C

*Corresponding author, e-mail: tqsuperego@163.com

in wet air only partially recovered with time. Since Estane 5703 strongly affects the mechanical properties of the composites, it is essential to know how the material changes with time at various environmental conditions. Small-angle scattering technique is a very powerful tool for investigating internal structures of PUs [2, 4–9]. Mang and coworkers [2, 9] applied small-angle neutron scattering (SANS) technique to determine the domain structures in deuterated Estane with low HS content. To the best of our knowledge, there is little information on nanoscale structural changes in Estane aged at different temperature and humidity conditions.

Our motivation is to reveal the influence of aging on the microstructures of Estane by applying a scattering method, which is a direct probe of the structure on the nanometer length scales. These results will aid in understanding the structure-property correlations, as well as the development of predictive models for the safety, performance, and lifetime of polyurethanes.

2. Experimental section

2.1. Materials

Estane 5703 obtained as pellets from the Lubrizol Advanced Materials, Inc., US, contains about 23 wt% HSs. The SSs are polymers (oligomers) of the ester of adipic acid with 1,4 butanediol; they have an average molecular weight in the range of 800 to 1050 Da [9]. The HSs consist of very short polyurethanes made from 4,4′-diphenylmethane diisocyanate molecules bonded together by urethane links to the butanediol that serve as chain extenders, as shown in Figure 1.

Estane pellets were compression-molded into 1 mm thick disk at 20 MPa, 120°C for 10 minutes and then cooled to room temperature (*RT*), initiating the phase separation process. The Estane samples (10×10×1 mm) were sealed in containers to maintain the wet and dry environments. Water for 100% relative humidity (*RH*) condition and silica gel desiccant for dry condition were employed inside the sealed containers. The sealed containers were placed at *RT* and 70°C for 1 and/or 2 months. All the aged samples were allowed to equilibrate at *RT* for not less than 3 months. The samples were swollen by deuterated toluene for 48 hours before SANS measurements in order to reach equilibrium swelling and enhance the scattering contrast between HS and SS domains, and were measured in the swollen state.

2.2. Characterization

The SANS measurements were performed with the small-angle neutron scattering diffractometer 'Yellow Submarine' at the Budapest Research Reactor. A mean neutron wavelength of 0.47 and 1.175 nm was selected by mechanical velocity selector. The sample-detector distance was 1.57 and 5.50 m respectively. By changing the wavelength and sample-detector distance, we have covered a q range of 0.08–2.5 nm^{-1}. The acquisition times were 30 minutes for each sample at each detector position. Immediately before the measurements, the swollen samples were transferred into quartz cells of path length 2 mm and filled with deuterated toluene (Figure 2). The scattering data were processed using BerSANS software [10]. The data reduction corrects the raw measured data for the contributions of the background, transmission, scattering from empty cell and normalizes the data to the efficiency of the individual cells of the multidetector.

The gel permeation chromatography (GPC) measurements were performed using a Biospher GMB 100 column (8×500 mm, Labio, Czech Republic) filled with 10 μm sorbent particles. Tetrahydrofuran (Sigma-Aldrich), distilled and dried over molecular sieves (4 Å), was used as a mobile phase at a flow rate 1 mL/min. Small amount of toluene (2% (w/v))

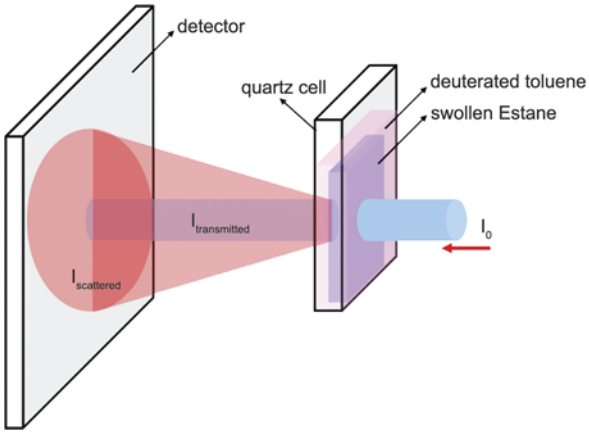

Figure 2. Schematic diagram of the SANS measurements of swollen Estane

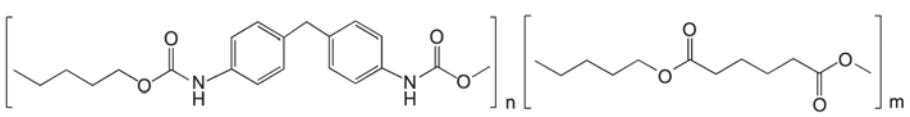

Figure 1. Molecular structure of Estane 5703

was used as internal standard. The data from a refractive index detector were collected and treated by using CSW 1.7 software (Data Apex, Czech Republic). For the determination of molar masses, a universal calibration equation calculated from the data on polystyrene standards (Polymer Standards Service) was used.

2.3. Data analysis

Polyurethanes containing 40% or less HSs (by weight) are known to have a discrete hard microdomain structure [4]. A broad peak seen in all data (Figures 3 and 4) confirms that this is the case in the studied samples. In the simplest approximation, the peak position (q_0) gives the average distance between the domains as $d = 2\pi/q_0$. It can be seen, that with aging, the peak shifts to lower q values, indicating the increase of the interdomain distance. To extract more information, the SANS scattering data are usually analyzed by fitting parameters of model functions to the data, provided that appropriate models are known for the investigated structure. In the present case, the simplest plausible model of domains in a matrix was the ensemble of hard spheres with spatial distribution according to hard sphere interaction potential. However, such model did not give adequate fits, even when enhancing the model to include polydispersity, or using different hard sphere and interaction radii. Such results were not unexpected, given the hard domains do not necessarily have compact shapes and smooth interfaces. For a similar polymer containing hard domains in a soft matrix, Krakovsky and coworkers [5, 6] found empirically

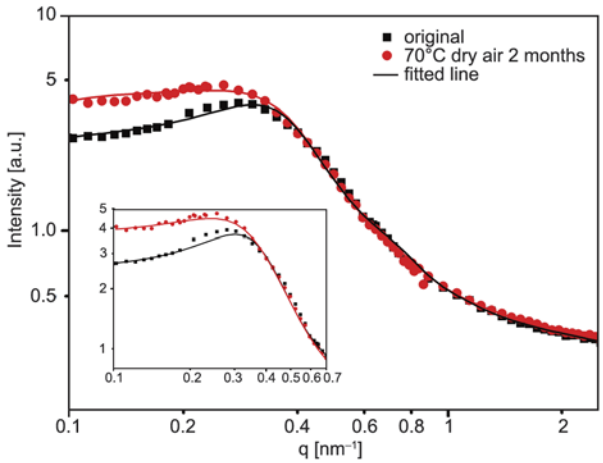

Figure 3. SANS data of the original Estane and aged Estane at 70°C in dry air for 2 months, the solid lines are the fitting results by DAB-PY model. The inset shows the fitting results by TS model.

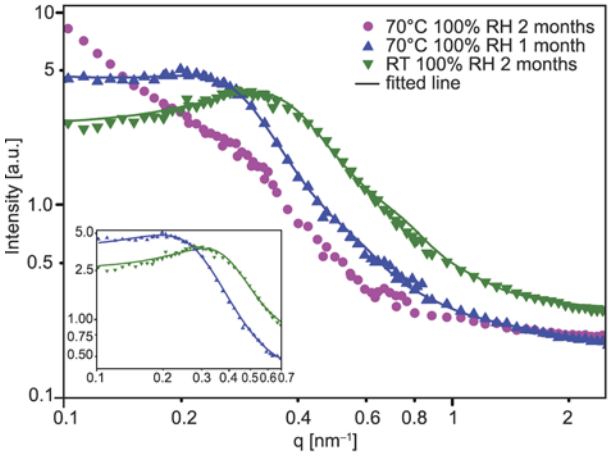

Figure 4. SANS data of Estane aged at 70°C in wet air for 1 and 2 months, as well as at RT in wet air for 2 months, the solid lines are the fitting results by DAB-PY model. The inset shows the fitting results by TS model.

that the scattering from PUs based on poly(butadiene)diol, 4,4'-diphenylmethane diisocyanate and poly(oxypropylene) triol can be adequately described using the Debye, Anderson and Brumberger (DAB) model for the hard domain shape. Although this is not a form factor of a compact object, in combination with the hard sphere interdomain structure factor it described reasonably well the scattering data, presumably because the right asymptotical behavior of the DAB model in the measured q interval. The DAB model for random two-phase morphology is written by Equation (1):

$$P(q) = \frac{1}{(1 + a_{corr}^2 q^2)^2} \tag{1}$$

where a_{cor} is correlation length. It represents the length over which the structural correlation decays. This model assumes smooth interfaces between the phases. The HSs content of Estane is low and consequently the hard-domains are much smaller than the chords crossing the soft and hard domains, therefore a_{cor} can be considered as an approximation of the average hard domain size [11, 12]. The formula of the Percus-Yevick (PY) type for the interference factor, applicable for hard sphere interaction, is shown in Equation (2):

$$S(q) = \frac{1}{1 + \dfrac{24\nu G(A,\nu)}{A}} \tag{2}$$

where

$A = 2qR_{HS}$

$$G=\frac{\alpha}{A^2}(\sin A-A\cos A)+\frac{\beta}{A^3}[2A\sin A+(2-A^2)\cos A-2]+\frac{\gamma}{A^5}\{-A^4\cos A+4[(3A^2-6)\cos A+(A^3-6)\sin A+6]\}$$

$$\alpha=\frac{(1+2v)^2}{(1-v)^4}$$

$$\beta=-\frac{6v\left(1+\frac{v}{2}\right)^2}{(1-v)^4}$$

$$\gamma=\frac{v(1+2v)^2}{2(1-v)^4}$$

R_{HS} and v denote the hard-sphere interaction radius and volume fraction, respectively [13]. The first strong peak in the PY structure factor is related to a preferential distance between adjacent hard domains. Herein, we take the DAB plus PY as an approximate model to fit the scattering intensities by Equation (3):

$$I(q) = A\cdot P(q,a_{cor})\cdot S(q,R_{HS},v) + I_B \quad (3)$$

where A is a scale factor, and the background intensity, $I_B = A_1 + A_2q^4$, accounts for the incoherent scattering and for large inhomogeneities, herein A_1 and A_2 are adjustable parameters. The fitted results are shown in Table 1. Good agreement is found between the measured data and the model function, except for the sample aged at 70°C for 2 months in wet air. Since the presence of separated and uniform HS domains is clearly an oversimplification, the scattering data were also fitted to Teubner-Strey (TS) model, which, according to Equations (4)–(6) describes a random two phase structure with locally lamellar order:

$$I(q) = \frac{1}{a_2 + c_1q^2 + c_2q^4} + b \quad (4)$$

Table 1. Structural parameters obtained from SANS data on aged Estane 5703 samples swollen by d-toluene by curve-fitting using the DAB-PY model and TS model

Sample	DAB-PY model			TS model	
	a_{cor} [nm]	RHS [nm]	v	ξ [nm]	D [nm]
Original	2.3	8.4	0.15	6.1	18.2
70°C 2 months dry air	2.5	8.8	0.12	5.9	20.1
RT 2 months 100% RH	2.3	8.3	0.15	6.0	18.0
70°C 1 month 100% RH	3.8	10.6	0.15	7.0	25.9

$$\xi = \left[\frac{\left(\frac{a_2}{c_2}\right)^{1/2}}{2} + \frac{c_1}{4c_2}\right]^{-1/2} \quad (5)$$

$$D = 2\pi\left[\frac{\left(\frac{a_2}{c_2}\right)^{1/2}}{2} - \frac{c_1}{4c_2}\right]^{-1/2} \quad (6)$$

where b is a background and a_2, c_1, and c_2 are composition-dependent coefficients, related to two characteristic lengths, D and ξ, which appear in the spatial correlation function of the system [14]. D represents a quasi-periodic repeat distance of hard domains, and ξ is the correlation length. Hydrogels containing two phases and aqueous solutions of short chain surfactants often show such structure [15, 16]. For our samples, the TS model gives good fit only over a restricted q region from 0.1 to 0.7 nm^{-1}, indicating that it does not describe fully the polymer structure on the length scale below 10 nm. The characteristic periodicity or interdomain spacing is nevertheless well captured by this model. The fitted results are shown in Table 1. All the data was fitted by SASfit software [17].

3. Results

3.1. Behavior in dry air

The $I(q)$ curves of Estane 5703 aged in dry air at *RT* and 70°C for 2 months are shown in Figure 3. The sample aged in dry air at RT is further referred as the original sample. A distinct interference peak is observed at q = 0.3 nm^{-1}, which shifts with increasing aging temperature, towards smaller q-values, indicating increase of the interdomain distance. After aging at 70°C for 2 months in dry air, R_{HS} increases from 8.4 to 8.8 nm and a_{cor} increases from 2.3 to 2.5 nm; D increases from 18.2 to 20.1 nm and ξ decreases from 6.1 to 5.9 nm. These results indicate that the hard domain size keeps nearly unchanged while the distance between adjacent hard domains increases. $2R_{HS}$ and D are the characteristic distance and the average quasi-periodic distance of adjacent HS domains, in the two models, respectively. All samples exhibit a broad GPC peak (see Figure 5). Exposition of Estane to dry air at 70°C causes a small shift of the GPC peak to higher elution volume which is equivalent to shift of its molec-

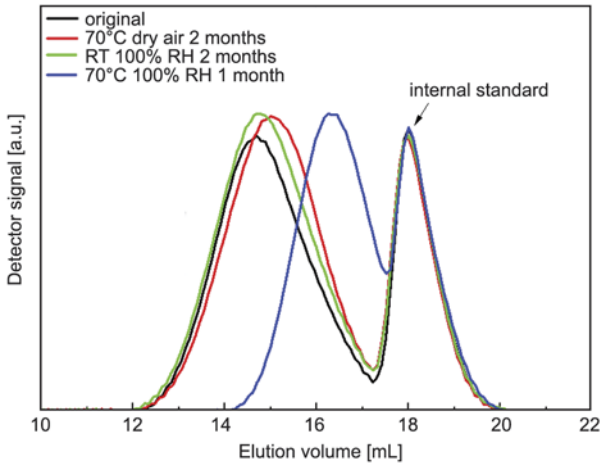

Figure 5. GPC curves for Estane aged at different environmental conditions

ular weight distribution to somewhat smaller values.

3.2. Behavior in wet air

The $I(q)$ curves of the samples aged at *RT* and 70°C for 1 and 2 months in wet air are shown in Figure 4. The scattering curve and the fitted parameters keep nearly unchanged for the sample after aging at *RT* in wet air for 2 months. At elevated temperature, 70°C, however, a strong change of the sample structure is seen. After 1 month, the interference peak shifts to $q = 0.2$ nm^{-1}, reflecting a significant increase in spacing between the discrete domains. Fitting by the aforementioned models, the structural parameters develop as follows: after 1 month, at 70°C and 100% RH, a_{cor} increases from 2.3 to 3.8 nm and R_{HS} increases from 8.4 to 10.6 nm; ξ increases from 6.1 to 7.0 nm and D increases from 18.2 to 25.9 nm. Further treatment at 70°C in wet air for 2 months leads to a drastic change of the structure. The scattering at small q values becomes strong, which indicates the appearance of a new population of scatters with the characteristic sizes above 100 nm. The domains of HSs are still observable from the interference peak, however the model fits are no longer accurate due to the strong forward scattering. It appears that during this treatment the microstructure is badly destroyed, and, most importantly, the structure looses its homogeneity on the length scale above 100 nm. As shown in Figure 5, exposition of Estane to wet air at *RT* does not show any effect on position and width of the GPC peak. However, the peak is shifted considerably under exposition of the material to wet air at elevated temperature (70°C) which signifies a shift of molecular weight distribution of polymer to much lower values.

4. Discussion

The hard domain size keeps nearly unchanged and the distance between hard domains increases for the samples aged at 70°C in dry air for 2 months, which could be explained by the remixing of small HSs into the soft phase. The glass transition temperature of hard domains in Estane is around 70°C, and at this temperature part of HSs and SSs are remixed. The rather broad scattering peak shows a wide distribution in the size of the HS and SS domains. The shorter HSs can dissolve within the SSs if their length is below the critical length for microphase separation [4]. Therefore the aging may preferentially destroy the smaller HSs domains, which could result in the shift of the peak to low q-value and the increase of the average hard domain distance.

Our experiments reveal that the combined effects of temperature (70°C) and humidity (100% RH) strongly modify the nanoscale structure of Estane 5703. It can be inferred that the hydrolysis at 70°C is the main reason for the changes of hard domains distance and size. The ester group is most susceptible to hydrolysis, which reverts RCOOR' to polymeric acid (RCOOH) and polymeric alcohol (R'OH) [18, 19]. This is a chain scission reaction inducing the decrease of the molecular weights of the polymer chains. The GPC results shown in Figure 5 and parameters determined from them are in agreement with this observation (Table 2). Compared with the original sample, the molecular weight of Estane aged at 70°C in wet air for 1 month decreased about 9-fold, while the molecular weights of Estane aged at *RT* in wet air and 70°C in dry air for 2 months have a little drop. Thompson *et al*. [20] also proved that the molecular weights for Estane aged in wet air decreased strongly after 20 days. Moreover, we

Table 2. Molecular weight distribution parameters obtained from GPC data on aged Estane 5703 samples: M_n and M_w denote number- and weight-average (polystyrene equivalent) of molecular weight, respectively

Sample	M_n [g/mol]	M_w [g/mol]	M_w/M_n
Original	32 000	104 000	3.3
70°C 2 months dry air	26 700	113 000	4.2
RT 2 months 100% RH	33 000	106 000	3.2
70°C 1 month 100% RH	3 600	7 900	2.2

found that part of the Estane samples aged at 70°C and 100% RH were dissolved in toluene, while no obvious dissolution for the samples aged in dry air was observed. This appears to be the consequence of the hydrolysis of the ester links and decrease of the molecular weight [18].

The increase in hard domains distance can be mainly attributed to the chain scission of SSs. It is reported that the ester segments are more than an order of magnitude more susceptible to hydrolytic cleavage than the urethane [21]. This means the chain scission would induce a looser structure in SSs, which in turn, may lengthen the distance between adjacent hard domains. The increase in hard domain size is also related with the hydrolysis. First, it is energetically favourable for the SSs and HSs not to mix. The phase separation process is inhibited by steric and mobility constraints. Second, the SSs mobility of the hydrolyzed Estane is increased due to the decrease of the molecular weights after hydrolysis. Hence the organization of the HSs into domains becomes easier, and the HS domains incline to grow bigger than those of the non-aged or dry-aged samples. This analysis is in accordance with the literature, which reported that the increased molecular weights and decreased chain mobility of nitroplasticized Estane caused by branching undergoes a less degree of phase separation [22]. Furthermore, the tensile strength of the samples aged at 70°C in wet air (75% RH) for 27 and 59 days was reduced by 58 and 93% respectively with respect to the corresponding values measured before aging [3]. Hence the increase of hard domain size and distance correlates straightly with the chemical changes and the change of the mechanical properties of Estane. In summary, the microstructural changes of the studied Estane 5703 are shown in Figure 6.

70°C	2 months The domains dissolve R_{HS} = 8.8 nm D = 20.1 nm	1 month R_{HS} = 10.6 nm D = 25.9 nm Hydrolysis is the reason. 2 months The microstructure is badly destroyed.
Room temperature	DAB-PY model: R_{HS} = 8.4 nm a_{cor} = 2.3 nm TS model D = 18.2 nm ξ = 6.1 nm	Hard domain size and distance keep nearly unchanged.
	Dry air	Wet air (100% RH)

Figure 6. Summary diagram of the microstructural changes of Estane 5703 at various aging conditions

5. Conclusions

Microstructures of Estane swollen in deuterated toluene after aging at 70°C in dry air and wet air have been studied by SANS technique. The hard domain size keeps nearly unchanged and the distance between hard domains increases for the samples aged in dry air for 2 months. Both the domain sizes and their distances, analyzed by DAB-PY and TS models, are increased for the humidity-aged sample at 70°C for 1 month. Further treatment at 70°C in wet air for 2 months leads to restructuring or degradation of the sample observable at a larger length scale, with characteristic size above 100 nm. The combined effects of temperature and humidity strongly modify the nanoscale structure of Estane 5703. The hydrolysis of ester links at 70°C that causes a decrease of average molecular weight of the polymer chains is the main reason for these changes. This study contributes to understanding the structure-property correlations of polyurethanes in different environments.

Acknowledgements

This work was supported by the National Natural Science Foundation of China under grant Nos. 11205137, 11079043, and 11302199, and by project KMR12-1-2012-0226 granted by the National Development Agency (NDA) of Hungary. We thank the many useful suggestions of the anonymous referees.

References

[1] Prisacariu C.: Polyurethane elastomers: From morphology to mechanical aspects. Springer, Wien (2011).

[2] Mang J. T., Peterson P. D., Orler E. B., Wrobleski D. A., Langlois D. A., Espada L. I., Hjelm R. P.: Small-angle neutron scattering study of a thermally aged, segmented poly(ester urethane) binder. Neutron News, **14**, 26–28 (2003). DOI: 10.1080/10448630308218510

[3] Orler E. B., Wrobleski D. A., Smith M. E.: Hydrolytic degradation of Estane 5703. Los Alamos National Laboratory, US, No. LA-UR-99-1383 (1999).

[4] Koberstein J. T., Galambos A. F., Leung L. M.: Compression-molded polyurethane block copolymers. 1. Microdomain morphology and thermomechanical properties. Macromolecules, **25**, 6195–6204 (1992). DOI: 10.1021/ma00049a017

[5] Krakovský I., Bubeníková Z., Urakawa H., Kajiwara K.: Inhomogeneous structure of polyurethane networks based on poly(butadiene)diol: 1. The effect of the poly (butadiene)diol content. Polymer, **38**, 3637–3643 (1997).
DOI: 10.1016/S0032-3861(96)00897-X

[6] Krakovský I., Urakawa H., Kajiwara K.: Inhomogeneous structure of polyurethane networks based on poly(butadiene)diol: 2. Time-resolved SAXS study of the microphase separation. Polymer, **38**, 3645–3653 (1997).
DOI: 10.1016/S0032-3861(96)00898-1

[7] Koberstein J. T., Russell T. P.: Simultaneous SAXS-DSC study of multiple endothermic behavior in polyether-based polyurethane block copolymers. Macromolecules, **19**, 714–720 (1986).
DOI: 10.1021/ma00157a039

[8] Blundell D. J., Eeckhaut G., Fuller W., Mahendrasingam A., Martin C.: Real time SAXS/stress–strain studies of thermoplastic polyurethanes at large strains. Polymer, **43**, 5197–5207 (2002).
DOI: 10.1016/S0032-3861(02)00386-5

[9] Mang J. T., Hjelm R. P., Orler E. B., Wrobleski D. A.: Small-angle neutron scattering of a solvent-swollen segmented polyurethane as a probe of solvent distribution and polymer domain composition. Macromolecules, **41**, 4358–4370 (2008).
DOI: 10.1021/ma800015g

[10] Keiderling U.: The new 'BerSANS-PC' software for reduction and treatment of small angle neutron scattering data. Applied Physics A, **74**, 1455–1457 (2002).
DOI: 10.1007/s003390201561

[11] Debye P., Anderson R., Brumberger H.: Scattering by an inhomogeneous solid. II. The correlation function and its application. Journal of Applied Physics, **28**, 679–683 (1957).
DOI: 10.1063/1.1722830

[12] Linliu K., Chen S-A., Yu T. L., Lin T-L., Lee C-H., Kai J-J., Chang S-L., Lin J. S.: A small-angle X-ray scattering study of microphase separation transition of polyurethanes: Effect of hard segments. Journal of Polymer Research, **2**, 63–70 (1995).
DOI: 10.1007/BF01493435

[13] Percus J. K., Yevick G. J.: Analysis of classical statistical mechanics by means of collective coordinates. Physical Review, **110**, 1–13 (1958).
DOI: 10.1103/PhysRev.110.1

[14] Li W., Ryan A. J., Meier I. K.: Morphology development via reaction-induced phase separation in flexible polyurethane foam. Macromolecules, **35**, 5034–5042 (2002).
DOI: 10.1021/ma020035e

[15] Krakovský I., Székely N.: Small-angle neutron scattering study of nanophase separated epoxy hydrogels. Journal of Non-Crystalline Solids, **356**, 368–373 (2010).
DOI: 10.1016/j.jnoncrysol.2009.11.037

[16] D'Arrigo G., Giordano R., Teixeira J.: Temperature and concentration dependence of SANS spectra of aqueous solutions of short-chain amphiphiles. The European Physical Journal E, **29**, 37–43 (2009).
DOI: 10.1140/epje/i2008-10447-7

[17] Kohlbrecher J.: SASfit: A program for fitting simple structural models to small angle scattering data. Paul Scherrer Institute, Laboratory for Neutron Scattering (2011).

[18] Gardner R. J., Martin J. R.: Effect of relative humidity on the mechanical properties of poly(1,4-butylene terephthalate). Journal of Applied Polymer Science, **25**, 2353–2361 (1980).
DOI: 10.1002/app.1980.070251021

[19] Salazar M. R., Lightfoot J. M., Russell B. G., Rodin W. A., Mccarty M., Wrobleski D. A., Orler E. B., Spieker D. A., Assink R. A., Pack R. T.: Degradation of a poly (ester urethane) elastomer. III. Estane 5703 hydrolysis: Experiments and modeling. Journal of Polymer Science: Part A: Polymer Chemistry, **41**, 1136–1151 (2003).
DOI: 10.1002/pola.10656

[20] Thompson D. G., Osborn J. C., Kober E. M., Schoonover J. R.: Effects of hydrolysis-induced molecular weight changes on the phase separation of a polyester polyurethane. Polymer Degradation and Stability, **91**, 3360–3370 (2006).
DOI: 10.1016/j.polymdegradstab.2006.05.019

[21] Fambri L., Penati A., Kolarik J.: Synthesis and hydrolytic stability of model poly(ester urethane ureas). Angewandte Makromolekulare Chemie, **228**, 201–219 (1995).
DOI: 10.1002/apmc.1995.052280116

[22] Orler E. B., Wrobleski D. A., Cooke D. W., Bennett B. L., Smith M. E., Jahan M. S.: Thermal aging of nitroplasticized Estane 5703. Los Alamos National Laboratory, US, No. LA-UR-02-1315 (2002).

eXPRESS Polymer Letters Vol.8, No.5 (2014) 352–361
Available online at www.expresspolymlett.com
DOI: 10.3144/expresspolymlett.2014.39

Nanofibrous solid dosage form of living bacteria prepared by electrospinning

Zs. K. Nagy[1], I. Wagner[1], Á. Suhajda[2], T. Tobak[1], A. H. Harasztos[2], T. Vigh[1], P. L. Sóti[1], H. Pataki[1], K. Molnár[3,4], Gy. Marosi[1]*

[1]Budapest University of Technology and Economics, Department of Organic Chemistry and Technology, 1111 Budapest, Budafoki út 8., Hungary
[2]Budapest University of Technology and Economics, Department of Applied Biotechnology and Food Science, 1111 Budapest, Szent Gellért tér 4., Hungary
[3]Budapest University of Technology and Economics, Department of Polymer Engineering, 1111 Budapest, Műegyetem rkp. 3., Hungary
[4]MTA-BME Research Group for Composite Science and Technology, 1111 Budapest, Műegyetem rkp. 3., Hungary

Received 9 October 2013; accepted in revised form 27 December 2013

Abstract. The aim of this work was to investigate the suitability of electrospinning for biodrug delivery and to develop an electrospinning-based method to produce vaginal drug delivery systems. *Lactobacillus acidophilus* bacteria were encapsulated into nanofibers of three different polymers (polyvinyl alcohol and polyvinylpyrrolidone with two different molar masses). Shelf life of the bacteria could be enhanced by the exclusion of water and by preparing a solid dosage form, which is an advantageous and patient-friendly way of administration. The formulations were stored at –20, 7 and 25°C, respectively. Viability testing showed that the nanofibers can provide long term stability for huge amounts of living bacteria if they are kept at (or below) 7°C. Furthermore, all kinds of nanowebs prepared in this work dissolved instantly when they got in contact with water, thus the developed biohybrid nanowebs can provide new potential ways for curing bacterial vaginosis.

Keywords: *nanomaterials, electrospinning, vaginal web, nanofibers, biohybrid nanoweb*

1. Introduction

One of the main challenges of pharmaceutical technology at the beginning of the 21st century, which is the great period of biotechnology, is the formulation of biopharmaceuticals (proteins, peptides, nucleic acids, living cells, viral particles and vaccines). These objects are generally very sensitive to the physical and chemical impacts of their environment [1]. Solid dosage forms are preferred to liquid ones from stability, dose accuracy, shipping, handling, and patient-compliance points of view; however, drying is a limiting factor in their formulation. After the biotechnological processes, gentle removal of the commonly applied water would be desirable to keep the structure of bio-drugs unaltered [2].

Electrospinning (electrostatic spinning, *ES*) is a remarkably simple and efficient technique to generate fine polymeric fibers in submicron – and nano – scale from polymer solutions (or melts) using high electric voltage [3]. Electrospinning provides an extremely rapid (less than 0.1 s [4]) and very gentle drying step at ambient temperature due to the direct interactions between the electrostatic energy and the working fluids and to the huge surface area of the fluid jets during the bending and whipping processes. This fiber forming process has been primarily devel-

*Corresponding author, e-mail: istvanwagner@gmail.com

oped in the textile industry [5–8], but in the recent years, applications have been published also in various biomedical fields such as wound dressing [9], wound healing [10], sterile filtration [11], tissue engineering [12, 13] and drug delivery [14–19].

In former studies bioactive ingredients such as proteins and DNA have been embedded successfully in nanofibers mainly for tissue engineering purposes, while living prokaryotic cells were encapsulated by this technique mainly for industrial application in bioreactors utilizing their metabolic activity [20–22]. Zussman [23] has recently reviewed the preparation methods of electrospun polymer fibers encapsulating cells and their potential applications. Salalha *et al*. [24] showed that *Escherichia coli* and *Staphylococcus albus* remained viable after electrospinning process and retained their viability in polyvinyl alcohol (PVA) matrix for at least 3 months when the bacteria-containing electrospun webs were stored at –20 and –55°C. Lopez-Rubio *et al*. [25] incorporated living probiotic bacteria (*B. animalis Bb12*) into PVA nanofibers applying co-electrospinning and the cells remained viable after 40 days at room temperature and 130 days at 4 and –20°C under refrigeration. Henceforth they encapsulated *B. animalis Bb12* into protein- and carbohydrate-based microcapsules using electrospraying [26]. Similarly, Heunis *et al*. [27] and Fung *et al*. [28] embedded *Lactobacillus* bacteria into polymer nanofibers with moderate survival rate (2% [27] and 1–10% [28]).

Lactobacillus acidophilus is one of the most widely investigated and used species especially in the field of dairy industry and it is an important part of normal human bacterial flora usually located in mouth, gastrointestinal tract and the urinary and genital tract of females [29, 30]. The most common vaginal disease (at ages 14–49), the bacterial vaginosis (polymicrobial syndrome caused by an imbalance of normal vaginal micro flora) is in connection with the lack of *Lactobacillus* bacteria and its substitution by exogenous bacteria [31]. Vaginal pH rises up over 4.5 during bacterial vaginosis and *Lactobacillus* bacteria may disappear almost completely [32]. Curing of this disorder is a considerable challenge of the healthcare worldwide because about one third of females are affected (29% in the United States [33]). In normal vaginal microbiota, a huge number of *Lactobacillus* bacteria exist, which prevent the colonization and proliferation of pathogenic microorganisms through several ways, such as competition for nutrients and adherence, production of H_2O_2 [34], bacteriocins [35] and lactic acid, which is mainly responsible for the protective acidic pH of the vagina [36]. Several clinical studies showed that intravaginal administration of *Lactobacillus acidophilus* resulted in a significantly increased number of recoveries compared to treatments with placebo, acetic acid or no treatment [37–40]. Furthermore, a recent review drew attention to the increased importance of probiotic treatment for prevention of bacterial vaginosis so that more serious complications can be avoided [41]. The efficacy of standard antibiotic treatments has been decreasing (because of the spreading of resistant bacteria strains and due to the increasing refusal of antibiotics by patients). Therefore, new, effective, readily accessible and economical lactobacilli-based probiotic therapies are badly needed [41]. It meets the purpose of this work since water-based electrospinning is a simple, scalable and continuous technology with very low energy consumption [8, 17, 42]. Furthermore, development of effective drug delivery systems for living cells and other biopharmaceuticals is a general need of pharmaceutical technology owing to the newly appearing biomedicals [43].

The aim of this work was to develop an electrospinning-based method for encapsulation of *Lactobacillus acidophilus* (LBA) and to investigate the applicability of electrospinning technology for preparing vaginal drug delivery systems in the form of biohybrid nanowebs (BNW) for curing of bacterial vaginosis.

2. Experimental section

2.1. Materials

Lactobacillus acidophilus (Strain number: B1075) was kindly provided by National Collection of Agricultural and Industrial Microrganisms (Budapest, Hungary).

Polyvinyl pyrrolidone (PVP) with two different chain lengths (molecular weight: PVP K30: ~50 000 Da, PVP K90: ~1 200 000 Da), kindly provided by BASF (Ludwigshafen, Germany) and polyvinyl alcohol (PVA), purchased from Fluka (Buchs, Switzerland, molecular weight: 130 000 Da), were used as polymer matrices. Solvent was distilled water.

2.2. Selection of optimal concentration of polymer solution

The optimal concentration of the polymer solutions was determined without LBA. The polymers were added into 10 mL of purified water and stirred by ARE magnetic stirrer (VELP Scientifica, Usmate, Italy) at 600 rpm and 50°C until complete dissolution was achieved. The mass percents of polymer solutions were as follows: PVA 130 000 and PVP K90: 5, 10, 15, 20%; PVP K30: 20, 25, 30, 35, 40, 45, 50%. The solutions and the collected electrospun materials were investigated with a rheometer, and by optical and electron microscopy, respectively.

2.3. Preparation of bacterial suspensions and bacteria-containing polymer suspensions

Stock culture was subcultured in MRS agar (LabM, Bury, United Kingdom). The MRS agar was freshly prepared and sterilized. According to the instructions of the manufacturer 70 g of MRS agar powder was added to 1 L of deionized water. The system was heated and mixed properly and after total dissolution it was autoclaved at 121°C. In each experiment, the bacteria were harvested from the surface of 3 MRS agar cultures, with approx. 5 mL of sterilized water, and were dispersed properly with a Vortex mixer. 5 mL of bacterial suspension was added to 10 g (1.5 g PVA, 8.5 g dist. water) of aqueous PVA solution and 5 g (2.2 g PVP K90, 3.8 g dist. water) of aqueous PVP K90 solution. In the case of PVP K30, the polymer (2.25 g) was added directly to the bacterial suspension (3 mL). Hereinafter they were mixed properly with magnetic stirrer at 600 rpm and room temperature. The polymer concentrations of the obtained suspensions were as follows: PVA: 10 w/w%, PVP K90: 20 w/w%, PVP K30: 45 w/w%.

2.4. Electrospinning

The electrostatic spinner used for the experiments was equipped with NT-35 High Voltage DC Supply (MA2000, Nagykanizsa, Hungary). The utilized electrical potential on the spinneret electrode was 35 kV, which was adjusted during the experiments. A grounded steel plate covered with polytetrafluoroethylene was used as collector. Polymer solutions were dosed by SEP-10S Plus syringe pump (Aitecs, Vilnius, Lithuania). The distance between the spinneret and the collector was 15 cm in all cases and the experiments were performed at room temperature (25°C). Electrospinning was carried out in fume hood. The continuous ventilation provided constant humidity during the process owing to the same inlet air. Relative humidity was around 35%, temperature was 25°C.

2.5. Rheological measurements

Viscosity of the solutions was determined using an AR 2000 rotational rheometer (TA Instruments, New Castle, USA) in parallel plate configuration. The upper moving plate of 40 mm diameter and the lower Peltier plate, which adjusted the temperature of the solutions to 25°C, were made of stainless steel.
The viscosities were measured at torques increasing logarithmically from 10 to 1000 μNm·Pa. The shown viscosities are the averages of 10 measured values at different torques (no significant changes were estimated as a function of torque).

2.6. Scanning electron microscopy (SEM)

Morphology of the samples was investigated with a JEOL 6380LVa (JEOL, Japan) type scanning electron microscope. Each specimen was fixed by conductive double sided carbon adhesive tape and sputtered by gold (using a JEOL 1200 instrument).

2.7. Viability test

In order to determine the number of colony forming units in the prepared nanowebs and in the initial solutions of electrospinning after 4 h, their weighed pieces were dissolved completely using 5 mL of sterilized water (stock solution). Hereinafter these initial solutions were diluted in nine steps (1 step = 10-fold dilution) and after each step 1 mL of solution was pipetted onto MRS agar plate. Agar plates were kept in a lockup plastic box containing activated Microbiology Anaerocult® (Merck, Darmstadt, Germany), which provides anaerobic circumstances by adsorption of oxygen. These were held at 37°C for 48 hours then the formed colonies were enumerated (colony forming unit = CFU). CFU number of 1 g of initial solution was calculated as 100%.

2.8. Storage test

Samples containing LBA were kept in lockup containers at the typically used storage temperatures (7, 20°C), what correspond to the temperatures of a freezer and a fridge respectively. Viability of LBA bacteria in the nanofibers was investigated during the storage period (3 months) and CFU/g was determined. The method applied to determine cell viabil-

ity was the plating procedure described in the Viability test part.

2.9. Dissolution test

In order to determine the release time of LBA from each nanoweb, 100 mg of them were dissolved in 10 mL of dist water. Dissolution vessels were shaken with a speed of 50 rpm. After 1, 2, 3, 5, 10 and 60 min, 1 mL of the solution was pipetted to an MRS agar plate and the dissolution media was refilled with dist. water. The method of plating procedure was the same that described above. Dissolution was calculated as follows: the CFU number at different time points was divided by the total CFU number at the end of the dissolution test, which was considered as 100%. The release from membranes was measured with three samples in each case, and the relative standard deviations were below 5%.

3. Results and discussion

At first, the electrospinning process of polymers was optimized without bacteria and the collected dried products were investigated by SEM. Bacteria containing polymer solutions were prepared at the determined optimal concentration. The effect of the polymers on the viability of the bacteria was examined as a function of time through 4 h at 25°C. After that bacteria containing polymer solutions were electrospun. The obtained morphology was investigated by SEM; the survival rate of the bacteria was quantified by viability tests. Storage tests of the electrospun products were also accomplished at two different temperatures through 3 months.

3.1. Optimization of polymer concentration

Before the encapsulation of LBA, the optimal concentrations of polymers in the solution to feed for electrospinning were determined. The polymers applicable for pharmaceutical purposes are limited by stringent regulations. Three different FDA approved water-soluble polymer types were applied and compared in this study (PVA, PVP K30 and PVP K90).

Logarithm of the viscosities of the examined polymer solutions increased nearly linearly with polymer concentration because of the increasing polymer-polymer interaction and the growing number of entanglements [44–46] (Figure 1). The collected solid particles and fibrous structures were investigated by scanning electron microscopy. Figure 1 refers to

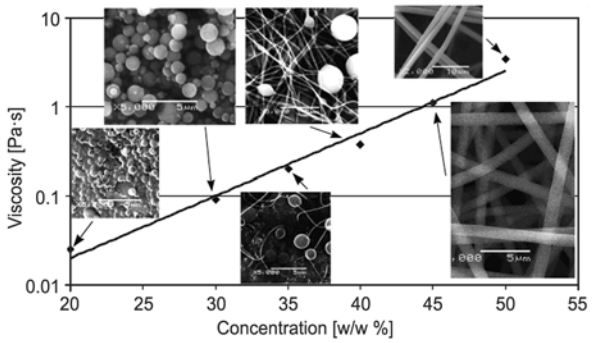

Figure 1. Viscosities of the PVP K30 of the aqueous solutions and the obtained morphology of objects electrospun from those solutions

PVP K30 showing how the morphology changed from micro- and nanoparticles through beaded fibers to nanofibers when the concentration and the viscosity of the polymer solution was varied. At lower (20–30%) polymer concentrations, electrospraying occurred typically producing submicronic. Electrospraying has also capability to encapsulate of biodrugs in a very gentle way, which is, however, out of the scope of this paper.

Beaded fibers were gained from the 35 and 40 w/w% solution of PVP K30, while at higher concentrations (45 and 50 w/w%) discrete nano- and microfibers (~400–2000 nm) were formed owing to the increased viscosity and higher entanglement of the polymer chains. Thus, 45 w/w% polymer solution was chosen for the encapsulation of bacteria in the case of PVP K30.

When the other two polymers were used, the phenomena were similar as in the case of PVP K30 (Figure 1). At lower concentrations, beaded fibers were gained and the concentrations, which were found to be optimal for getting discrete fibers with stable structure were as follows: 10 w/w% in the case of PVA and 20 w/w% in the case of PVP K90. Diameters of the formed fibers at the optimal con-

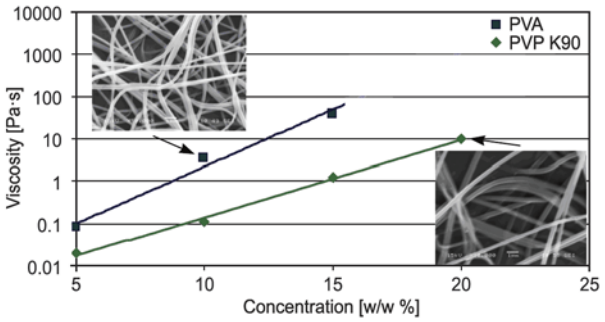

Figure 2. Viscosities of the PVA and PVP K90 aqueous solutions and the obtained morphology at the concentrations chosen for the encapsulation of bacteria

centrations were between 150 and 350 nm and 200 and 600 nm in the cases of PVA and PVP K90, respectively (Figure 2).

3.2. Encapsulation of *Lactobacillus acidophilus* into polymer nanofibers

Encapsulation of bacteria was supposed to cause a significant change in the rheological properties of the polymer solutions. Consequently, the experiments for encapsulation were started with polymer concentration at lowest concentration in order to maintain spinnability.

In contrast to the mentioned concern, the presence of bacteria in the pumped liquids containing 10 w/w% PVA and 45 w/w% PVP K30 did not cause any remarkable changes in the viscosity (increasing of viscosity was below 0.1 and 0.5%, respectively), only in the case of 20 w/w% PVP K90 was 3% difference observed. However it did not affect the fiber formation during the electrospinning process. The morphology of the LBA bacteria and their arrangement in electrospun fibers was investigated by scanning electron microscopy. Figure 3 shows the formed fibers in different magnifications. These SEM images enable us to see that the polymer fibers got thicker by encompassing rod-shaped single or interconnected bacteria. In all cases polymer coating was formed around bacteria as a result of the ES process. On the SEM images (Figures 3–6) the sizes of bacteria can be seen, which is similar to that of their original form (width: ~0.5–0.7 μm, length: ~1–3 μm) that are shown in Figure 6. These results demonstrate that all the studied pharma-polymers are capable to encapsulate LBA probiotic bacteria into water-soluble nanofibers by electrospinning technique.

Here, the concept of electrospun living bacteria solid dosage forms containing living bacteria was put forward using a single fluid electrospinning of

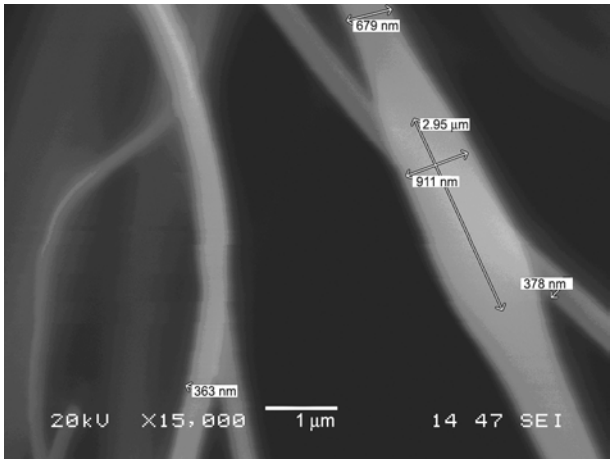

Figure 4. SEM image of LBA embedded in PVP K30 nanofibers with thickness data

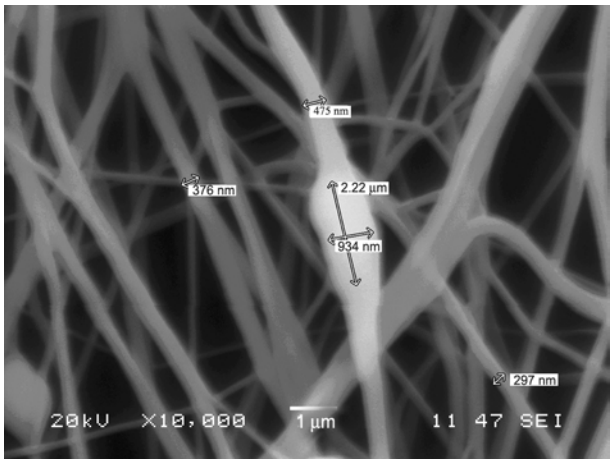

Figure 5. SEM image of LBA embedded in PVP K90 nanofibers with thickness data

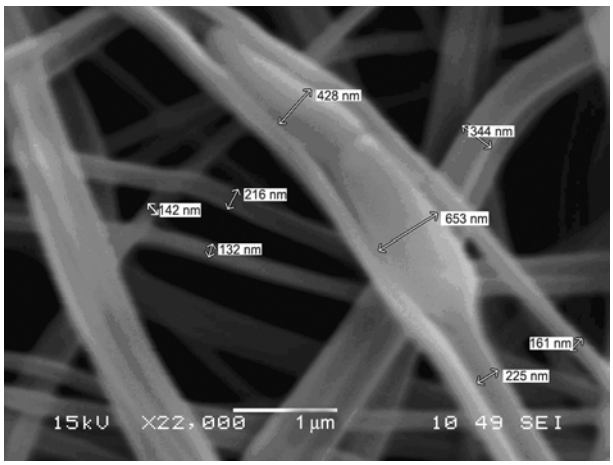

Figure 3. SEM image of LBA embedded in PVA nanofibers with thickness data

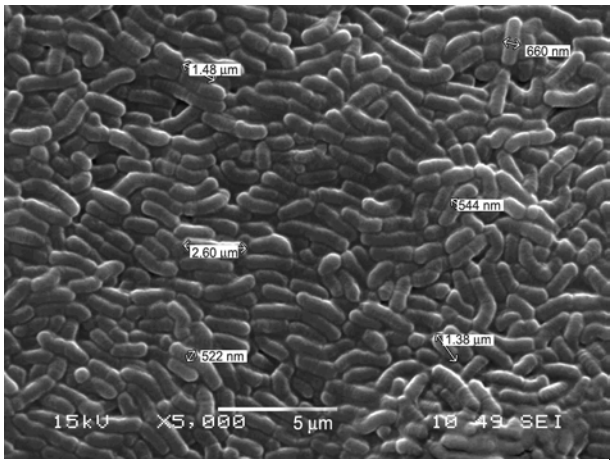

Figure 6. SEM image of the applied bacteria with thickness and length data

suspensions. Coaxial electrospinning [47–49] could further expand this concept owing to its capability to manipulate nanostructure.

3.3. Viability results

As the most important issue, from the point of view of medical application, is the biological activity of LBA the living bacteria content of the nanofibers was examined after their dissolution from nanofibers.

Measurement of CFU (colony forming unit) was performed in order to determine the effect of technology steps of the whole *ES* process on bacteria.

Immediately after electrospinning 1 g of nanofibers still contained large number of active LBA (from 8.78–9.28 log CFU) as the survival rate of the bacteria was between 34 and 68% (Table 1.), which is a remarkable result compared to efficiency of current drying processes such as freeze drying and spray drying. As Rybka and Kailasapathy [50] reported that recovery of viable *Lactobacillus acidophilus* cells after freeze drying was between 1–56% as a percentage of cells in the original solution. Besides, Riveros *et al*. [51] and Wang *et al.* [52] spray dried *Lactobacillus acidophilus* under gentle conditions (inlet temperature: 100°C, outlet temperature: 58, 60°C). Nevertheless, survival rates were only 11 and 4.9% respectively. The better survival rate in case of PVA can be explained by the oxygen excluding property of this polymer, which means that the bacteria are protected during the process [53].

Viability of LBA bacteria in polymer–containing suspensions without electrospinning process was investigated at ambient temperature as a reference. Number of CFU after 4 h decreased to 79, 72 and 70% (data are not shown) of the initial number in PVA-, PVP K30- and PVP K90–containing suspensions, respectively. This phenomenon is probably due to the lack of nutritive in the suspensions and can be avoided by adding nutrients and stabilizers to the solution.

Based on these findings electrospinning is a capable technique to produce solid dosage form of LBA in a gentle way.

Table 1. Number of active bacteria and survival rate in different types of electrospun nanowebs

	Initial solution log (CFU/g)	Electrospun biohybrid nanoweb log (CFU/g)	Survival [%]
PVA	9.45±0.03	9.28±0.03	68
PVP K30	9.12±0.04	8.65±0.04	34
PVP K90	9.18±0.03	8.78±0.04	40

3.4. Stability results

Table 2 presents the result of stability tests in case of three different of polymers. Keeping samples at ambient temperature caused the total loss of biological activity of them after a week (data are not shown). This result was predictable because marketed biopharmaceutical products containing living organism have to be stored generally at 2–8°C. The difference between the stability of samples stored at 7 and –20°C is very slight suggesting that both storage conditions are applicable and freezing is probably not necessary in most cases. Stability tests also confirmed that all of the selected polymer solutions, having no significant effect on viability of LBA, are applicable for living cell formulation. After 90 days, nanofibers still contained large amounts of LBA, which is a remarkable achievement considering the fact that there was no stabilizer of LBA present.

Table 2. Number of colony forming units per grams of electrospun nanofibers as a function of time at two temperatures

		Time [days]			
		0	7	30	90
PVA (7°C)	log(CFU/g)	9.28±0.03	8.72±0.02	8.34±0.03	7.97±0.05
	%	100	27	11	4,9
PVA (–20°C)	log(CFU/g)	9.28±0.03	8.49±0.03	8.29±0.05	8.09±0.03
	%	100	16	10	6,4
PVP K30 (7°C)	log(CFU/g)	8.65±0.04	7.94±0.06	7.55±0.04	7.07±0.04
	%	100	19	7,9	2,6
PVP K30 (–20°C)	log(CFU/g)	8.65±0.04	8.28±0.04	7.88±0.03	7.58±0.03
	%	100	42	17	8,5
PVP K90 (7°C)	log(CFU/g)	8.78±0.04	8.11±0.03	7.72±0.06	7.24±0.05
	%	100	21	8,8	2,9
PVP K90 (–20°C)	log(CFU/g)	8.78±0.04	8.35±0.05	7.95±0.03	7.64±0.04
	%	100	37	14	7.2

Applying stabilizer and packaging that excludes the oxygen would probably further improve the stability of living LBA [54].

3.5. Potential dosage forms of LBA containing biohybrid nanoweb

Industrial scaling-up of the described process seems to be achievable based on recent developments in the field of electrospinning. Several solutions for industrial-scale production of electrospun nanofibers are available and used mainly in the filtration industry [55]. Industrially performed electrospinning, equipped with transferring collector, is continuous process having very low energy consumption and high enough capacity to fabricate pharmaceutical products. As the developed electrospun BNW contain, according to the viability and stability results, high enough amounts of biologically active probiotic bacteria, several novel and existing pharmaceutical dosage forms can be designed on this basis. PVA and PVP have already been applied in vaginal formulations [56]; thus, vaginal film or electrospun biohybrid nanoweb of these polymers, containing LBA, can easily get approval from the authorities.

In order to use the new living-cell-containing solid materials for curing bacterial vaginosis, selection of administration in adequate form is also necessary. The simplest way is to apply the prepared nonwoven tissue directly after the removal from the collector and cutting into proper-sized (proper-weight) pieces. The square-cut webs can be delivered manually into the vagina (similarly to the insertion of vaginal contraceptive films called VCF), where the inserted web dissolves. For this kind of administration PVA- and PVP K90-based biohybrid nanowebs with mucoadhesive character [57, 58] are preferred and some kind of applicator (tweezers, protective gloves, etc.) needs to avoid the dissolution of web before placement. These nanofibrous tissues can be attached to a carrier film containing enhancer additives. The multilayer system, adhered to the mucosa, releases the bacteria as the polymer dissolves.

Furthermore, all kinds of nanowebs prepared in this work, dissolved instantly when they got in contact with water, and can be well exploited in stabile formulation. On Figure 7 saturation curves show that nearly the total (90%) amount of bacteria were released within one minute and there was no significant difference between the polymers due to the huge surface and to the good solubility of nanofibers.

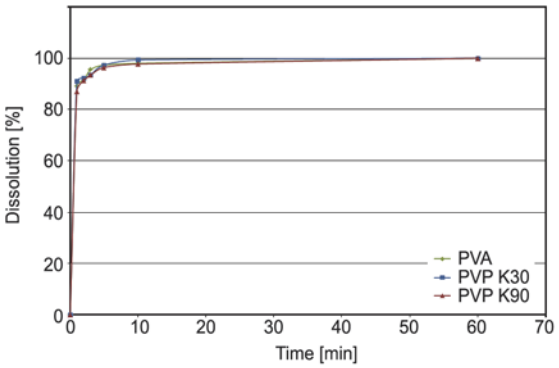

Figure 7. Release of LBA from different polymers (PVA, PVP K30, PVP K90) based BNWs

After the rapid dissolution of the solid BNW, the obtained LBA-containing liquid is administrable as a douche and can be effective against bacterial vaginosis owing to the high active probiotic content. Further enhancement of curing efficiency can be achieved by introducing appropriate excipients such as lactose, lactic acid and buffering salts, in the solvent of the web. As the nanofibrous matrix dissolves instantly when contacting with water, it can also be filled in disposable syringes together with excipients, buffering agents and enhancers which can be injected after rapid dissolution in water loaded in the syringe.

4. Conclusions

The present work shows that electrospinning is a capable way for stable solid formulation of LBA. It was found that with all the three studied polymers solutions were suitable for encapsulating huge amounts of LBA and provided long shelf life at 7 and 20°C, which can be even further extended using stabilizer excipients or applying oxygen excluding packaging. The formed nanofibrous product can be applied as an inexpensive and easy-to-use dosage form that can be recommended for the treatment of bacterial vaginosis. An adequate dose of living bacteria could be stabilized using this effective and gentle technique, which is considered to be a feasible way to produce other biopharmaceuticals as well. The dosage forms (e.g. vaginal douche) based on the developed biohybrid nanowebs are new potential way for curing bacterial vaginosis.

Acknowledgements

This project was financially supported by the New Széchenyi Development Plan (project ID: TÁMOP-4.2.1/B-09/1/KMR-2010-0002) and the Hungarian Research Fund (OTKA PD-108975, OTKA K 100949). The authors would like to express their special thanks to Richter Gedeon Talentum foundation for their generous support of István Wagner's scholarship.

References

[1] Parkins D. A., Lashmar U. T.: The formulation of biopharmaceutical products. Pharmaceutical Science and Technology Today, **3**, 129–137 (2000).
DOI: 10.1016/S1461-5347(00)00248-0

[2] Maa Y-F., Prestrelski S. J.: Biopharmaceutical powders particle formation and formulation considerations. Current Pharmaceutical Biotechnology, **1**, 283–302 (2000).
DOI: 10.2174/1389201003378898

[3] Greiner A., Wendorff J. H.: Electrospinning: A fascinating method for the preparation of ultrathin fibers. Angewandte Chemie International Edition, **46**, 5670–5703 (2007).
DOI: 10.1002/anie.200604646

[4] Liu Y. Y., Li Q. W., Hu Q. X., Jing C. J., Wang Q. G.: A new spurts controllable electrospinning collecting device designed basing on advanced motion control. Applied Mechanics and Materials, **44–47**, 1698–1702 (2011).
DOI: 10.4028/www.scientific.net/AMM.44-47.1698

[5] Lukáš D., Sarkar A., Martinová L., Vodsed'álková K., Lubasová D., Chaloupek J., Pokorný P., Mikeš P., Chvojka J., Komárek M.: Physical principles of electrospinning (electrospinning as a nano-scale technology of the twenty-first century). Textile Progress, **41**, 59–140 (2009).
DOI: 10.1080/00405160902904641

[6] Molnár K., Vas L. M., Czigány T.: Determination of tensile strength of electrospun single nanofibers through modeling tensile behavior of the nanofibrous mat. Composites Part B: Engineering, **43**, 15–21 (2012).
DOI: 10.1016/j.compositesb.2011.04.024

[7] Yu D. G., Branford-White C., White K., Chatterton N. P., Zhu L. M., Huang L. Y., Wang B.: A modified coaxial electrospinning for preparing fibers from a high concentration polymer solution. Express Polymer Letters, **5**, 732–741 (2011).
DOI: 10.3144/expresspolymlett.2011.71

[8] Košťáková E., Mészáros L., Gregr J.: Composite nanofibers produced by modified needleless electrospinning. Materials Letters, **63**, 2419–2422 (2009).
DOI: 10.1016/j.matlet.2009.08.014

[9] Rosic R., Kocbek P., Baumgartner S., Kristl J.: Electro-spun hydroxyethyl cellulose nanofibers: The relationship between structure and process. Journal of Drug Delivery Science and Technology, **21**, 229–236 (2011).

[10] Rho K. S., Jeong L., Lee G., Seo B-M., Park Y. J., Hong S-D., Roh S., Cho J. J., Park W. H., Min B-M.: Electrospinning of collagen nanofibers: Effects on the behavior of normal human keratinocytes and early-stage wound healing. Biomaterials, **27**, 1452–1461 (2006).
DOI: 10.1016/j.biomaterials.2005.08.004

[11] Huang F., Wang Q., Wei Q., Gao W., Shou H., Jiang S.: Dynamic wettability and contact angles of poly(vinylidene fluoride) nanofiber membranes grafted with acrylic acid. Express Polymer Letters, **4**, 551–558 (2010).
DOI: 10.3144/expresspolymlett.2010.69

[12] Sun K., Li Z. H.: Preparations, properties and applications of chitosan based nanofibers fabricated by electrospinning. Express Polymer Letters, **5**, 342–361 (2011).
DOI: 10.3144/expresspolymlett.2011.34

[13] Rampichová M., Martinová L., Košťáková E., Filová E., Míčková A., Buzgo M., Michálek J., Přádný M., Nečas A., Lukáš D., Amler E.: A simple drug anchoring microfiber scaffold for chondrocyte seeding and proliferation. Journal of Materials Science: Materials in Medicine, **1**, 555–563 (2012).
DOI: 10.1007/s10856-011-4518-x

[14] Verreck G., Chun I., Peeters J., Rosenblatt J., Brewster M. E.: Preparation and characterization of nanofibers containing amorphous drug dispersions generated by electrostatic spinning. Pharmaceutical Research, **20**, 810–817 (2003).
DOI: 10.1023/A:1023450006281

[15] Yu D-G., Liu F., Cui L., Liu Z-P., Wang X., Bligh S. W. A.: Coaxial electrospinning using a concentric Teflon spinneret to prepare biphasic-release nanofibers of helicid. RSC Advances, **3**, 17775–17783 (2013).
DOI: 10.1039/C3RA43222J

[16] Yu D-G, Branford-White C., White K., Li X-L., Zhu L-M.: Dissolution improvement of electrospun nanofiber-based solid dispersions for acetaminophen. AAPS PharmSciTech, **11**, 809–817 (2010).
DOI: 10.1208/s12249-010-9438-4

[17] Nagy Zs. K., Nyúl K., Wagner I., Molnár K., Marosi Gy.: Electrospun water soluble polymer mat for ultrafast release of Donepezil HCl. Express Polymer Letters, **4**, 763–772 (2010).
DOI: 10.3144/expresspolymlett.2010.92

[18] Yu D-G., Yu J-H., Chen L., Williams G. R., Wang X.: Modified coaxial electrospinning for the preparation of high-quality ketoprofen-loaded cellulose acetate nanofibers. Carbohydrate Polymers, **90**, 1016–1023 (2012).
DOI: 10.1016/j.carbpol.2012.06.036

[19] Nagy Zs. K., Balogh A., Vajna B., Farkas A., Patyi G., Kramarics Á., Marosi Gy.: Comparison of electrospun and extruded soluplus®-based solid dosage forms of improved dissolution. Journal of Pharmaceutical Sciences, **101**, 322–332 (2011).
DOI: 10.1002/jps.22731

[20] Liu Y., Rafailovich M. H., Malal R., Cohn D., Chidambaram D.: Engineering of bio-hybrid materials by electrospinning polymer-microbe fibers. Proceedings of the National Academy of Sciences, **106**, 14201–14206 (2009).
DOI: 10.1073/pnas.0903238106

[21] Klein S., Kuhn J., Avrahami R., Tarre S., Beliavski M., Green M., Green M., Zussman E.: Encapsulation of bacterial cells in electrospun microtubes. Biomacromolecules, **10**, 1751–1756 (2009).
DOI: 10.1021/bm900168v

[22] Gensheimer M., Becker M., Brandis-Heep A., Wendorff J. H., Thauer R. K., Greiner A.: Novel biohybrid materials by electrospinning: Nanofibers of poly(ethylene oxide) and living bacteria. Advanced Materials, **19**, 2480–2482 (2007).
DOI: 10.1002/adma.200602936

[23] Zussman E.: Encapsulation of cells within electrospun fibers. Polymers for Advanced Technologies, **22**, 366–371 (2011).
DOI: 10.1002/pat.1812

[24] Salalha W., Kuhn J., Dror Y., Zussman E.: Encapsulation of bacteria and viruses in electrospun nanofibres. Nanotechnology, **17**, 4675–4681 (2006).
DOI: 10.1088/0957-4484/17/18/025

[25] López-Rubio A., Sanchez E., Sanz Y., Lagaron J. M.: Encapsulation of living bifidobacteria in ultrathin PVOH electrospun fibers. Biomacromolecules, **10**, 2823–2829 (2009).
DOI: 10.1021/bm900660b

[26] López-Rubio A., Sanchez E., Wilkanowicz S., Sanz Y., Lagaron J. M.: Electrospinning as a useful technique for the encapsulation of living bifidobacteria in food hydrocolloids. Food Hydrocolloids, **28**, 159–167 (2012).
DOI: 10.1016/j.foodhyd.2011.12.008

[27] Heunis T. D. J., Botes M., Dicks L. M. T.: Encapsulation of *Lactobacillus plantarum* 423 and its bacteriocin in nanofibers. Probiotics and Antimicrobial Proteins, **2**, 46–51 (2010).
DOI: 10.1007/s12602-009-9024-9

[28] Fung W-Y., Yuen K-H., Liong M-T.: Agrowaste-based nanofibers as a probiotic encapsulant: Fabrication and characterization. Journal of Agricultural and Food Chemistry, **59**, 8140–8147 (2011).
DOI: 10.1021/jf2009342

[29] Cannon J., Lee T., Bolanos J., Danziger L.: Pathogenic relevance of *Lactobacillus:* A retrospective review of over 200 cases. European Journal of Clinical Microbiology and Infectious Diseases, **24**, 31–40 (2005).
DOI: 10.1007/s10096-004-1253-y

[30] Madigan M. T.: Prokaryotic diversity: The bacteria. in 'Brock biology of microorganisms' (eds: Madigan M. T., Martinko J. M., Stahl D., Clark D. P.) Prentice Hall, Upper Saddle River, USA' 329–418 (2006).

[31] Castellano Filho D. S., Diniz C. G., Silva V. L.: Bacterial vaginosis: Clinical, epidemiologic and microbiological features. HU Revista, **36**, 223–230 (2010).

[32] Mastromarino P., Macchia S., Meggiorini L., Trinchieri V., Mosca L., Perluigi M., Midulla C.: Effectiveness of *Lactobacillus*-containing vaginal tablets in the treatment of symptomatic bacterial vaginosis. Clinical Microbiology and Infection, **15**, 67–74 (2009).
DOI: 10.1111/j.1469-0691.2008.02112.x

[33] Allsworth J. E., Peipert J. F.: Prevalence of bacterial vaginosis: 2001–2004 national health and nutrition examination survey data. Obstetrics and Gynecology, **109**, 114–120 (2007).
DOI: 10.1097/01.AOG.0000247627.84791.91

[34] McLean N. W., McGroarty J. A.: Growth inhibition of metronidazole-susceptible and metronidazole-resistant strains of *Gardnerella vaginalis* by *Lactobacilli in vitro*. Applied and Environmental Microbiology, **62**, 1089–1092 (1996).

[35] Simoes J. A., Aroutcheva A., Heimler I., Shott S., Faro S.: Bacteriocin susceptibility of *Gardnerella vaginalis* and its relationship to biotype, genotype, and metronidazole susceptibility. American Journal of Obstetrics and Gynecology, **185**, 1186–1190 (2001).
DOI: 10.1067/mob.2001.118144

[36] Falagas M. E., Betsi G. I., Athanasiou S.: Probiotics for the treatment of women with bacterial vaginosis. Clinical Microbiology and Infection, **13**, 657–664 (2007).
DOI: 10.1111/j.1469-0691.2007.01688.x

[37] Hallén A., Jarstrand C., Påhlson C.: Treatment of bacterial vaginosis with *Lactobacilli*. Sexually Transmitted Diseases, **19**, 146–148 (1992).

[38] Chimura T., Funayama T., Murayama K., Numazaki M.: Ecological treatment of bacterial vaginosis. The Japanese Journal of Antibiotics, **48**, 432–436 (1995).

[39] Parent D., Bossens M., Bayot D., Kirkpatrick C., Graf F., Wilkinson F. E., Kaiser R. R.: Therapy of bacterial vaginosis using exogenously-applied *Lactobacilli acidophili* and a low dose of estriol: A placebo-controlled multicentric clinical trial. Arzneimittelforschung, **46**, 68–73 (1996).

[40] Neri A., Sabah G., Samra Z.: Bacterial vaginosis in pregnancy treated with yoghurt. Acta Obstetricia et Gynecologica Scandinavica, **72**, 17–19 (1993).
DOI: 10.3109/00016349309013342

[41] MacPhee R. A., Hummelen R., Bisanz J. E., Miller W. L., Reid G.: Probiotic strategies for the treatment and prevention of bacterial vaginosis. Expert Opinion on Pharmacotherapy, **11**, 2985–2995 (2010).
DOI: 10.1517/14656566.2010.512004

[42] Persano L., Camposeo A., Tekmen C., Pisignano D.: Industrial upscaling of electrospinning and applications of polymer nanofibers: A review. Macromolecular Materials and Engineering, **298**, 504–520 (2013).
DOI: 10.1002/mame.201200290

[43] Park S. J., Park S-H., Cho S., Kim D-M., Lee Y., Ko S. Y., Hong Y., Choy H. E., Min J-J., Park J-O., Park S.: New paradigm for tumor theranostic methodology using bacteria-based microrobot. Scientific Reports, **3**, 3394/1–3394/8 (2013).
DOI: 10.1038/srep03394

[44] Shenoy S. L., Bates W. D., Frisch H. L., Wnek G. E.: Role of chain entanglements on fiber formation during electrospinning of polymer solutions: Good solvent, non-specific polymer–polymer interaction limit. Polymer, **46**, 3372–3384 (2005).
DOI: 10.1016/j.polymer.2005.03.011

[45] Zeng J., Haoqing H., Schaper A., Wandorff J. H., Greiner A.: Poly-L-lactide nanofibers by electrospinning – Influence of solution viscosity and electrical conductivity on fiber diameter and fiber morphology. e-Polymers, no.009 (2005).

[46] Beachley V., Wen X.: Effect of electrospinning parameters on the nanofiber diameter and length. Materials Science and Engineering: C, **29**, 663–668 (2009).
DOI: 10.1016/j.msec.2008.10.037

[47] Yu D. G., Wang X., Li X. Y., Chian W., Li Y., Liao Y. Z.: Electrospun biphasic drug release polyvinylpyrrolidone/ethyl cellulose core/sheath nanofibers. Acta Biomaterialia, **9**, 5665–5672 (2012).
DOI: 10.1016/j.actbio.2012.10.021

[48] Yu D-G., Williams G. R., Wang X., Liu X-K., Li H-L., Bligh S. W. A.: Dual drug release nanocomposites prepared using a combination of electrospraying and electrospinning. RSC Advances, **3**, 4652–4658 (2013).
DOI: 10.1039/C3RA40334C

[49] Yu D-G., Li X-Y., Wang X., Chian W., Liao Y-Z., Li Y.: Zero-order drug release cellulose acetate nanofibers prepared using coaxial electrospinning. Cellulose, **20**, 379–389 (2013).
DOI: 10.1007/s10570-012-9824-z

[50] Rybka S., Kailasapathy K.: The survival of culture bacteria in fresh and freeze-dried AB yoghurts. Australian Journal of Dairy Technology, **50**, 51–57 (1995).

[51] Riveros B., Ferrer J., Bórquez R.: Spray drying of a vaginal probiotic strain of *Lactobacillus acidophilus*. Drying Technology, **27**, 123–132 (2009).
DOI: 10.1080/07373930802566002

[52] Wang Y-C., Yu R-C., Chou C-C.: Viability of lactic acid bacteria and bifidobacteria in fermented soymilk after drying, subsequent rehydration and storage. International Journal of Food Microbiology, **93**, 209–217 (2004).
DOI: 10.1016/j.ijfoodmicro.2003.12.001

[53] Miller K. S., Krochta J. M.: Oxygen and aroma barrier properties of edible films: A review. Trends in Food Science and Technology, **8**, 228-237 (1997).
DOI: 10.1016/S0924-2244(97)01051-0

[54] Morgan C. A., Herman N., White P. A., Vesey G.: Preservation of micro-organisms by drying; A review. Journal of Microbiological Methods, **66**, 183–193 (2006).
DOI: 10.1016/j.mimet.2006.02.017

[55] Zhou F-L., Gong R-H., Porat I.: Mass production of nanofibre assemblies by electrostatic spinning. Polymer International, **58**, 331–342 (2009).
DOI: 10.1002/pi.2521

[56] Garg S., Tambwekar K. R., Vermani K., Garg A., Kaul C. L., Zaneveld L. J. D.: Compendium of pharmaceutical excipients for vaginal formulations. Pharmaceutical Technology, **25**, 14–25 (2001).

[57] Perioli L., Ambrogi V., Angelici F., Ricci M., Giovagnoli S., Capuccella M., Rossi C.: Development of mucoadhesive patches for buccal administration of ibuprofen. Journal of Controlled Release, **99**, 73–82 (2004).
DOI: 10.1016/j.jconrel.2004.06.005

[58] Peppas N. A., Mongia N. K.: Ultrapure poly(vinyl alcohol) hydrogels with mucoadhesive drug delivery characteristics. European Journal of Pharmaceutics and Biopharmaceutics, **43**, 51–58 (1997).
DOI: 10.1016/S0939-6411(96)00010-0

eXPRESS Polymer Letters Vol.8, No.5 (2014) 362–372
Available online at www.expresspolymlett.com
DOI: 10.3144/expresspolymlett.2014.40

Dispersing hydrophilic nanoparticles in hydrophobic polymers: HDPE/ZnO nanocomposites by a novel template-based approach

M. Salzano de Luna[1], *M. Galizia*[1], *J. Wojnarowicz*[2], *R. Rosa*[3], *W. Lojkowski*[2], *C. Leonelli*[3], *D. Acierno*[1], *G. Filippone*[1*]

[1]Dipartimento di Ingegneria Chimica, dei Materiali e della Produzione Industriale, Università di Napoli Federico II, Piazzale Tecchio 80, 80125 Naples, Italy
[2]Institute of High Pressure Physics, Polish Academy of Sciences, ul. Sokolowska 29/37 01-142 Warsaw, Poland
[3]Dipartimento di Ingegneria 'Enzo Ferrari', Università di Modena e Reggio Emilia, Via Vignolese 905/A, 41125 Modena, Italy

Received 3 November 2013; accepted in revised form 29 December 2013

Abstract. The efficiency of a novel template-based approach for the dispersion of hydrophilic nanoparticles within hydrophobic polymer matrices is investigated. The procedure envisages the permeation of a well dispersed nanoparticle suspension inside a micro-porous matrix, obtained through selective extraction of a sacrificial phase from a finely interpenetrated co-continuous polymer blend. Specifically, a blend of high density polyethylene (HDPE) and polyethylene oxide (PEO) at 50/50 wt% is prepared by melt mixing. The addition of small amounts of organo-clay promotes the necessary refinement of the blend morphology. Once removed the PEO, the micro-porous HDPE matrix is dipped in a colloidal suspension of zinc oxide nanoparticles which exhibits low interfacial tension with HDPE. A system prepared by traditional melt mixing is used as reference. Melt- and solid-state viscoelastic measurements reveal a good quality of the filler dispersion despite the uneven distribution on micro-scale. The latter can be capitalized to minimize the filler content to attain a certain improvement of the material properties or to design nano-structured polymer composites.

Keywords: *nanocomposites, ZnO nanoparticles, filler dispersion, polymer blends, templates*

1. Introduction

Polymer nanocomposites (PNCs) based on inorganic nanoparticles (INPs) are a well-established field of research due to the interesting properties arising from such class of filler. In particular, besides improved mechanical, thermal and barrier properties, the control of the chemistry of INPs may provide new functionalities to the host matrix, allowing for the enlarging of the fields of application of polymeric materials in sectors such as automotive, micro-optics, micro-electronics, environment, health, energy and housing [1]. The use of nanoparticles as filler for polymer matrices generally implies relevant problems in terms of dispersability [2]. INPs usually present hydrophilic characteristics, which bring about substantial differences in terms of surface energy between the polymer matrix and the filler, leading to phase segregation. In addition, the high surface-to-volume ratio of nanoparticles typically results in small inter-particle distances, which makes van der Waals and electrostatic forces of major importance [3]. As a consequence, nanoparti-

*Corresponding author, e-mail: gfilippo@unina.it

cles are inclined to form agglomerates which can be extremely difficult to break up into individual species and to disperse uniformly inside the polymer matrix. The presence of such agglomerates impedes the efficient transfer of the beneficial properties of the filler related to its nanoscopic dimension to the host polymer, leading to 'nanofilled materials' with properties comparable to traditional microcomposites [4].

In the light of previous considerations, it is clear that controlling the dispersion of nanoparticles inside polymer matrices is crucial to fully exploit the potential of polymer nanocomposites. In this sense, the using of suitable compounding technique is strictly required [5]. Various approaches have been proposed to manufacture well dispersed INP-based polymer nanocomposites. Chemical modification of the nanoparticle surface, polymer-particle compatibilizing agents, in situ INP synthesis and/or polymerization are examples of possible strategies which have revealed to be effective in attaining a homogeneous filler dispersion [6–8]. However, the compounding approach for the large scale production of PNCs typically involve unmodified nanoparticles which are directly incorporated in the polymer matrix, either in the melt or in solution. Melt mixing is the most time- and cost-effective technique, but it requires that the filler is used in powder form. Although produced in the nm-range and with a narrow size distribution, such kind of dry nanoparticles have the tendency to fuse together forming stable aggregates, suffering from further agglomeration during handling and/or storage [9]. The immediate advantage offered by solution mixing is a better filler dispersion [10]. In this case the nanoparticles are in the form of colloidal dispersion, in which almost exclusively isolated primary particles are present. The major con of solution mixing is that it requires that the polymer matrix is dissolved in the same solvent of nanoparticles or in a medium soluble with them. Unless often unaffordable chemical modifications of the particle surface are made, the feasibility of solution mixing is hence limited to suitable polymer-particle pairs, and to polymers which are soluble in solvents of common use, thereby excluding, for example, polyolefins.

In the present work we deal with the challenging task of dispersing hydrophilic nanoparticles in a hydrophobic matrix. In particular, PNCs based on high density polyethylene (HDPE) filled with zinc oxide (ZnO) nanoparticles are prepared by means of a novel template-based approach, which capitalizes the high degree of filler dispersion of solution techniques eluding the issues related to the needing of specific solvents for the polymer. The ability of the proposed strategy to effectively entrap hydrophilic nanoparticles in a hydrophobic polymer matrix is the result of a judicial selection of the materials and compounding procedures. The state of dispersion and distribution of the filler is compared to that of PNCs prepared by conventional melt mixing.

2. Experimental

2.1. Materials

The polymers are high density polyethylene (HDPE, code 427985, Sigma-Aldrich, Milan, Italy) with melt flow index $MFI_{190°C/2.16\,kg}$ =12 g·min^{-1} and poly (ethyleneoxide) (PEO, code 181986, Sigma-Aldrich, Italy) with molecular weight M_v = 100 kDa.

A montmorillonite organo-modified with dimethyl dihydrogenatedtallow quaternary ammonium salt (Cloisite® C15A, Southern Clay Products, Gonzales, Texas, USA) was used to refine the morphology of the polymer blends. C15A has an organic content of ~43% and a mass density of 1.66 g·cm^{-3}.

Unfunctionalized, almost spherical zinc oxide nanoparticles were produced in the form of dry powder by microwave-assisted synthesis [11], with average dimension of the primary particles of 32 nm, specific surface area of ~36 m^2·g^{-1} (BET method) and mass density of 5.21 g·cm^{-3}.

Two colloidal suspensions of zinc oxide nanoparticles were purchased from Sigma Aldrich: a water-based dispersion of particle of size <100 nm (50 wt% of ZnO, code 721077) and a dispersion of particle of size <110 nm in butyl acetate (40 wt% of ZnO, code 721093).

2.2. Nanocomposite preparation

Two series of nanocomposites at different filler content were prepared using different compounding procedures. The samples classified as 'MM' were prepared by a two-step melt mixing route. Specifically, a masterbatch of HDPE at high content of dry ZnO nanoparticles (particle weight percentage Φ_{ZnO} ~7 wt%) was prepared using a co-rotating conical twin-screw micro-compounder (Xplore, DSM). The resulting sample was then diluted by melt mixing with neat HDPE to adjust the composition. The extrusions were all performed at 150°C in

nitrogen atmosphere at a screw speed of 200 rpm, corresponding to average shear rates of ~75 s^{-1}. Finally, the specimens for the subsequent analyses were obtained by compression molding for 3 minutes at 150°C under a pressure of ~100 bar. The unfilled HDPE used as reference material was processed in the same conditions.

The second class of samples, classified as 'TB' (template-based), was prepared by a novel approach in which a polymer scaffold is used as template. The basic steps are sketched in Figure 1. First, a HDPE/PEO blend (50/50 wt%) filled with C15A (Φ_{C15A} ~1.5 wt%) was prepared by melt mixing at 150°C in nitrogen atmosphere ad at a screw speed of 100 rpm, corresponding to average shear rates of ~50 s^{-1} (step a) in Figure 1. The constituents, dried overnight under vacuum at 50°C, were simultaneously loaded and melt compounded in the extruder. Disk-shaped specimens were obtained by compression-molding at 150°C for 3 minutes under a pressure of ~100 bar. Then, the disks were immersed in deionized water for approximately 3 weeks under stirring to extract the PEO phase from the samples (step b). The two as-received dispersions of ZnO nanoparticles in water and butyl acetate were diluted with pure solvents until reaching a filler concentration of ~4 wt%. Then, the extracted, PEO-free disks were dipped in the dispersions under stirring to allow the ZnO to penetrate inside the microporous HDPE scaffolds (step c). After 2 weeks the samples were collected and dried under vacuum until a constant weight was reached. The TB approach led to porous samples, which were finally compacted at 150°C in a vacuum oven under low pressures (~0.1 bar) to obtain dense samples (step d).

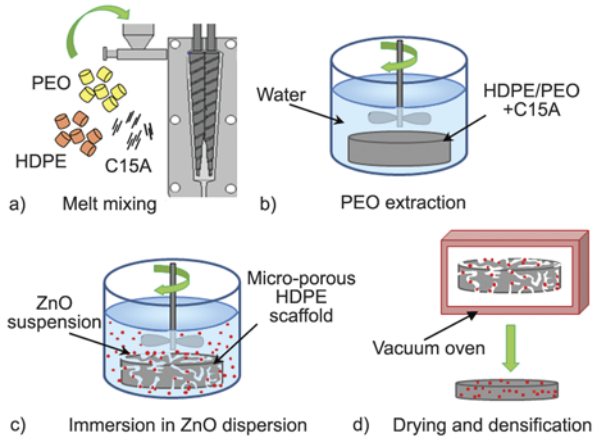

Figure 1. Schematic of the basic steps of the template-based approach for the preparation of the HDPE/ZnO nanocomposites

HDPE-based nanocomposites filled with C15A (Φ_{C15A} ~1.5 wt%) and with the same amount of ZnO nanoparticles as those obtained by the TB approach were prepared by simple melt mixing and used as reference to assess the effectiveness of our compounding technique.

2.3. Characterization

Differential scanning calorimetry was performed under nitrogen flow using a Q20 DSC apparatus (TA Instruments). The samples were first heated from room temperature up to 170°C, then cooled down to 25°C, and finally heated again. Each step was performed at a rate of 10°C min^{-1}. The crystallization temperature (T_c), onset ($T_{m,onset}$) and peak melting temperatures ($T_{m,peak}$) and melting enthalpy (ΔH_f) were recorded. The degree of crystallinity (χ_c) of the HDPE samples was obtained by dividing the ΔH_f of the first heating scan by the melting enthalpy of a 100% pure crystalline HDPE sample, taken as 293.1 $J \cdot g^{-1}$ [12].

The tensile properties were estimated at room temperature and humidity using an Instron machine according to ASTM test method D882. The specimens were cut from compression-molded sheets. The samples, stored at room temperature and humidity, were tested at 25 $mm \cdot min^{-1}$ up to a strain of 2%, then the speed was increased up to 50 $mm \cdot min^{-1}$ until break. The Young's modulus (E), tensile strength (σ_{max}) and elongation at break (ε_{break}) were recorded. The data reported are average values obtained by analyzing the results of eight tests per sample.

The permeability to oxygen (P_{O_2}) and carbon dioxide (P_{CO_2}) were measured at 30°C and atmospheric pressure using a constant volume-variable pressure apparatus.

Thermogravimetric analyses were performed using a Q5000 TGA apparatus (TA Instruments). The samples were heated up to 700°C at 10°C·min^{-1} in nitrogen atmosphere. The actual content of filler in the PNCs was estimated as the residual weight at T = 700°C. Note that for the TB samples the actual content of filler was determined after each step of Figure 1.

The microstructure of the neat and filled HDPE/PEO blends was investigated through scanning electron microscopy (FE-SEM, Ultraplus by Zeiss). The samples were cracked in liquid nitrogen and

the fracture surfaces were observed. Energy dispersive spectroscopy (EDS, Aztec by Oxford Instruments) was used to infer the presence of the ZnO nanoparticles in the samples obtained by TB approach and to investigate the distribution of the filler on micro-scale.

The static contact angle (θ) of water and butyl acetate on HDPE films surface was estimated with an automatic video-based measurement of contact angle performed at room temperature and humidity by using a Theta contact angle T200-Auto (KSV/Attension, Helsinki). Five μL of liquid were placed over the HDPE surface and the Young/Laplace method was used to calculate the static contact angle. Five independent measurements were performed for each liquid.

A stress-controlled rotational rheometer (AR-G2, TA Instruments) in parallel-plate geometry (diameter 25 mm) was used for the rheological analyses. Oscillatory tests were performed at $T = 180$°C in a dry nitrogen atmosphere. Specifically, low-frequency (10^{-1} rad/s) time-sweep experiments were carried out first. After the reaching of the steady state, the elastic (G') and viscous (G'') shear moduli were measured as a function of mechanical frequency (ω) in the linear regime, which was previously evaluated for each composition through strain amplitude tests.

Dynamic mechanical analyses were carried out using a Tritec 2000 DMA apparatus (Triton Technology Ltd., Grantham). The elastic (E') and viscous (E'') flexural moduli were measured as function of temperature in single-cantilever bending mode at a frequency of 1 Hz and with a total displacement of 0.02 mm, which is small enough to be in the linear regime. The sample bars ($10\times20\times1$ mm^3) were heated at 2°C·min^{-1} from room temperature.

3. Results and discussion

3.1. Melt mixing route

First of all, the impact of dry ZnO nanoparticles on technologically relevant properties of HDPE/ZnO nanocomposites prepared by a traditional melt mixing route has been investigated. Dispersing metal oxide nanoparticles in polymer media is a difficult task because of the large specific surface area of the filler and the incompatibility in surface characteristics with the matrix. Simply compounding polymer and dry nanopowders by melt mixing routes is often inadequate, although the high shear and elongational stresses during extrusion could break the clusters of primary nanoparticles reducing their average size. The minimum size of the aggregates depends on the applied stress and the composite Hamaker constant for two surfaces interacting through a medium [13], being in any case much larger than the size of the single nanoparticle. A SEM micrograph of our dry ZnO nanoparticles is shown in Figure 2a, whereas a typical micron-sized aggregate suspended in the HDPE matrix of a MM sample is reported in Figure 2b.

The negligible polymer-particle enthalpic interactions and the aggregated state of the filler are expected to not appreciably affect the macroscopic

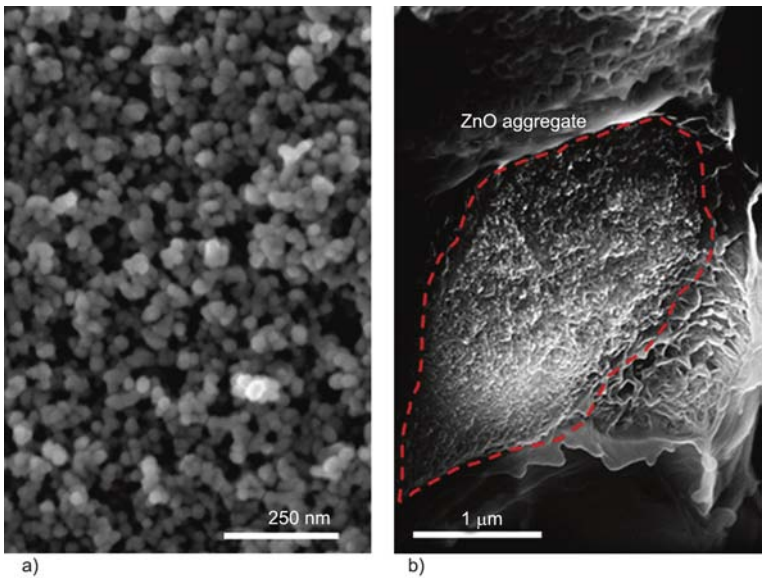

Figure 2. SEM micrographs showing (a) as-synthesized ZnO dry nanoparticles and (b) a detail of particle aggregate protruding from the fracture surface of a MM nanocomposite

properties of the MM samples. First, possible effects of the particles on the crystalline structure of the host polymer have been investigated through DSC measurements. As summarized in Table 1, whatever the content of ZnO nanoparticles is, the melting and crystallization behaviors remain almost constant. In addition, no evident changes are detected for the crystallinity, the samples sharing comparably high values of χ_c (~50%).

Other technologically relevant properties of PNCs particularly sensitive to the state of dispersion of nanoparticles are mechanical and barrier properties. The results of the tensile and permeability tests are reported in Figure 3 as a function of filler content.

Neither E nor σ_{max} appreciably change with respect to the unfilled matrix, whereas a drastic decrease of ε_{break} occurs with increasing Φ_{ZnO}. The detrimental effect on the elongation at break noticed in the presence of the filler is due to the presence of nanoparticle aggregates, which are sites where cracks initiate on and significantly lowering the ultimate properties of the material [14]. The barrier properties are also negligibly affected by the aggregated filler. The P_{O_2} and P_{CO_2} of our MM nanocomposites indeed slightly increase upon addition of ZnO nanoparticles, probably due to the scarce polymer-particle interfacial adhesion which enhances the overall free volume of the MM samples. Actually, scarce improvements in the mechanical and barrier properties of ZnO-filled nanocomposites have been reported even in case of good dispersion of the filler due to the low aspect ratio of the nanoparticles [15]. A more conclusive insight on the state of dispersion of the filler can be obtained through rheological measurements. In particular, linear viscoelastic analysis is an extremely sensitive tool to probe the material structure over various length scales, offering an integrated picture of composite samples with higher reliability of the results compared to other methods, based on the analysis of the mechanical and barrier properties, which are too sensitive to micron-scale inhomogeneity [16]. The time evolution of G' at $\omega = 10^{-1}$ rad/s and the frequency-dependent moduli of neat polymer and nanocomposites at different filler content are shown in Figure 4.

Nanoparticles, either isolated or in the form of aggregates, may experience relevant Brownian motions in polymer melts provided that they are sufficiently small. Driven by particle-particle attraction, the filler flocculate in timescales which scale with the cubic power of the size of the aggregates [17]. Such structural rearrangements, if any, cause an enhancement of the elastic connotation during time, which eventually alters the relaxation spectrum in a characteristic way: both G' and G'' significantly increase at low frequency, the effect being more pronounced on the elastic component. It is important to observe that noticeable alterations are expected even for very low filler contents and poor polymer-particle affinity [18]. None of the rheological peculiarities of PNCs can be recognized in the MM, not even at relatively high ZnO contents. The behavior is rather reminiscent of that of conventional micro-compos-

Table 1. Onset and peak melting temperatures, crystallization temperature and crystallinity of neat HDPE and melt mixed nanocomposites

Φ_{ZnO} [wt%]	$T_{m,onset}$ [°C]	$T_{m,peak}$ [°C]	T_c [°C]	χ_c [%]
0.0	123.5	128.8	115.3	54.5
~1.5	122.3	128.5	116.0	54.3
~3.0	123.6	128.9	116.7	53.4
~4.5	122.7	128.7	116.6	52.5
~6.0	123.8	128.7	116.4	52.7

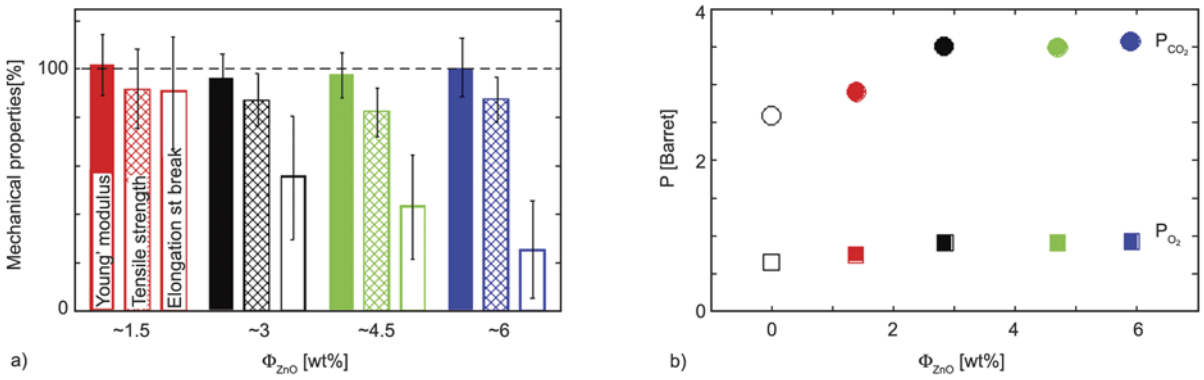

Figure 3. (a) Mechanical properties of the melt mixed PNCs at different Φ_{ZnO}: Young's modulus, tensile strength and elongation at break. The values are normalized with respect to the neat matrix. (b) Barrier properties of the melt mixed PNCs at different Φ_{ZnO}: permeability to oxygen (squares) and carbon dioxide (circles).

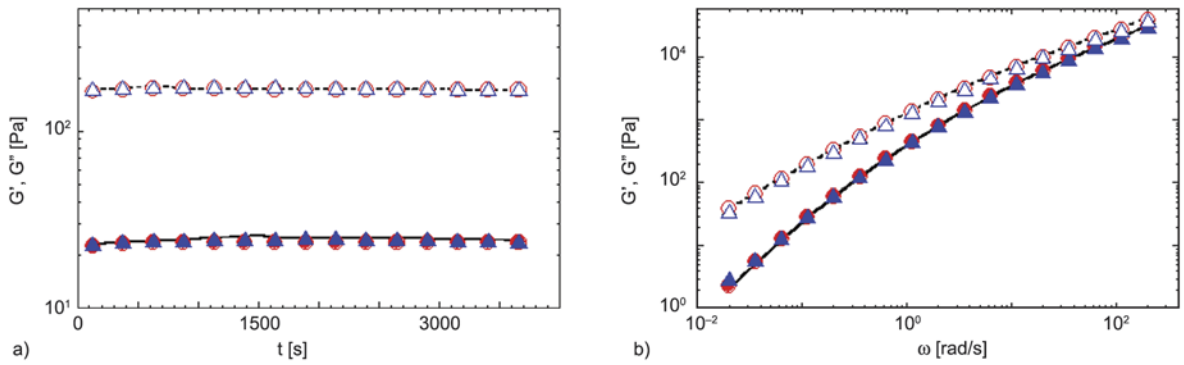

Figure 4. (a) Time evolution and (b) frequency-dependence of G' (full symbols) and G'' (empty symbols) of the PNCs at Φ_{ZnO} ~1.5 wt% (red circles) and ~6 wt% (blue triangles). Solid and dashed black lines represent G' and G'', respectively, of neat HDPE.

ites at low filler volume fractions, in which the particles are too big to move and rearrange in the melt and the volume of polymer perturbed by the filler is not sufficient to affect the overall relaxation spectrum [19, 20].

Although being a widespread route to distribute and disperse nanoparticles in the form of dry powders within polymer matrices, unless using targeted processing expedients, melt compounding is often inadequate in case of systems with very low polymer-particle affinity, such as the HDPE/ZnO nanocomposites considered here. Aim of the next section is assessing the effectiveness of an alternative compounding method, which exploits the advantages of solution techniques eluding the issues related to the needing of specific solvents.

3.2. Template-based approach

The underlying idea of the proposed TB method is to make a dispersion of well dispersed ZnO nanoparticles to penetrate inside a microporous HDPE scaffold obtained by selective extraction of a sacrificial PEO phase blended with the HDPE. A prerequisite is that the starting HDPE/PEO blend exhibits a co-continuous morphology, in which PEO forms a space-spanning framework that interpenetrates the HDPE. A blend composition of 50/50 wt%/wt% has been selected for this purpose.

Once the PEO has been extracted, the remaining HDPE scaffold is dipped in a stable dispersion of isolated ZnO nanoparticles, which will hopefully remain trapped inside the polymer. In order to optimize the process, the HDPE scaffold should contain a thick network of tiny channels, i.e. the starting HDPE/PEO blend should exhibit a microstructure as fine as possible. In such a way, the trapped nanoparticles will finely distribute inside the host matrix. On the other hand, the penetration depth of the ZnO suspension inside the channels, which inversely scales with their diameter, must be preserved to ensure a homogeneous distribution along the sample thickness. Conciliating these two opposite requisites is a challenging task, which we have addressed through a judicial selection of the materials.

Adding plate-like nanoparticles to a polymer blend is a clever expedient to promote and stabilize fine co-continuous morphologies in immiscible polymer blends. Basing on recent results by our group, small amounts of C15A were used to refine the morphology of our blends [21]. The SEM micrographs showing the impact of the filler are reported in Figure 5. C15A induces a drastic downsizing of the polymer phases, and the HDPE scaffold remaining after the removal of PEO exhibits an irregular porous microstructure much finer than that of the unfilled sample.

Besides refining the morphology, the penetration of the suspension of ZnO nanoparticles inside the channels of the HDPE scaffold has to be ensured. For this purpose, wettability arguments are invoked. A good affinity between the liquid phase of the suspension and the polymer scaffold is required. The penetrating power of a liquid is equal to the distance which the liquid will penetrate a capillary tube of unit radius in unit time, when flowing under its own capillary pressure. Such a 'penetrativity' is also a function of the nature of the material composing the capillary and the liquid itself, being proportional to $\cos\theta$, where θ represents the contact angle [22]. To verify the relevance of the nature of the liquid medium, two different ZnO dispersions, one in water and the other in butyl acetate, have

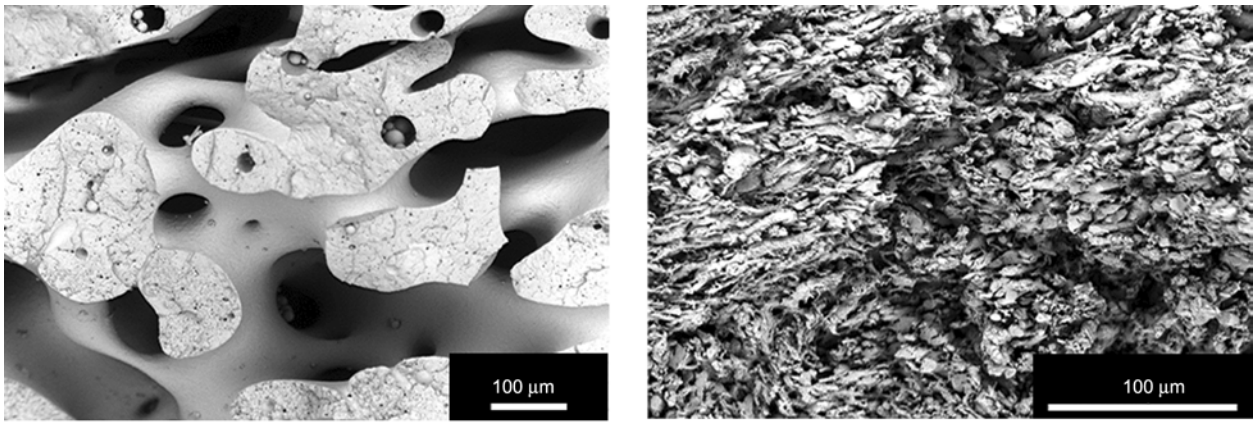

Figure 5. SEM micrographs of (a) the neat HDPE/PEO blend and (b) the blend filled with Φ_{C15A} ~1.5 wt%. For clarity, the cryo-fractured surfaces have been dipped in water to selectively remove the PEO phase.

been employed. The wettability of HDPE by the two liquids has been estimated by contact angle measurements, whose results are summarized in Table 2 (see also Figure 6).

The water contact angle is greater than 90°, hence water cannot penetrate inside the pores of the HDPE scaffold by capillary action. In contrast, the value of θ <<90° of butyl acetate indicates a much higher propensity of this liquid to permeate the material. The EDS mapping of the fracture surfaces of the HDPE scaffolds confirm the presence of ZnO nanoparticles in the porous sample dipped in the butyl acetate-based suspensions. It is worth noting that the EDS analysis was performed in the center of the disk, meaning that the ZnO suspension effectively penetrates deep inside the HDPE scaffold. On the contrary, the water-based dispersion cannot access the inner parts of the sample due to the unfavorable contact angle, and no signal related to the filler was detected (Figure 7).

Table 2. Contact angle of water and butyl acetate on HDPE

Probing liquid	θ [°]
Water	96.5±3.4
Butyl acetate	15.7±2.7

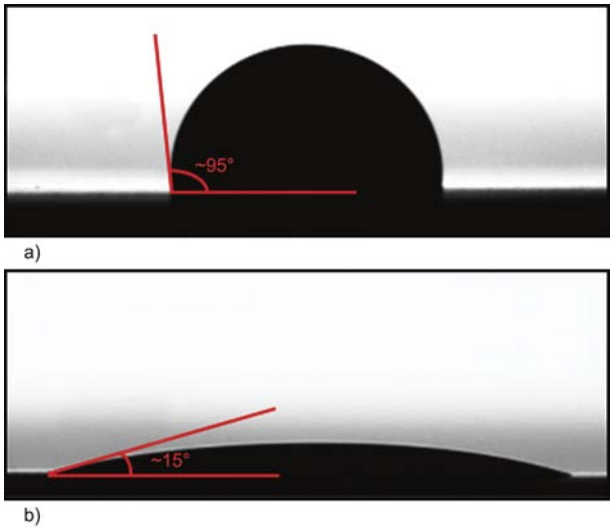

Figure 6. Illustrative images of the contact angle measurements for HDPE films with (a) water and (b) butyl acetate

More quantitative proofs of the presence of ZnO nanoparticles come from the TGA analyses performed on the HDPE scaffolds dipped into the two colloidal suspensions. As summarized in Table 3, a residual is noticed at high temperature, i.e. after the volatilization of the polymer, in both samples. Taking the residual of the C15A-containing HDPE scaffold as the reference, more than 2 wt% of ZnO nanoparticles remains trapped in the sample dipped in the butyl acetate-based suspension, compared to little more than 0.5 wt% of the one immersed in the water-based suspension.

Once the ZnO nanoparticles have been trapped in the HDPE scaffolds, the porous samples have been compacted as described in the Experimental section. The forth step of the procedure depicted in Figure 1 determines the eventual space arrangement of the ZnO nanoparticles in the TB samples. EDS analyses were performed to localize the filler. The SEM micrographs of the TB and MM samples with the X-ray maps of the Zn are compared in Figure 8.

Although unable to overcome the strong cohesive forces which held together the primary ZnO nanoparticles within the aggregates, the MM route ensures a good distribution of the filler on micro-scale. On the contrary, the EDS mapping of the compacted TB

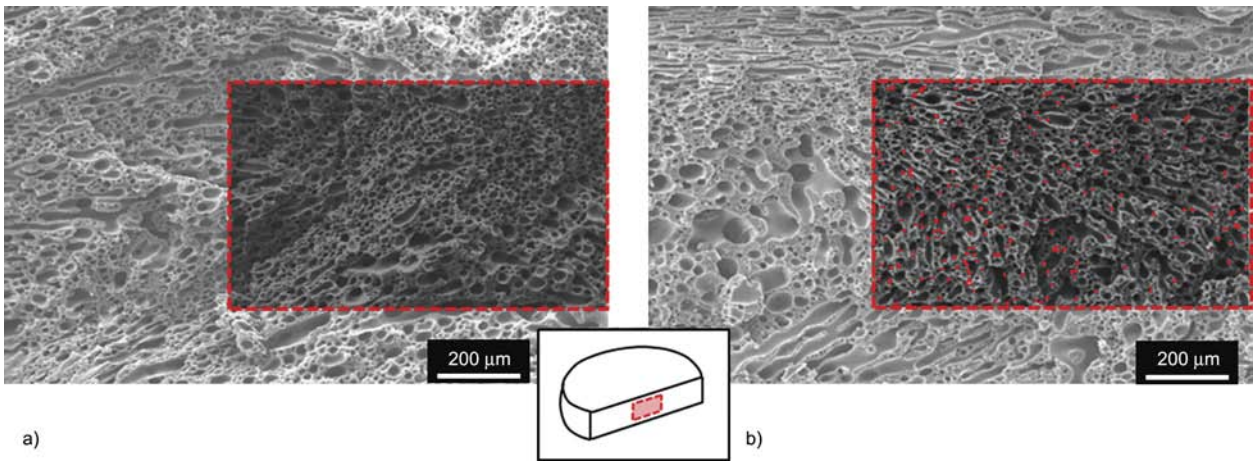

Figure 7. SEM micrographs with the X-ray map of zinc partially superimposed on it for the blends after immersion in the ZnO dispersion in (a) water and (b) butyl acetate

Table 3. Residual weight at 700°C of the HDPE scaffolds after immersion in ZnO dispersions in water and butyl acetate

Sample	Residual [wt%]
HDPE	0.01
PEO	1.71
HDPE/PEO	0.78
HDPE (PEO extracted)	0.15
HDPE/PEO+C15A	2.32
HDPE+C15A (PEO extracted)	1.68
HDPE+C15A+ZnO (water)	2.37
HDPE+C15A+ZnO (butyl acetate)	3.85

sample reveals an inhomogeneous filler distribution, with ZnO-rich micro-channels intercalated with ZnO-poor regions. This is in line with what we expected: the ZnO suspension can only penetrates the channels of the scaffold, but it cannot permeate their HDPE walls. As a result, micron-sized polymer domains devoid of filler will coexist with a continuous network of channels full of nanoparticles. Nonetheless, deriving from isolated ZnO nanoparticles firmly suspended in the liquid phase, the filler trapped in the TB samples is expected to be less aggregated than in the MM samples. Again, viscoelastic analysis is used as indirect and yet powerful tool to assess the state of dispersion of the particles. The time evolution of G' at $\omega = 10^{-1}$ rad/s and the frequency-dependent moduli of the TB nanocomposite at about 2 wt% of ZnO are shown in Figure 9. Note that about 1.5 wt% of C15A remains trapped in the HDPE during the procedure to prepare the TB samples. A reference sample containing the same amounts of ZnO and C15A was then prepared by melt mixing and used for comparison.

Neither the time evolution of G' at low frequency nor the relaxation spectrum of the MM sample disclose the presence of the filler, confirming the ineffectiveness of the MM route in dispersing ZnO nano-

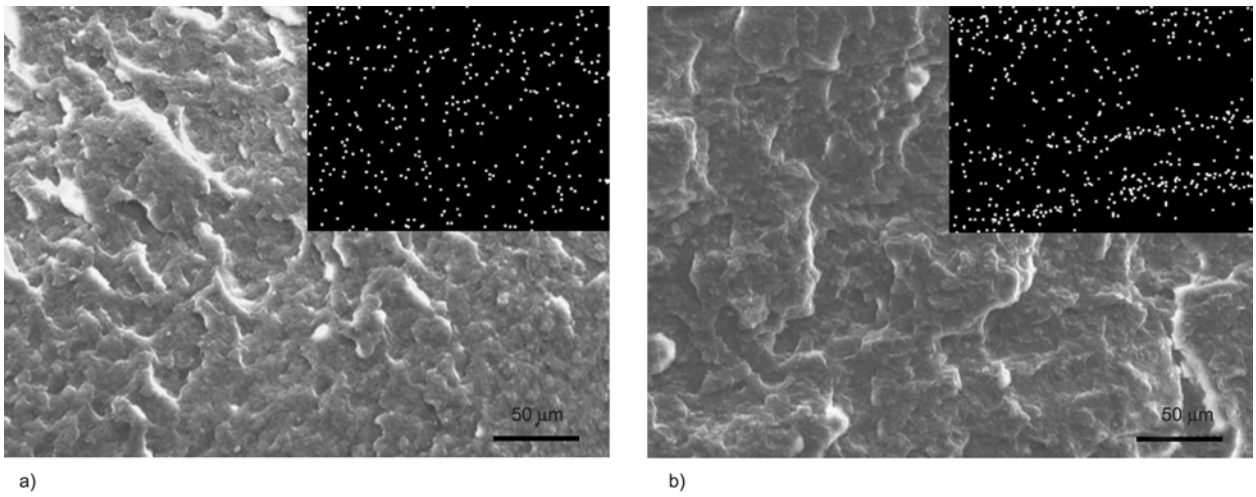

Figure 8. SEM micrographs with the corresponding X-ray map of zinc in the inset for the samples prepared trough (a) the melt mixing and (b) template-based method

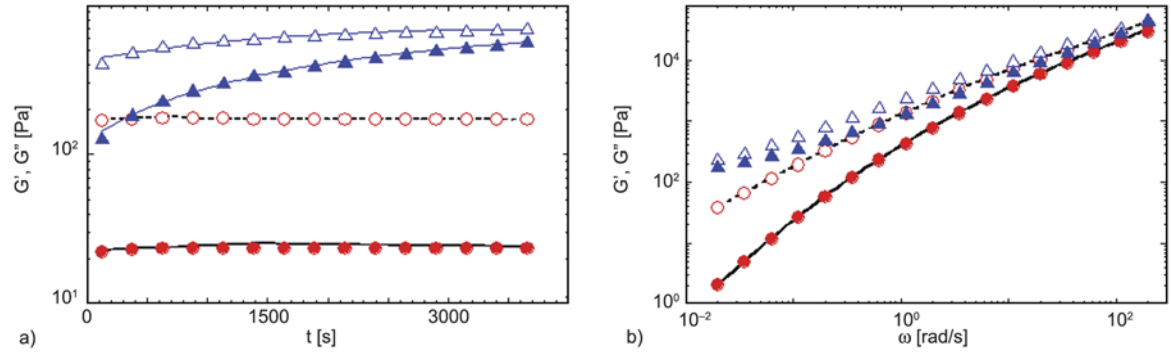

Figure 9. (a) Time evolution and (b) frequency-dependence of G' (full symbols) and G'' (empty symbols) of the PNCs prepared trough melt mixing (red circles) and template-based method (blue triangles) at Φ_{ZnO} ~2 wt%. Solid and dashed black lines represent G' and G'', respectively, of neat HDPE. Blue lines in a are guide for the eye.

particles within a non-polar matrix such as HDPE. Even possible synergistic effects with a secondary filler such as C15A have to be excluded. On the contrary, the filler strongly affects the viscoelasticity of the TB sample. Specifically, the growth of the low-frequency moduli reflects the structural rearrangements of the nanoparticles, which flocculate in the melt driven by attractive forces. Such particle mobility has to be ascribed to a finer dispersion of the filler which allows the smaller aggregates to experience the Brownian motions essential for the emergence of the peculiar pseudo-solidlike behavior of well dispersed PNCs. The relaxation spectrum of the TB sample collected at the end of the time scan is shown in Figure 9b. The moduli get flat at low frequency, with a prominent effect on G' which increases of more than two order of magnitude with respect to the unfilled matrix despite the low amounts of filler considered. It is worth noting that similar alterations in the viscoelastic behavior cannot be found in the literature for HDPE-based nanocomposites unless performing modifications of the particle surface and/or adding suitable compatibilizers to reduce the chemical incompatibility between the polymer and the filler [23–25].

The viscoelastic behavior has been investigated also in the solid state by means of DMA (Figure 10).

Nanoparticles constrain the deformability of the amorphous fraction of HDPE in which they reside, improving the dynamic mechanical moduli. As DSC analyses exclude noticeable alterations of the crystalline structure of the HDPE (Table 4), the dynamic-mechanical properties primarily reflect the quality of the filler dispersion.

As in the melt state, the nanoparticles in the TB sample are much more effective in reinforcing the matrix. Again, the state of dispersion of the filler

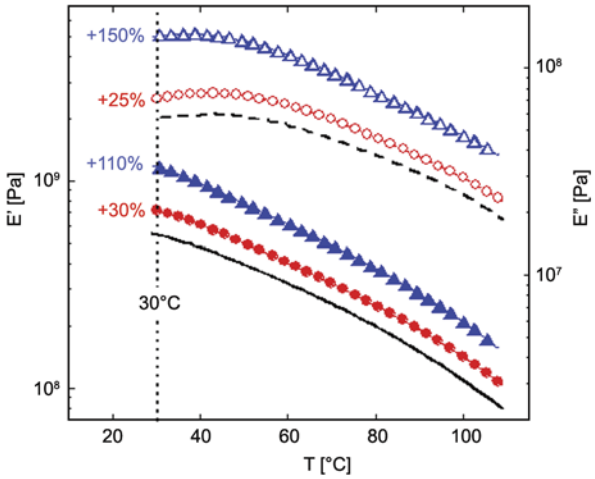

Figure 10. Temperature-dependence of E' (full symbols) and E'' (empty symbols) of the nanocomposite prepared trough melt mixing (red circles) and template-based method (blue triangles) at Φ_{ZnO} ~2 wt%. Solid and dashed black lines represent E' and E'', respectively, of neat HDPE

Table 4. Onset and peak melting temperatures, crystallization temperature and crystallinity of neat HDPE and nanocomposites

Sample	$T_{m,onset}$ [°C]	$T_{m,peak}$ [°C]	Tc [°C]	χ_c [%]
HDPE	123.5	128.8	115.3	54.5
MM	124.6	128.4	116.3	53.2
TB	122.6	128.7	116.1	53.5

appears more important than its distribution on micron-scale in enhancing the macroscopic structural properties of PNCs.

Finally, the tensile behavior of the TB samples has been investigated. The Young's modulus, tensile strength and elongation at break are shown in Figure 11 taking the neat HDPE as a reference.

As consequence of the good particle dispersion, the modulus of the nanocomposite is noticeably higher

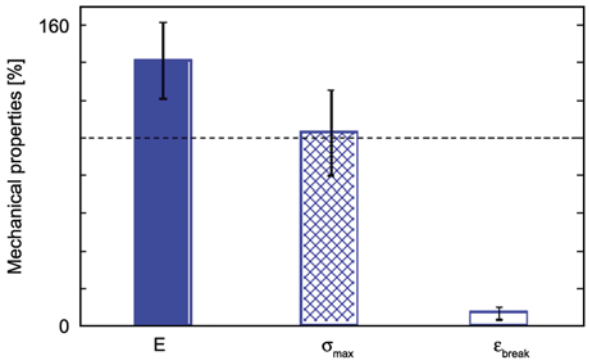

Figure 11. Mechanical properties of the TB sample: Young's modulus, tensile strength and elongation at break. The values are normalized with respect to the neat matrix.

than that of the matrix. However, such a strengthening is coupled with a remarkable loss in ductility, which reflects the inherent non-homogeneity of the sample. Specifically, besides the non uniform particle distribution, the ineludible presence of residual domains of PEO, which we estimate to be in the range 6–8 wt%, makes the TB sample obviously brittle. Such a drawback must be taken into account in the analysis of pros and cons of the TB approach. Provided that a material embrittlement is passable, we argue that the proposed approach can be capitalized to impart specific functionality to the composite. As an example, using conductive fillers such as carbon nanotubes or graphene-based particles, very low percolation thresholds can be in principle attained, thus enhancing the electrical and/or thermal conductivity of the host polymer. A similar strategy underpins the double percolation concept, sometimes exploited in case of polymer blends with interfacially-located particles [26]. The latter condition can be difficult to realize, being dictated by cogent thermodynamic requirements. Differently, the TB approach in principle could result in low percolation thresholds in monophasic matrices irrespective of wettability considerations.

4. Conclusions

The efficiency of a novel template-based approach for the dispersion of hydrophilic nanoparticles within hydrophobic polymer matrices has been investigated using a system prepared by melt mixing as reference. The procedure envisages that a well dispersed ZnO nanoparticles suspension penetrates inside a microporous HDPE scaffold obtained by selective extraction of a sacrificial PEO phase blended with the HDPE. To finely distribute the nanoparticles inside the host matrix, two opposing requirements have been conciliated: (i) having a scaffold with a thick network of tiny channels and yet (ii) preserving the penetration depth of the ZnO suspension along the sample thickness. The goal has been reached through a judicial selection of the materials and the adoption of targeted expedients throughout the compounding procedure. Deriving from isolated ZnO nanoparticles firmly suspended in the liquid phase, the filler trapped in the microporous sample has resulted much better dispersed than in the melt mixed sample, and noticeable increases of the viscoelastic properties of the PNCs have been achieved. On the other hand, morphological analyses reveal ZnO-rich domains surrounded by ZnO-poor regions, indicating an inhomogeneous filler distribution on micron-scale. Despite a detrimental effect on the material ductility, the latter can be capitalized to minimize the amount of nanoparticles required to attain a certain improvement of functional properties. Although hard to scale up in an industrial context, our results demonstrate the possibility to realize spatially engineered polymer nanocomposites through the clever subtraction of volumes of materials where the nanoparticles can access in the course of the compounding.

Acknowledgements

This work has been supported by the Italian Ministry of University and Research (MIUR) through the PRIN 2009 prot. 2009WXXLY2_002.

References

[1] Sanchez C., Belleville P., Popall M., Nicole L.: Applications of advanced hybrid organic–inorganic nanomaterials: From laboratory to market. Chemical Society Reviews, **40**, 696–753 (2011). DOI: 10.1039/C0CS00136H

[2] Jancar J., Douglas J. F., Starr F. W., Kumar S. K., Cassagnau P., Lesser A. J., Sternstein S. S., Buehler M. J.: Current issues in research on structure–property relationships in polymer nanocomposites. Polymer, **51**, 3321–3343 (2010). DOI: 10.1016/j.polymer.2010.04.074

[3] Hiemenz P., Rajagopalan R.: Principles of colloid and surface chemistry. Marcel Dekker, New York (1997).

[4] Balazs A. C., Emrick T., Russell T. P.: Nanoparticle polymer composites: Where two small worlds meet. Science, **314**, 1107–1110 (2006). DOI: 10.1126/science.1130557

[5] Demir M. M., Wegner G.: Challenges in the preparation of optical polymer composites with nanosized pigment particles: A review on recent efforts. Macromolecular Materials and Engineering, **297**, 838–863 (2012). DOI: 10.1002/mame.201200089

[6] Peponi L., Tercjak A., Martin L., Mondragon I., Kenny J. M.: Morphology-properties relationship on nanocomposite films based on poly(styrene-*block*-diene-*block*-styrene) copolymers and silver nanoparticles. Express Polymer Letters, **5**, 104–118 (2011). DOI: 10.3144/expresspolymlett.2011.12

[7] Tyurin A., De Filpo G., Cupelli D., Nicoletta F. P., Mashin A., Chidichimo G.: Particle size tuning in silver-polyacrylonitrile nanocomposites. Express Polymer Letters, **4**, 71–78 (2010). DOI: 10.3144/expresspolymlett.2010.12

[8] Chow W. S., Leu Y. Y., Mohd Ishak Z. A.: Effects of SEBS-g-MAH on the properties of injection moulded poly(lactic acid)/nano-calcium carbonate composites. Express Polymer Letters, **6**, 503–510 (2012). DOI: 10.3144/expresspolymlett.2012.53

[9] Nordström J., Matic A., Sun J., Forsyth M., MacFarlane D. R.: Aggregation, ageing and transport properties of surface modified fumed silica dispersions. Soft Matter, **6**, 2293–2299 (2010). DOI: 10.1039/b921488g

[10] Agrawal M., Gupta S., Zafeiropoulos N. E., Oertel U., Häßler R., Stamm M.: Nano-level mixing of ZnO into poly(methyl methacrylate). Macromolecular Chemistry and Physics, **211**, 1925–1932 (2010). DOI: 10.1002/macp.201000191

[11] Fidelus J., Piticescu R. R., Piticescu R. M., Lojkowski W., Giurgiu L.: Solvothermal synthesis of Co-doped ZnO nanopowders. Zeitschrift für Naturforschung B, **63**, 725–729 (2008).

[12] Wunderlich B.: Macromolecular physics, Vol. 3. Academic Press, New York (1980).

[13] Baird D. G., Collias D. I.: Polymer processing principles and design. Butterworth-Heinemann, Newton (1995).

[14] Tjong S. C.: Structural and mechanical properties of polymer nanocomposites. Materials Science and Engineering R: Reports, **53**, 73–197 (2006). DOI: 10.1016/j.mser.2006.06.001

[15] Hess S., Demir M. M., Yakutkin V., Baluschev S., Wegner G.: Investigation of oxygen permeation through composites of PMMA and surface-modified ZnO nanoparticles. Macromolecular Rapid Communications, **30**, 394–401 (2009). DOI: 10.1002/marc.200800732

[16] Galindo-Rosales F. J., Moldenaers P., Vermant J.: Assessment of the dispersion quality in polymer nanocomposites by rheological methods. Macromolecular Materials and Engineering, **296**, 331–340 (2011). DOI: 10.1002/mame.201000345

[17] Romeo G., Filippone G., Russo P., Acierno D.: Effects of particle dimension and matrix viscosity on the colloidal aggregation in weakly interacting polymer-nanoparticle composites: A linear viscoelastic analysis. Polymer Bulletin, **63**, 883–895 (2009). DOI: 10.1007/s00289-009-0176-2

[18] Acierno D., Filippone G., Romeo G., Russo P.: Dynamics of stress bearing particle networks in poly (propylene)/alumina nanohybrids. Macromolecular Materials and Engineering, **292**, 347–353 (2007). DOI: 10.1002/mame.200600386

[19] Acierno D., Filippone G., Romeo G., Russo P.: Rheological aspects of PP-TiO_2 micro and nanocomposites: A preliminary investigation. Macromolecular Symposia, **247**, 59–66 (2007). DOI: 10.1002/masy.200750108

[20] Dorigato A., Pegoretti A., Penati A.: Linear low-density polyethylene/silica micro- and nanocomposites: Dynamic rheological measurements and modelling. Express Polymer Letters, **4**, 115–129 (2010). DOI: 10.3144/expresspolymlett.2010.16

[21] Filippone G., Romeo G., Acierno D.: Role of interface rheology in altering the onset of *co*-continuity in nanoparticle-filled polymer blends. Macromolecular Materials and Engineering, **296**, 658–665 (2011). DOI: 10.1002/mame.201000343

[22] Washburn E. W.: The dynamics of capillary flow. The Physical Review, **17**, 273–283 (1921). DOI: 10.1103/PhysRev.17.273

[23] Sharif-Pakdaman A., Morshedian J., Jahani Y.: Influence of the silane grafting of polyethylene on the morphology, barrier, thermal, and rheological properties of high-density polyethylene/organoclay nanocomposites. Journal of Applied Polymer Science, **125**, E305–E313 (2012). DOI: 10.1002/app.36367

[24] Chae D. W., Kim K. J., Kim B. C.: Effects of silicalite-1 nanoparticles on rheological and physical properties of HDPE. Polymer, **47**, 3609–3615 (2006). DOI: 10.1016/j.polymer.2006.03.053

[25] Majid M., Hassan E-D., Davoud A., Saman M.: A study on the effect of nano-ZnO on rheological and dynamic mechanical properties of polypropylene: Experiments and models. Composites Part B: Engineering, **42**, 2038–2046 (2011). DOI: 10.1016/j.compositesb.2011.04.043

[26] Sumita M., Sakata K., Hayakawa Y., Asai S., Miyasaka K., Tanemura M.: Double percolation effect on the electrical conductivity of conductive particles filled polymer blends. Colloid and Polymer Science, **270**, 134–139 (1992). DOI: 10.1007/BF00652179